5-2007

Does the Southern Farmington Canyon Complex Record a late Archean/Early Proterozoic Accretionary Complex?

Kyle C. Andreasen
Utah State University

DOES THE SOUTHERN FARMINGTON CANYON COMPLEX RECORD A LATE ARCHEAN/EARLY PROTEROZOIC ACCRETIONARY COMPLEX?

Kyle C. Andreasen

A thesis submitted in partial fulfillment
of the requirements for the degree

of

MASTER OF SCIENCE

in

Geology

Approved:

UTAH STATE UNIVERSITY
Logan, Utah

2007

ABSTRACT

Geology of the Farmington Canyon Complex

by

Kyle C. Andreasen, Master of Science

Utah State University, 2007

Major Professor: Dr. John W. Shervais
Department: Geology

The Farmington Canyon Complex, situated along the Wasatch front in northern Utah, has been the target for many studies. The FCC has been interpreted to be a passive margin sedimentary wedge. Previous studies have yielded isotopic ages that broadly support an Archean age of formation, and a prominent mid-proterozoic amphibolite grade metamorphic event.

Based on this study, a new interpretation for the FCC is presented. Field relations and whole-rock geochemistry as well as recent advances in understanding Archean crustal processes have resulted in the FCC to be considered as an accretionary complex that formed along the SW margin of the Wyoming province in the early Archean. Rock assemblages such as mafic and ultramafic metavolcanics have chemistries that resemble oceanic crust and arc related volcanics. The extensive quartzo-felspathic gneiss and schist units have compositions that reflect greywacke, and are presented here as a mélange matrix. The quartzites have chemistries, which may represent cherts or silicified microbial mats. The field relations and timing of these rocks indicate that the FCC may

represent a continental arc synchronous with the closing of an ocean basin, forming an accretionary wedge. This culminated with the mid-proterozoic metamorphic event as this continental arc collided with the Santaquin arc, as well as the SW margin of Laurentia. This amphibolite grade metamorphic event has subsequently reset or overprinted isotopic evidence and obscured any textures that may have existed.

Although much has yet to be learned about Archean processes, comparison to other recognized Archean accretionary complexes has yielded striking similarities, and it is presented here that the FCC represents an active margin, and is likely an accretionary mélange.

(145 pages)

ACKNOWLEDGEMENTS

Many thanks go to Dr. John Shervais for the many discussions and revisions for this thesis. His valuable input and guidance have proven to be very helpful for this paper as well as developing my talents and knowledge base in many aspects. Special thanks also go to my committee members, Dr. Peter Kolesar and Dr. Carol Dehler, for their guidance and input. I would also like to thank the Geology Department and staff for their help.

Last but not least, I would like to thank my wife and kids for their support and sacrifices. Many days were spent with an absentee husband and father, as I did field work or ignored them while working on the computer. They truly have suffered the most, while I worked on this project.

Kyle C. Andreasen

CONTENTS

LIST OF TABLES

LIST OF FIGURES

CHAPTER 1

INTRODUCTION

INTRODUCTION

The formation of continental crust today is a "steady state" process, resulting from the subduction of oceanic lithosphere beneath continental and oceanic arcs. This differs greatly from the more dynamic and chaotic processes in the Archean (Shervais, 2006). Formation of continental crust during the Archean may have predated plate tectonics. Since more than half of the existing continental crust may have formed initially prior to 2.5 Ga (Kröner, 1985; Reymer and Schubert, 1984), it is therefore essential to understand how these processes differed during early earth history from more typical post-Archean processes.

The Archean is considered a period of high heat flow, and mantle convection was most likely dominated by chaotic thermal convection (e.g., Hamilton, 1998). Other workers have applied modern plate tectonic models; however, there are some inconsistencies in their correlations (e.g., de Wit et al., 1992; Connelly and Ryan, 1996; de Wit, 1998; Dirks and Jelsma, 1998; Kusky and Polat, 1999; Calvert and Ludden, 1999). Others suggest mechanisms from complex processes involving rising mantle plumes (Wyman and Kerrich, 2002) or sinking of eclogitic protocrusts (Zegers and van Keken, 2001). Recent computer models have generated plate-like behavior using an upper cold thermal boundary layer, i.e., lithosphere, which generated a large strong plate-like segment that can deform at weak, narrow boundaries that rapidly deform (Bercovici, 2003).

If the processes that formed continental crust truly differed during early earth history, when did this transition occur? The timing of the transition from Hadean-style thermal regimes controlled by mantle plumes and upwellings, to the modern thermal structure, controlled by the sinking of cold lithospheric plates is not well understood (e.g., Shervais, 2006).

The recognition of Phanerozoic-style plate tectonics is usually distinguished by one or more of the following assemblages: oceanic crust/ophiolites, island arc volcanic/plutonic series, and accretionary complexes. Archean tonalite-trondjhemite-granodiorite (TTG) suites and greenstone belts have been correlated geochemically and petrologically to the island arc and oceanic crust sequences, however these correlations are not universally accepted (e.g., Hamilton, 1998). Recognition of accretionary complexes would be very helpful, in that they provide more persuasive evidence of Archean subduction. To date, only two potential Archean subduction zone complexes have been recognized. The first is the Dongwanzi ophiolite mélange in the North China craton (Kusky et al., 2001; Li et al., 2002), and the second being the Schreiber-Hemlo greenstone belt in the Superior province of Canada (Polat et al., 1998; Polat and Kerrich, 1999). Additionally, Archean accretionary complexes have been recognized (e.g. Wutaishan greenstone belt) in the North China craton (Polat et al., 2005) and many more around the world that are just now being recognized and studied in further detail. It is important to note that greenstone belts have not been universally accepted as representing subduction processes.

This thesis looks at a third possible example: the Farmington Canyon Complex in the Wasatch Mountains of northern Utah (Bryant, 1988a; Shervais, 2006).

THE FARMINGTON CANYON COMPLEX

The Late Archean/Early Proterozoic Farmington Canyon Complex (FCC) is a metamorphic assemblage of migmatitic felsic gneiss, with locally abundant granite, amphibolite, schist and quartzite. Metamorphic grade is amphibolitic with greenschist facies overprint along shear zones (Bryant, 1988a). Rocks of the FCC are generally more migmatitic to the north.

The FCC is exposed in a narrow N-S trending belt (45 x 6 km) along the western Wasatch Mountains. It also comprises most of Antelope Island west of the Wasatch Mountains in northern Utah. Both outcrop belts lie along the eastern margin of the Basin and Range province (Fig 1-1). The complex is situated within the Selway province, which is on the southwestern margin of the Archean Wyoming province, and the northeastern margin of the Paleoproterozoic Mojave province (Fig 1-2).

The complex is allochthonous, and was emplaced along the Ogden thrust, which bounds the complex on the north and east during the Cretaceous Sevier Orogeny. The complex is well exposed along the western edge of the Wasatch Mountains, and the western and eastern flanks on Antelope Island due to Cenozoic normal faulting.

In the Wasatch Mountains, the FCC is overlain unconformably by the Cambrian Tintic Quartzite, a trangressive sequence of sandstones with minor siltstones and shales deposited along the miogeocline of the western margin of North America during the Cambrian; or the Tertiary Wasatch Formation, a continental clastic succession of

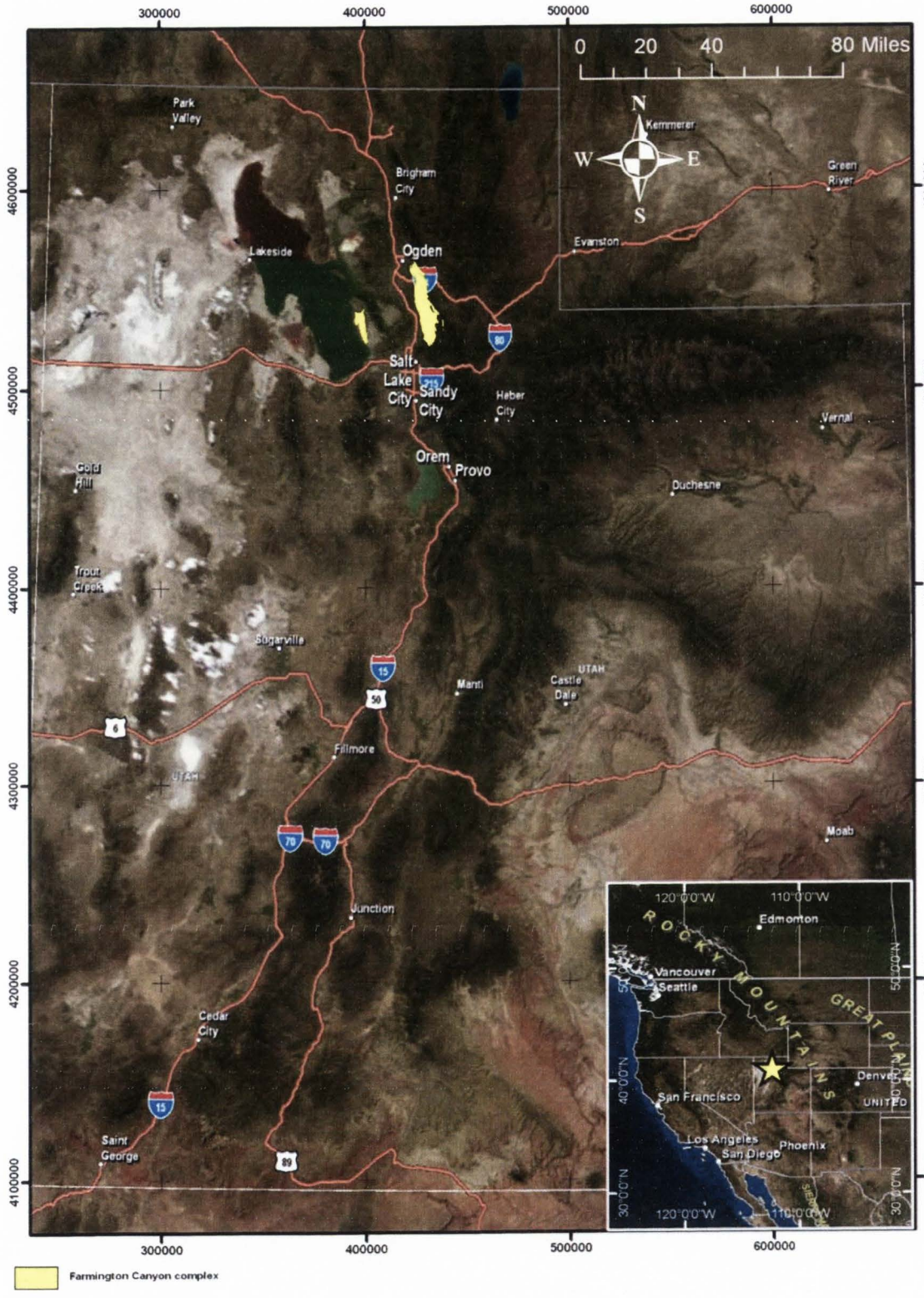

Figure 1-1. Location map of the Farmington Canyon Complex modified from Bryant (1988a). Larger map in UTM zone 12N.

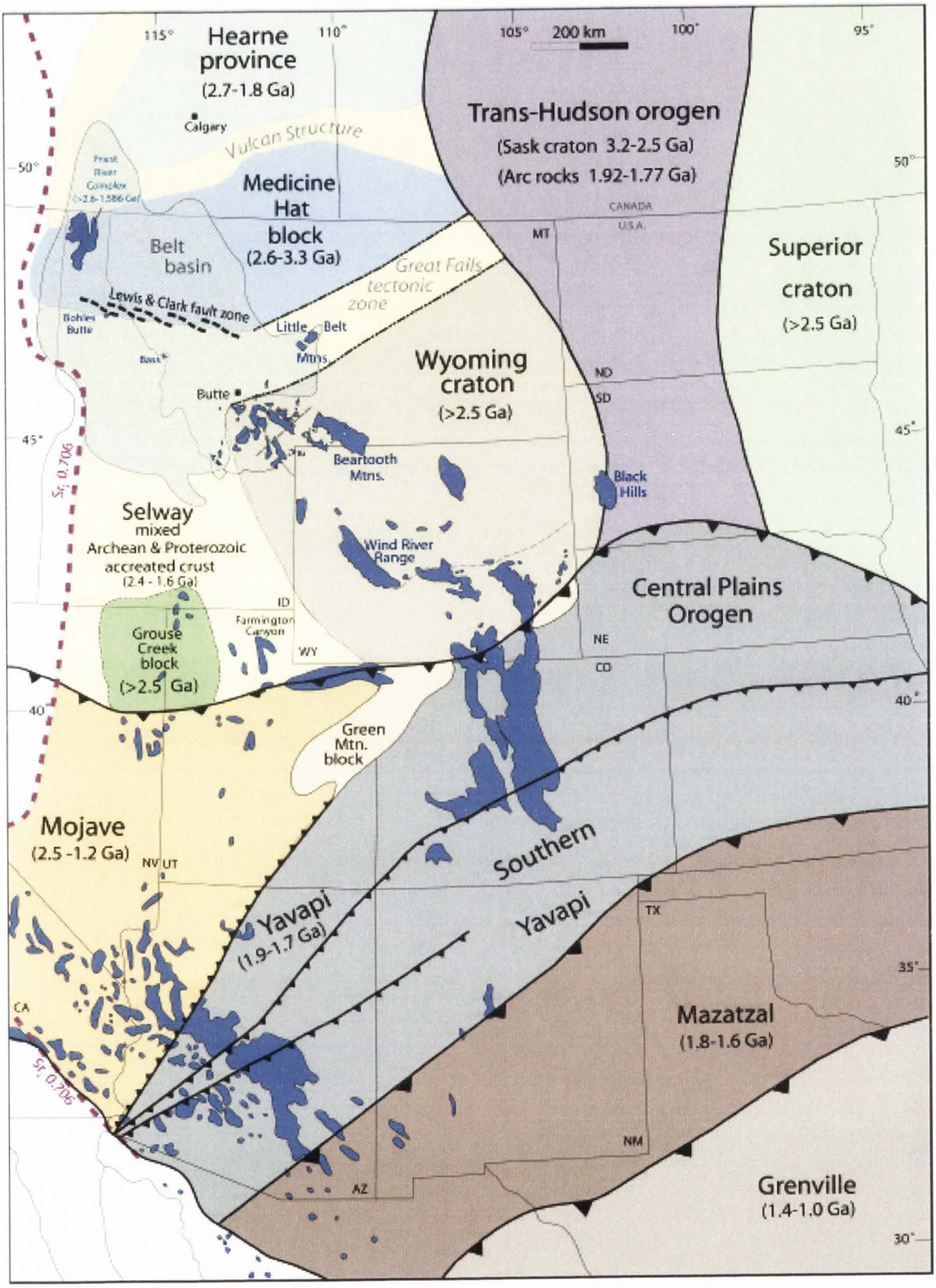

Figure 1-2. Map of basement provinces in the US western Cordillera from Foster et al. (2006).

sandstone, conglomerate and siltstone which were shed from the highlands during the Laramide uplift (Doelling et al., 1990; Willis et al., 2000). On Antelope Island, the complex is unconformably overlain by the Neoproterozoic Mineral Fork and Kelley Canyon formations, the Cambrian Tintic Quartzite, or by the Tertiary Wasatch Formation (Doelling et al., 1990; Willis et al., 2000). The Mineral Fork Formation is a diamictite, which likely represents the Sturtian glacial epoch (Christie-Blick, 1997; Ehlers et al., 1997). The Kelley Canyon Formation is a tidal dolomite-shale succession that was interpreted to represent a rapid climate change after a low-latitude glacial episode (Christie-Blick, 1997; Ehlers et al., 1997).

Other Precambrian rocks are exposed nearby include the Santaquin Complex, which comprises basement rocks that are mostly igneous and metasedimentary rocks of medium and high metamorphic grade. The Santaquin Complex was inferred to be Archean by correlation with the FCC (Hintze, 1993). Chemical signatures such as low $^{87}Sr/^{86}Sr_i$ ratios and high εNd_t age of igneous rocks in the Santaquin complex suggest juvenile crusts associated with volcanic arc-related magmatism. Emplacement of the Santaquin arc has occurred between 1670-1700 Ma (Nelson et al., 2002)

Archean rocks of the Grouse Creek block as mapped by Compton (1972, 1975) are exposed in southeastern Idaho within the Selway block and consists of the Grouse Creek metamorphic core complex (gneiss dome), and quartzite, schist, and granite in the Raft River Mountains of the Albion Range. The core of the Grouse Creek Mountains contains orthogneiss and is unconformably overlain by the Proterozoic metasedimentary rocks (Miller et al., 2002) which are preserved as screens or pendants (Compton, 1972,

1975; Compton et al., 1977; Todd, 1980). The orthogneiss has been dated at 2.5 Ga, and contains less abundant exposures of metasedimentary rocks. These metasedimentary rocks are exposed as screens or In the Raft River range, metamorphism has created a stretch-pebble conglomerate unit. Archean and Proterozoic rocks of the Raft River Range is primarily gneisses and schists along with metamorphosed granite, pegmatite and mafic rocks. The oldest schists show relict features which indicate protoliths of mudstones, siltstones, shales, and feldspathic sandstones (Compton, 1972, 1975, 1980).

The Uinta Mountains, an anomalous east-west trending range, are located in the northeastern part of Utah, and are comprised primarily of the Uinta Mountain Group. These rocks represent deposition in a Mid-Neoproterozoic intracratonic basin (Condie et al., 2001; Dehler et al., 2007). These strata are ~4-7 km thick deposits of dominantly tough- and tabular-cross-bedded quartz sandstone, with minor siltstone, mudstone and shale (Hintze, 1993, Dehler et al., 2007).

PREVIOUS WORK

The crystalline basement rocks of the FCC were first recognized and described by Captain Howard Stansbury in 1853. The principal study of the FCC was performed by Bell (1951, 1952), in which he recognized rocks with mixed metamorphic grades, as well as retrograde metamorphism. Bryant (1988a) carried out detailed mapping of the FCC at a 1:50,000 scale. He was looking for major thrust faults that would intercalate younger Precambrian slices, as suggested by Bell (1951, 1952), and relate these thrusts to the thrust belts of southwestern Wyoming and north-central Utah. He also wanted to study the relations between blocks with different metamorphic histories. In addition to

mapping, samples were collected and analyzed using petrography, X-ray fluorescence, and ICP-optical emission spectroscopy (OES) (Bryant 1988a). Petrographic studies focused on modal compositions and mineralogy. In conjunction with Byant's research, fellow researchers did isotopic studies on the FCC rocks (Hedge and Stacey, 1980; Hedge et al., 1983).

Based on geochemistry and petrology, the gneisses of the FCC have been interpreted to represent a passive margin sedimentary wedge deposited on Archean crust that was metamorphosed to amphibolite grade during the mid-Proterozoic. This is supported by whole rock geochemical data, which correlate broadly with greywackes in composition (Bryant, 1988a,b; 1990; Doelling et al., 1990; Willis et al., 2000; Yonkee et al., 2000; Nelson et al., 2002).

The Archean age (3 Ga - 2.6 Ga) is based on inheritance in zircon U/Pb systematics, Nd model ages of amphibolites, and high Sr values in orthogneiss (Hedge et al., 1983). Rb-Sr and Sm-Nd whole-rock dates from the layered metamorphic rocks define a crude triangular array and Hedge (1983) gives three possible interpretations: 1) that crustal material in the FCC is as old as 2600 to 3600 m.y., and has been subsequently reset to varying degrees by later metamorphic events; 2) that the rocks of the FCC are no older than 2600 m.y., and they have inherited sediments from an older terrane; 3) the ages of the FCC rocks are 3000 to 3200 m.y., and have been influenced by a combination of older crustal inheritance and metamorphic resetting.

A Rb-Sr date from muscovite of a pegmatite yielded an age of 1.58 Ga (Giletti and Gast, 1961). Hedge et al. (1983) argue that this age reflects resetting to some degree.

Using whole-rock Rb-Sr dates from the granite mapped by Bryant as quartz monzonite gneiss, Hedge et al. (1983) report an age of 1808 ±34 m.y. Hedge et al. also report U-Pb dates of 1780 ± 20 m.y from zircons in gneiss, which match the Rb-Sr ages within analytical error. The emplacement of granite with high initial $^{87}Sr/^{86}Sr$ ratios (0.769) around 1800 Ma is consistent with the interpretation of an intense metamorphic event during this time, which coincided with anatectic melting (Hedge et al., 1983).

Barnett et al. (1993) suggest that the older ages may reflect the age of the sediment provenance (Wyoming craton crystalline rocks), and not its formation age (Nelson et al., 2002). Hornblende ^{40}Ar-^{39}Ar ages of 1586 to 1656 Ma and electron microprobe monazite $^{207}Pb/^{206}Pb$ ages of 1644 to 1711 Ma indicate a significant mid-Proterozoic metamorphic event in northern Utah (Nelson et al., 2002). Nelson et al. (2002) attribute this event to the collision of the Santaquin arc volcanic sequence (which formed *circa* 1700 Ma) with the Farmington Canyon Complex. Collision and metamorphism at 1700 Ma would obscure the basinal record and therefore make interpretation problematic.

GOALS OF THIS INVESTIGATION:

This investigation has three main goals: first, to understand the origin of mafic metavolcanic rocks of the FCC and the quartzite that is commonly associated with them; second, to understand the structural and spatial relationships between these rocks and the host gneisses; and third, to constrain the tectonic history of the FCC prior to the documented orogenic events around 1800 Ma.

CHAPTER 2

UNIT DESCRIPTIONS AND FIELD RELATIONSHIPS

INTRODUCTION

The FCC consists dominantly of quartzo-feldspathic gneiss and migmatitic gneiss, with less common quartzite, amphibolite, and ultramafic rocks. The main lithology of the FCC is highly deformed and foliated quartzo-felspathic gneiss. Migmatite is more common in the north with less common pegmatite and mica schist. In the southern part, including Antelope Island, the gneisses are only locally migmatitic. The southern part also contains more abundant lenses and discontinuous layers of amphibolite, quartzite, and rare ultramafic rocks (Bryant, 1988a, b; 1990). The transition between the southern and northern parts of the complex is gradational and may represent an increase in metamorphic grade to the north. The complex has undergone at least two documented metamorphic events including an intense mid-Proterozoic (1.7 Ma) amphibolite-grade metamorphism (Bryant, 1988a, b; 1990; Doelling et al., 1990; Willis et al., 2000; Yonkee et al., 2000; Nelson et al., 2002).

Mapping

Previous mapping was done on a 1:24,000 scale by Bryant (1988a). For this project, we carried out detailed mapping on a smaller and more detailed scale (1:12,000) in four carefully selected areas (Fig 2-1). Mapping was carried out using mélange style methodology as outlined by Hsu (1968). Our goal was to document relationships between amphibolite, quartzite and the enclosing gneiss, in specific, well exposed areas.

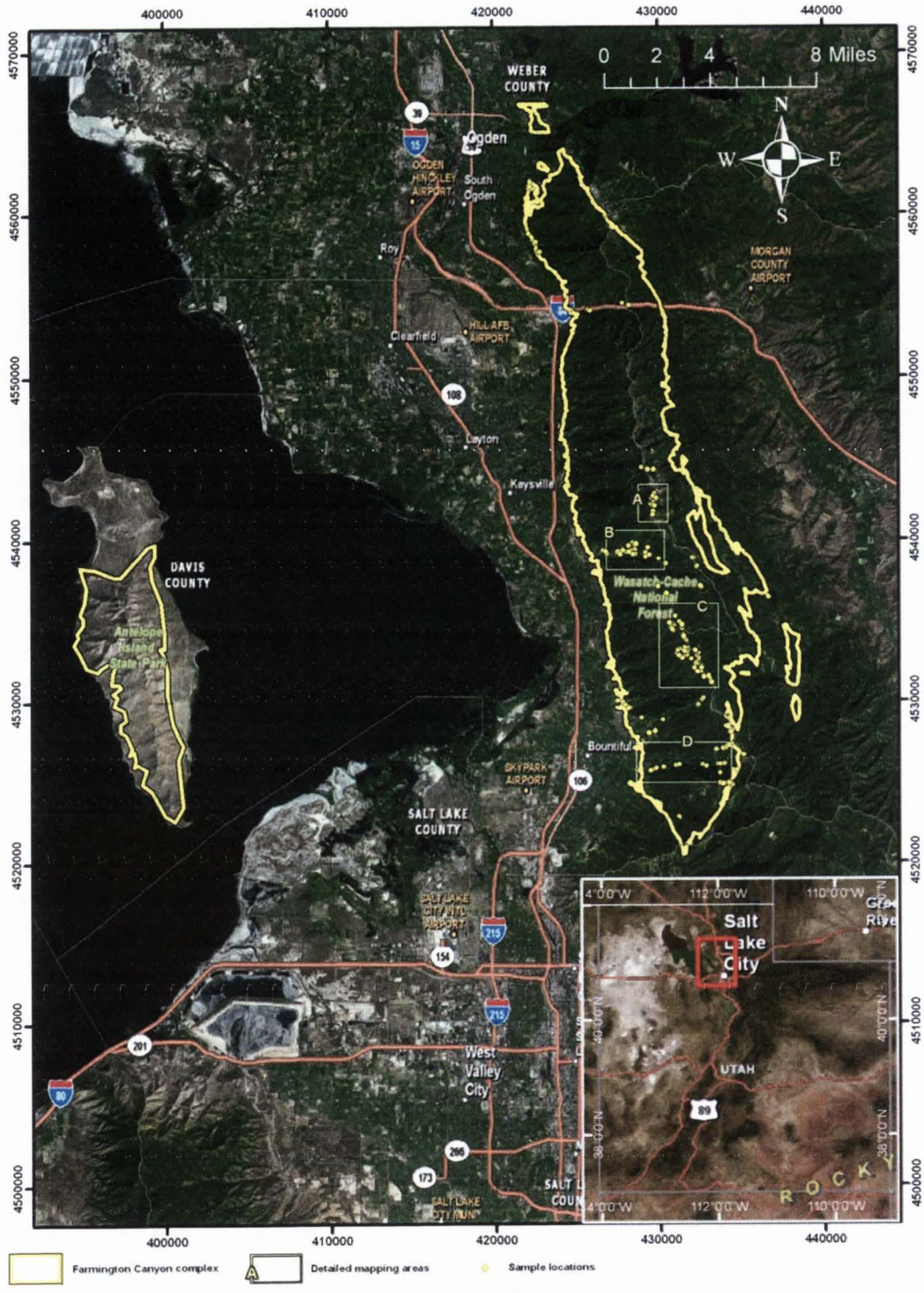

Figure 2-1. Map showing the distribution of the Farmington Canyon Complex in the Wasatch Mountains and on Antelope Island. Map in UTM zone 12N.

Mapping was carried out in the summer and fall of 2004. Additional mapping and field checks were carried out in late spring of 2005. Maps are shown as Figs 2-2 through 2-5 in the text, and as plates I-IV in the map packet, at a scale of 1/12,000. Sample locations are listed in UTM using NAD 1927 projection, and are listed in Table 2-1.

Gneiss

Light-to medium-grey-colored gneiss is the dominant lithology of the FCC (Fig 2-6 A-D), and can be subdivided into two groups: a more layered unit to the south and a more migmatitic unit to the north. Gneiss in the complex ranges from quartzo-feldspathic (Fig 2-6B) to a more amphibolitic character (Fig 2-6C). The migmatitic gneiss contains schist, amphibolite, and granite that have gradational contacts. Migmatitic gneisses also have pegmatitic segregational layering. The dominant lithology in the southern part of the complex is layered gneiss with minor schist, which is only locally migmatitic. Typical mineral assemblages include feldspar, quartz, biotite, hornblende, garnet, and microcline (Bryant, 1988a). Gneiss and schist have typically well-developed granoblastic textures.

The layered gneisses have chemical compositions similar to graywacke, and less commonly, arkose, and are interpreted by Bryant (1988a) to be derived from sandstone, siltstone and shale. In addition, some of the gneiss and schist that have > 50% feldspar are cited by Bryant as having a silicic volcanic conponent in them, such as a tuff, or tuffaceous sandstone.

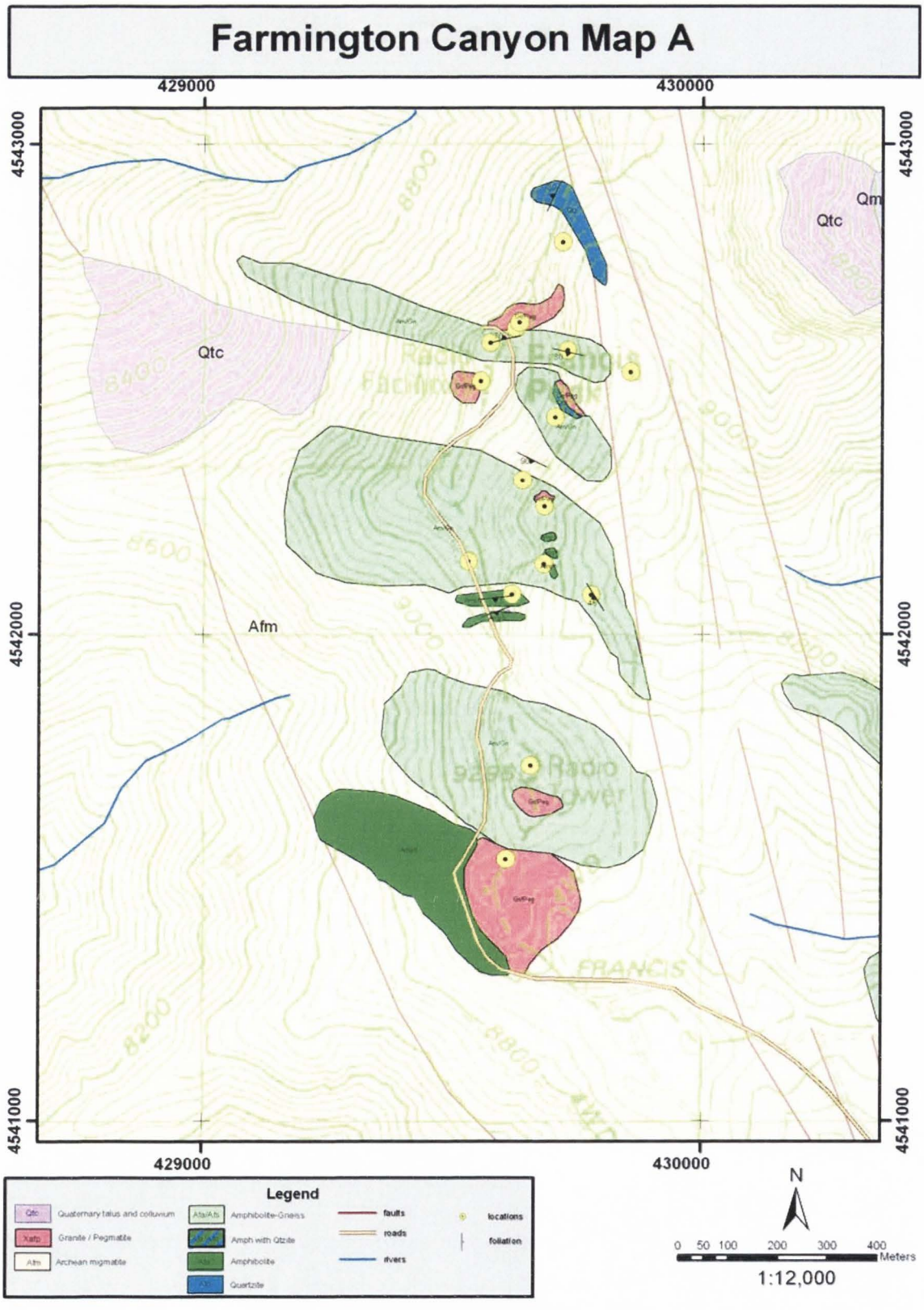

Figure 2-2. Detailed map of Francis Peak area in the Farmington Canyon Complex.

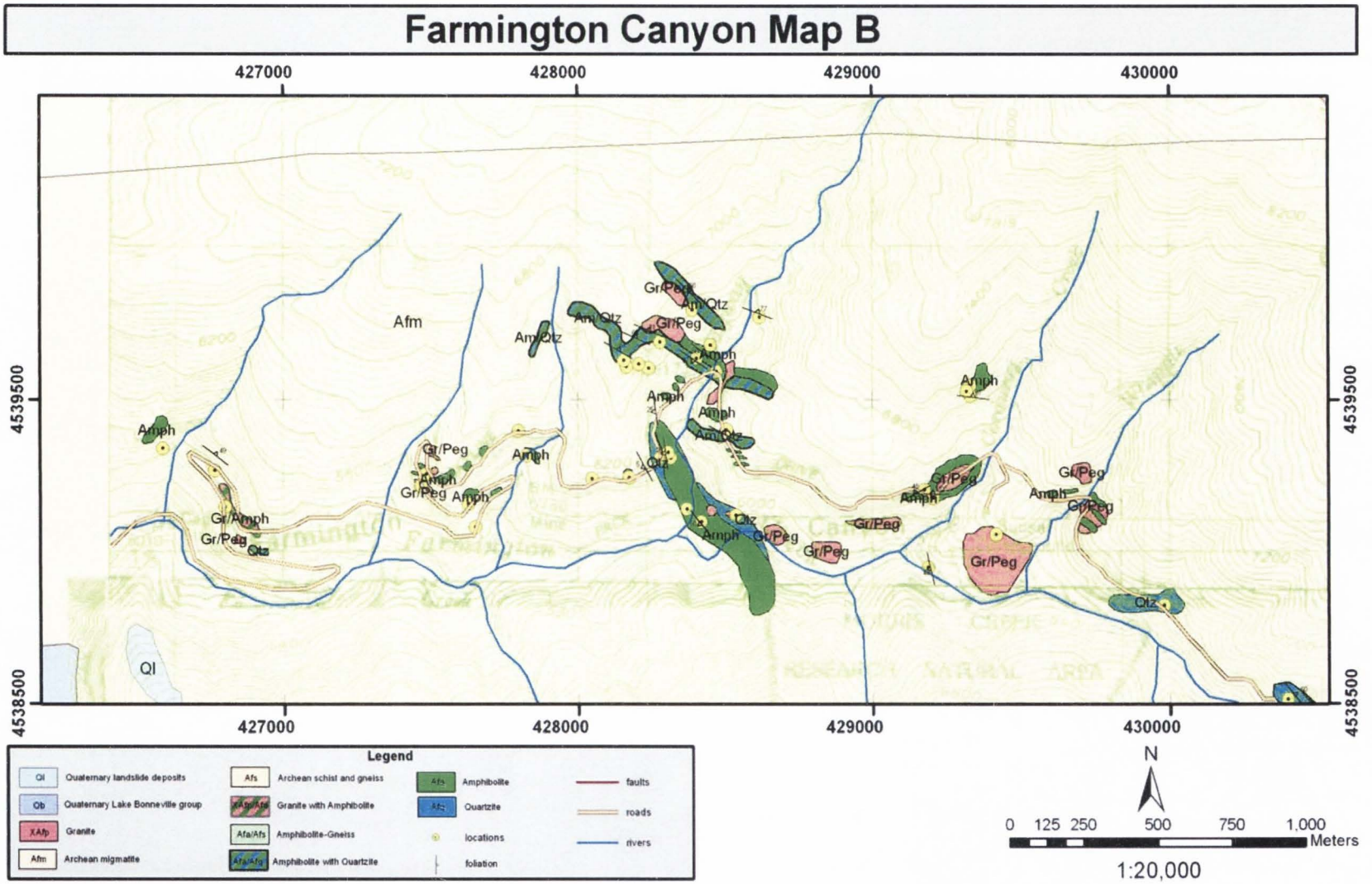

Figure 2-3. Detailed map of Farmington Canyon, in the Farmington Canyon Complex.

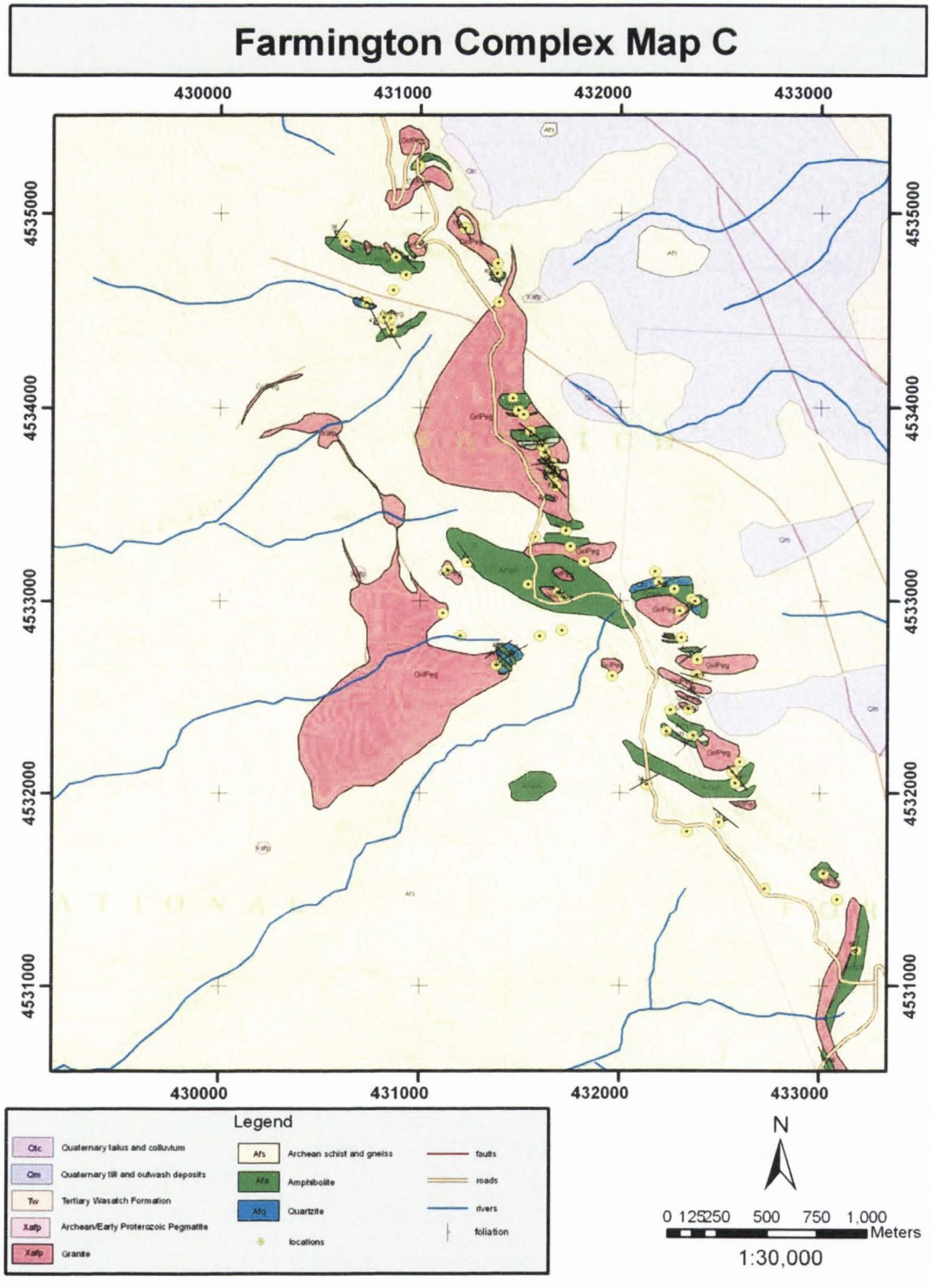

Figure 2-4. Detailed map of Bountiful Peak in the Farmington Canyon Complex.

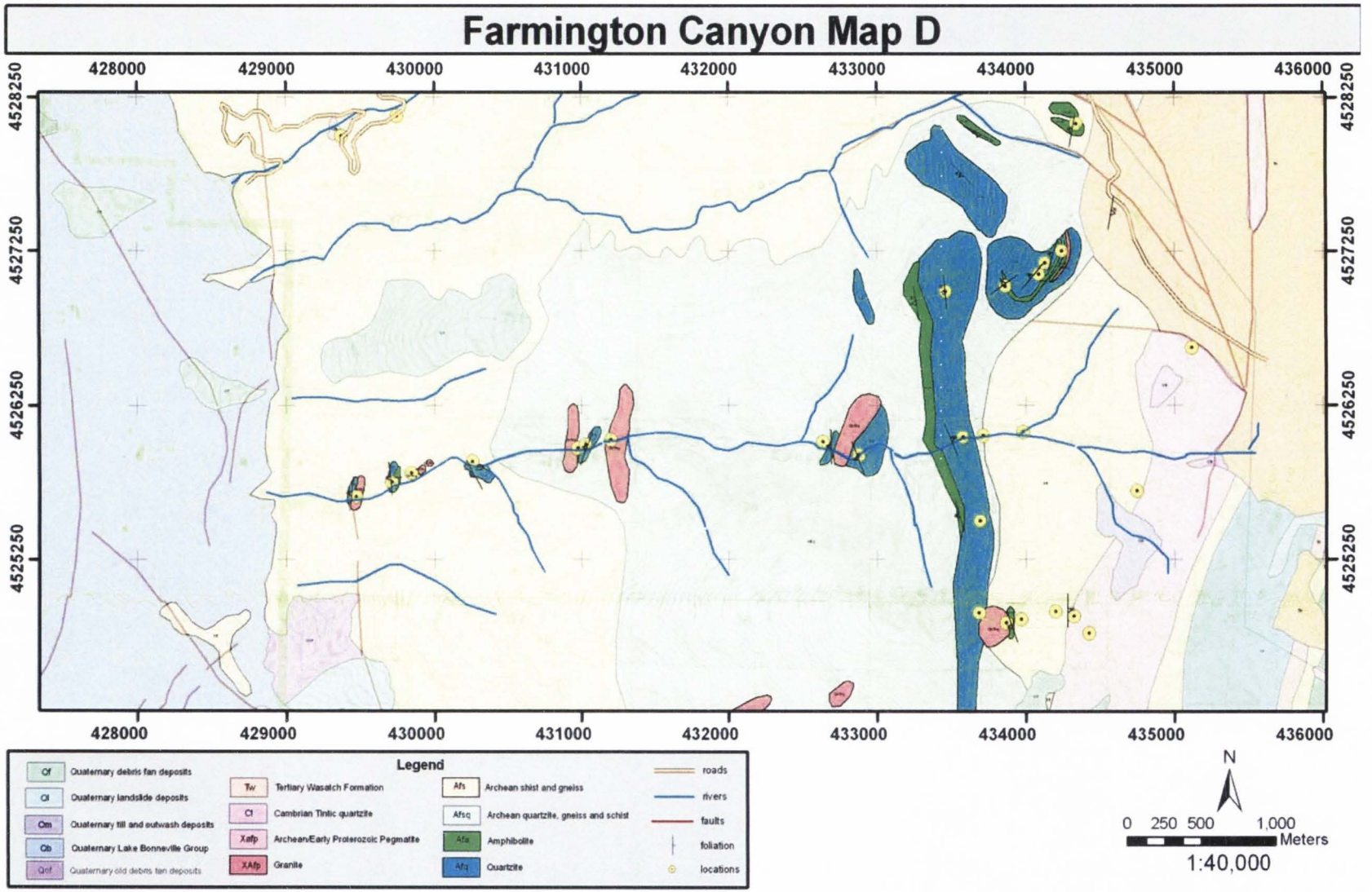

Figure 2-5. Detailed map of theSession Mountains in the Farmington Canyon Complex.

Table 2-1. Table showing locations of samples in UTM meters Zone12N (NAD 1929).

Sample #	Meters E	Meters N	Elevation (ft)	Description
FCC1-1B	428473	4539593	6180	Quartzite
FCC1-2B	428473	4539593	6180	Fine-grained amphibolite
FCC1-3B	428473	4539593	6180	Coarse grained amphibolite
FCC1-4	428473	4539593	6180	Amphibolite
FCC2-1	429203	4539177	6400	Medium-grained amphibolite
FCC3-1	428276	4539307	6260	Mica-rich amphiboloite w/ quartzite lens
FCC4-1	426592	4539340	6420	Fine-grained amphibolite
FCC4-2	426592	4539340	6420	Coarse-grained amphibolite
FCC4-3	426592	4539340	6420	Medium-grained gneiss
FCC5-1	428210	4554377	4800	Coarse-grained felsic gneiss
FCC5-2	428210	4554377	4800	Coarse-grained amphibolite
FCC5-3	428210	4554377	4800	Granite/pegmatite
FCC5-4	428210	4554377	4800	Medium-grained amphibolite
FCC6-1	429372	4527998	5800	Medium-grained amphibolite
FCC6-2	429372	4527998	5800	Granite/pegmatite
FCC7-1	429750	4528131	6000	Fine-grained amphibolite
FCC7-2	429750	4528131	6000	Coarse-grained amphibolite
FCC7-3	429750	4528131	6000	Quartzite
FCC7-4	429750	4528131	6000	Quartzite
FCC8-1	428903	4529299	6360	Felsic amphibolite
FCC8-2	428903	4529299	6360	Felsic amphibolite
FCC8-3	428903	4529299	6360	Felsic schist
FCC9-1	432344	4529780	7800	Amphibolite
FCC9-2	432344	4529780	7800	Amphibolite
FCC10-1	432599	4530087	7950	Fine-grained amphibolite
FCC10-2	432599	4530087	7950	Coarse-grained amphibolite
FCC11-1				Quartzo-feldpathic gneiss
FCC12-1	428229	4529597	5230	Felsic gneiss
FCC13-1	427467	4530015	4860	Quartzite
FCC14-1	427799	4529937	5285	Quartzite
FCC14-2	427799	4529937	5285	Coarse-grained amphibolite
FCC15-1	427947	4529776	5267	Quartzite
FCC15-2	427947	4529776	5267	Amphibolite
FCC15-3	427947	4529776	5267	Amphibolite
FCC16-1	428090	4529570	5180	Amphibolite
FCC19-1	428296	4539812	6488	Coarse-grained amphibolite
FCC19-2	428296	4539812	6488	Schist
FCC20-1	428426	4539708	6096	Coarse-grained amphibolite
FCC23-1	429172	4539205	6420	Medium-grained amphibolite
FCC25-1	433186	4531183	8200	Coarse-grained amphibolite
FCC26-1	432620	4531637	8250	Schist-gneiss
FCC26-2	432620	4531637	8250	Gneiss
FCC28-1	431738	4532988	8680	Coarse-grained amphibolite
FCC29-1	431482	4534015	9030	Amphibolite
FCC29-2	431482	4534015	9030	Granite/pegmatite
FCC30-1	430874	4534774	9070	Amphibolite
FCC30-2	430874	4534774	9070	Quartzite
FCC30-3	430874	4534774	9070	Amphibolite
FCC30-4	430874	4534774	9070	Schistose looking Amphibolite

Table 2-1. Table showing locations of samples in UTM meters Zone12N (NAD 1929).

Sample #	Meters E	Meters N	Elevation (ft)	Description
FCC31-1	430991	4535231	8950	Medium-grained amphibolite
FCC32-1	427625	4539156	5800	Medium-grained amphibolite
FCC33-1	427462	4539216	5860	Granite/pegmatite
FCC33-2	427462	4539216	5860	Amphibolite
FCC33-3	427462	4539216	5860	Quartzite
FCC33-4	427462	4539216	5860	Quartzite
FCC34-1	428044	4539241	6120	Medium-grained amphibolite
FCC35-1	428312	4539306	6000	Fine-grained amphibolite
FCC35-2	428312	4539306	6000	Quartzite
FCC36-1	428307	4539326	6000	Quartzite
FCC36-2	428307	4539326	6000	Fine-grained felsic amphibolite
FCC37-1	429982	4538818	6760	Quartzite
FCC38-1	430076	4538707	6580	Quartzite
FCC38-2	430076	4538707	6580	Amphibolite
FCC38-3	430076	4538707	6580	Quartzite
FCC39-1	434350	4528084	8270	Coarse-grained amphibolite
FCC39-2	434350	4528084	8270	Coarse-grained amphibolite
FCC39-3	434350	4528084	8270	Micaceous quartzite
FCC40-1	434090	4527110	8560	Quartzite
FCC40-2	434090	4527110	8560	Medium-grained amphibolite
FCC41-1	434246	4527234	8602	Quartzite
FCC41-2	434246	4527234	8602	Amphibolite
FCC42-1	433468	4526987	8320	Amphibolite
FCC42-2	433468	4526987	8320	Amphibolite
FCC42-3 A	433468	4526987	8320	Quartzite
FCC42-3 B	433468	4526987	8320	Quartzite with fuchsite
FCC42-4	433468	4526987	8320	Schist
FCC44-1	435110	4526623	8540	Quartzite
FCC45-1	425725	4554082	4780	Medium-grained amphibolite
FCC46-1	425839	4554030	4840	Quartzite
FCC46-2	425839	4554030	4840	Amphibolite
FCC46-3	425839	4554030	4840	Gneiss
FCC46-4	425839	4554030	4840	Amphibolite
FCC47-1	427831	4554491	4200	Amphibolite
FCC50-1	434324	4524878	8720	Quartzo-feldpathic gneiss/schist
FCC52-1	433965	4524856	8610	Amphibolite
FCC52-2	433965	4524856	8610	Gneiss
FCC53-1	433868	4524836	8630	Amphibolite
FCC54-1	433688	4524896	8680	Quartzite
FCC55-1	433692	4525499	7880	Felsic amphibolite
FCC56-1	433577	4526045	7020	Amphibolite
FCC56-2	433577	4526045	7020	Quartzite
FCC57-1	433713	4526056	7090	Schist
FCC60-1	433018	4531583	8390	Amphibolite
FCC61-1	432603	4532164	8680	Schist
FCC61-2	432603	4532164	8680	Fine-grained amphibolite
FCC61-3	432603	4532164	8680	Amphibolite
FCC61-4	432603	4532164	8680	Schist
FCC61-5	432603	4532164	8680	Schist

Table 2-1. Table showing locations of samples in UTM meters Zone12N (NAD 1929).

Sample #	Meters E	Meters N	Elevation (ft)	Description
FCC61-6	432603	4532164	8680	Schist
FCC62-1	432359	4532299	8666	Coarse-grained amphibolite
FCC63-1	432359	4532330	8666	Coarse-grained amphibolite
FCC63-2	432359	4532330	8666	Quartzite with schist
FCC65-1	431597	4532814	8510	Quartzite
FCC65-2	431597	4532814	8510	Medium-grained amphibolite
FCC67-1	431117	4532935	8310	Quartzite
FCC69-1	431712	4532854	8430	Quartzite
FCC70-1	428628	4538932	5770	Medium-grained amphibolite
FCC71-1	428536	4539118	5860	Quartzite
FCC72-1	429214	4538896	5790	Amphibolite looking schist
FCC74-1	422370	4561508	5280	Amphibolite
FCC74-2	422370	4561508	5280	Amphibolite
FCC75-1	422213	4561676	5220	Amphibolite
FCC77-1	432335	4531800	8250	Gneiss
FCC79-1	432583	4532063	8740	Amphibolite
FCC79-2	432583	4532063	8740	Gneiss
FCC81-1	432560	4537095	7380	Quartz-rich amphibolite
FCC82-1	432707	4530192	7970	Amphibolite
FCC88-1	432308	4532811	8680	Granite
FCC88-2	432308	4532811	8680	Amphibolite
FCC88-3	432308	4532811	8680	Feldspathic quartzite
FCC88A-1	432299	4532948	8740	Quartz/schist-rich amphibolite
FCC89-1	432358	4533015	8760	Amphibolite
FCC90-1	432375	4532999	8720	Medium-grained amphibolite
FCC91-1	432271	4533061	8830	Gneiss
FCC93-1	432175	4533153	8800	Quartzite
FCC93-2	432175	4533153	8800	Qtz rich UM?
FCC97-1	431736	4533363	8890	Quartzrich-Schist/Gneiss
FCC97-2	431736	4533363	8890	Amphibolite
FCC97-3	431736	4533363	8890	Quartzite
FCC100-1	431663	4533640	8915	Quartzite
FCC101-1	431659	4533664	8930	Amphibolite
FCC103-1	431659	4533721	8940	Amphibolite
FCC103-2	431659	4533721	8940	Amphibolite Gneiss
FCC105-1	431609	4533805	9030	Amphibolite
FCC107-1	431517	4533963	9100	Amphibolite
FCC108-1	431390	4534542	9060	Brecciated quartzite
FCC109-1	431383	4534692	9130	Medium-grained amphibolite
FCC110-1	431389	4534746	9210	Felsic amphibolite
FCC114-1	429298	4544281	8940	Amphibolite
FCC114-2	429298	4544281	8940	Granite/pegmatite
FCC115-1	429670	4544299	8945	Amph/ gneiss
FCC115-2	429670	4544299	8945	Amph/ gneiss
FCC115-3	429670	4544299	8945	Quartzite
FCC115-4	429670	4544299	8945	Amph/ gneiss
FCC116-1	429719	4542800	9313	Quartzite rich gneiss
FCC117-1	429729	4542581	9290	Amphibolite/ Gneiss
FCC118-1	429717	4542444	9260	Amph/ schist

Table 2-1. Table showing locations of samples in UTM meters Zone12N (NAD 1929).

Sample #	Meters E	Meters N	Elevation (ft)	Description
FCC119-1	429640	4542316	9240	Gneiss
FCC120-1	429619	4542080	9196	Amphibolite
FCC120-2	429619	4542080	9196	Amphibolite
FCC122-1	422502	4558164	5210	Ultramafic
FCC122-2	422502	4558164	5210	Ultramafic
FCC122-3	422502	4558164	5210	Amphibolite
FCC122-4	422502	4558164	5210	Quartzite
FCC122-5	422502	4558164	5210	Ironstone/ BIF
FCC123-1	422538	4558265	5230	Schist looking amphibolite
FCC123-2	422538	4558265	5230	Peridotite looking amphibolite
FCC124-1	422714	4557629	5410	Amphibolite
FCC124-2	422714	4557629	5410	Amphibolite
FCC124-3	422714	4557629	5410	Fine-grained hornblendite/ ultramafic
FCC124-4	422714	4557629	5410	Ultramafic
FCC125-1A	422799	4557639	5520	Quartzite
FCC125-1B	422799	4557639	5520	Quartzite
FCC125-1C	422799	4557639	5520	Quartzite
FCC128-1	427482	4539245	5910	Medium-grained amphibolite
FCC129-1	427795	4539398	6020	Felsic amphibolite
FCC130-1	427820	4539319	5800	Amphibolite
FCC131-1	428173	4539242	6085	Amphibolite
FCC131-2	428173	4539242	6085	Amphibolite
FCC132-1	432271	4538296	7500	Schist
FCC133-1	432295	4538344	7565	Quartz-rich schist
FCC143-1	429686	4542146	9040	Fine-grained amphibolite
FCC146-1	429607	4541534	9140	Fine-grained amphibolite
FCC148-1	430002	4537173	8295	Amphibolitic-Gneiss
FCC148-2	430002	4537173	8295	Amphibolitic-Gneiss
FCC149-1	430437	4536676	8496	Amphibolite
FCC152-1	430725	4534544	8870	Quartzite
FCC152-2	430756	4534509	8840	Quartzite
FCC154-1	430855	4534400	8660	Amphibolite
FCC156-1	431243	4533205	8475	Medium-grained amphibolite
FCC162-1	429467	4525662	5250	Quartzite
FCC163-1	429707	4525752	5355	Amphibolite
FCC163-2	429707	4525752	5355	Quartzite
FCC165-1	430255	4525890	5550	Quartzite
FCC165-2	430255	4525890	5550	Amphibolite
FCC167-1	431028	4525997	5810	Quartzite
FCC171-1	427654	4539078	5520	Amphibolite
FCC171-2	427654	4539078	5520	Schist
FCC172-1	428240	4239603	6430	Felsic schist
FCC175-1	428155	4539626	6625	Quartzite
FCC175-2	428155	4539626	6625	Quartzite
FCC175-3A,B	428155	4539626	6625	Banded Amph/Quartzite
FCC177-1	429334	4539537	6960	Coarse-grained amphibolite
FCC178-1	429316	4539522	6900	Schisty-looking amphibolite

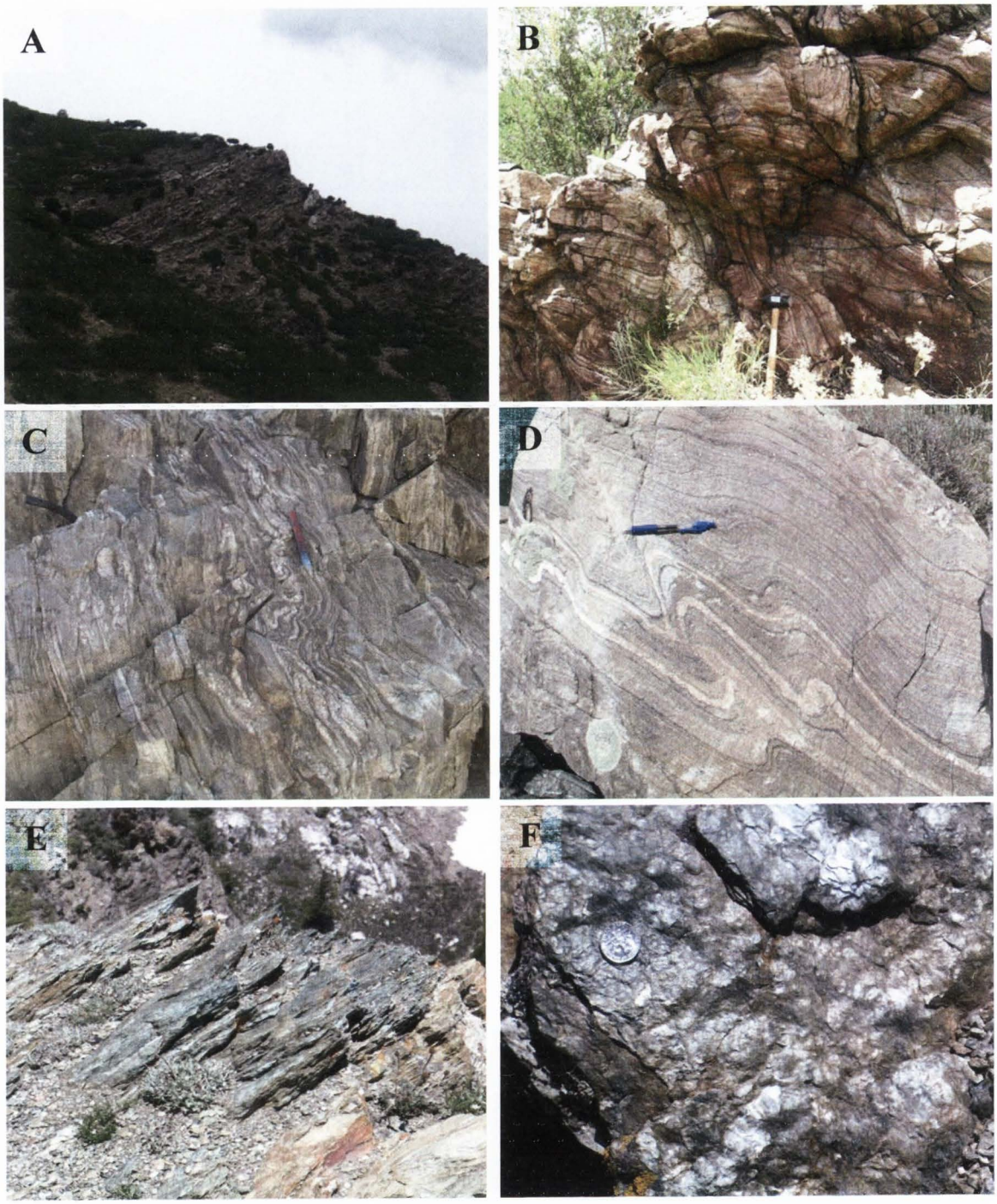

Figure 2-6. Farmington Canyon gneiss field photos. (A) Bold outcrops on ridges and in canyons,Typical layered outcrop of foliated gneiss in Farmington Canyon. (B) Folded layers of felsic gneiss of the FCC (note the small granite intrusion left of hammer). (C) Mafic layered gneiss (D) Felsic gneiss of the FCC with shear folds showing common top to North shear sense. (E) Outcrop of quartz-rich chlorite schist of the FCC, near Francis Peak. (F) Close-up of quatz-rich chlorite schist (photo E) showing foliation plane surface.

Schist

Associated with the gneiss is minor schist (Fig 2-6 E,F). These schists vary widely in amounts of chlorite, quartz, altered feldspar, and mafic minerals. Most schist units are rich in quartz and contain varying amounts of garnet, biotite, chlorite, sericite, sillimanite (up to 20%), and are more abundant in biotite than the gneiss units. Muscovite is common in the southern gneiss and schist unit of the FCC, but is absent in the northern portion (Bryant, 1988a). Discrete bodies of mica schist with large, distinct flakes (2-4 cm) of muscovite or chlorite are widely distributed (Fig 2-6E). Some schist units contain garnet and others display S-C fabrics with top to the north (Fig 2-6E). Bryant (1988a) states that the schists represent immature shales and possibly sandstone as protoliths.

Amphibolite

Amphibolite lenses (Fig 2-7 A-C,E-F) are widespread and occur in two varieties: (1) as large lensoid layers up to 4 km x 300 m, but are generally less than 500 m long and 10 m thick, and (2) as deformed or boudinaged dikes or sills in gneiss, quartzite, and even older amphibolites. Based on geochemistry the amphibolite dikes can be subdivided into 3 groups, and will be discussed in more detail in the following chapters. Amphibolites appear to be more common within the quartzites rather than within the gneisses and schists. Amphibolites are generally non-layered, and have sharp contacts with the surrounding rock units. Amphibolite units may be cut by less abundant pegmatites. Mineral assemblages include hornblende (45-70%) and plagioclase (30-40%), ± clinopyroxene, which can be locally altered to actinolite, quartz (up to 8%), and

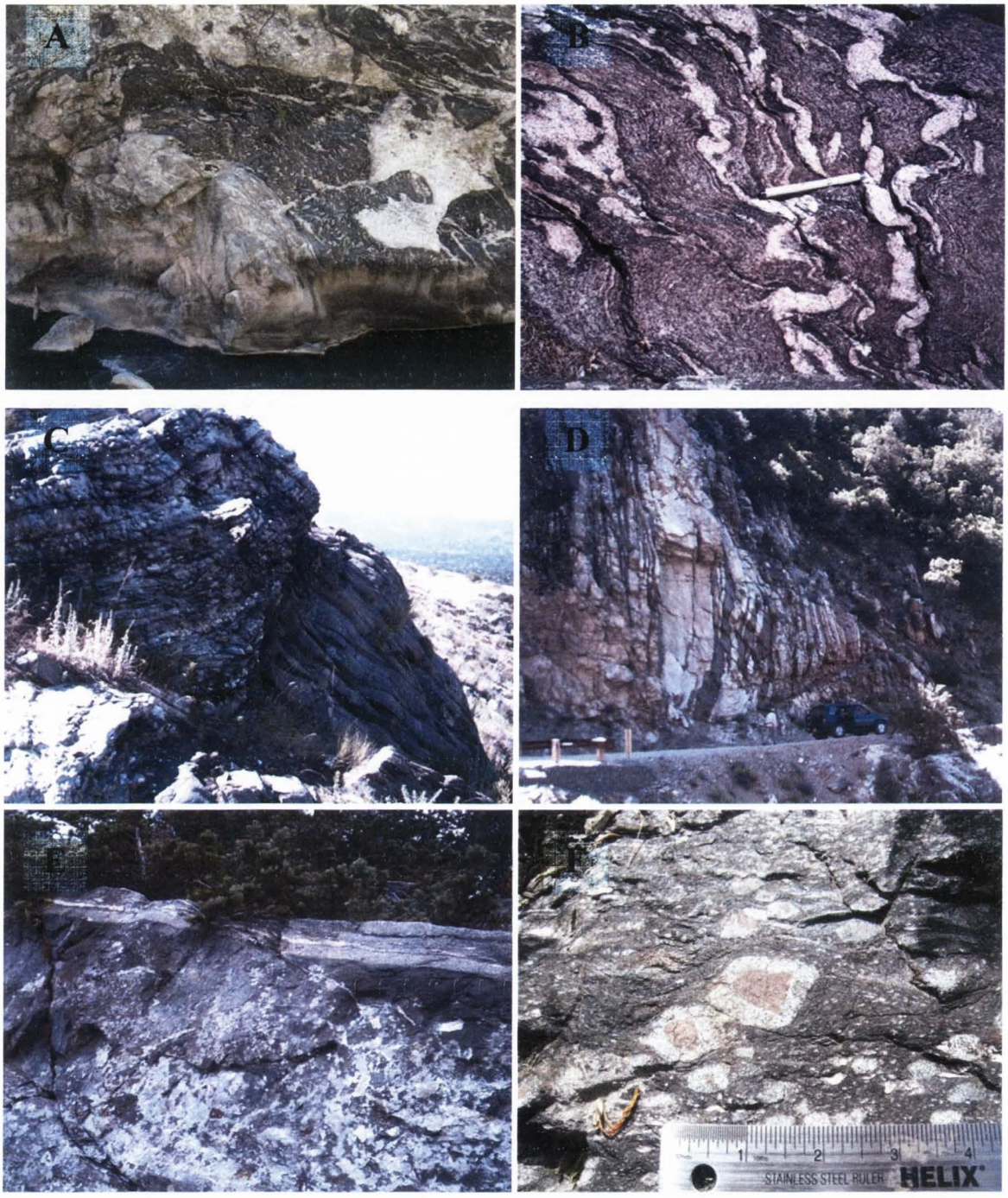

Figure 2-7. Boudinaged amphibolite (dikes?) and migmatitic felsic gneisses which are intruded by massive unfoliated plag/K-spar pegmatites in Weber Canyon. (A) Migmatitic amphibolite of the FCC. (B) Close-up of Farmington Canyon amphibolite. (C) Amphibolite overlain discordantly by quartzite. (D) Amphibolite dikes which intrude through quartzite (E) Amphibolitic dike (top) which has intruded through an amphibolite knocker (bottom) below Bountiful Peak. (F) Garnet amphibolite with large garnets surrounded by plagioclase-hornblende rims formed in response to decreased pressure or elevated temperature, Session Mountains, Utah.

garnet. Most amphibolites are medium grained and are granoblastic to nemanoblastic in texture, and some are highly lineated and contain lenses of plagioclase and quartz, suggested by Bryant (1988a) as being a relict gabbroic texture. The amphibolites in the northern part of the FCC is generally richer in monoclinic pyroxene, and is contemporaneous with the hornblende.

Ultramafics

Large lensoid outcrops of ultramafic rock (Fig 2-8 A-D), commonly associated with amphibolite and quartzite, are found near Ogden and on Antelope Island are associated with ultramafic bodies (Yonkee et al., 2000). The three largest ultramafic lenses include: (1) a lens on Antelope island which is 80 m x 20 m, (2) a large outcrop in Beus Canyon, which is about 120 m by 80 m; (this outcrop forms a composite block with quartzite along the eastern margin, and both the quartzite and ultramafic rocks are surrounded by gneiss), and (3) a 100 m x 30 m block in Burch Creek Canyon near Ogden, which is associated with a 20 m thick quartzite layer.

Other ultramafic bodies have been found in the Wasatch Mountains. Some have a schistose appearance, while others appear to grade into a mafic gneiss. The ultramafic block in Burch Creek has inclusions of pyroxene-amphibole-rich ultramafic rock that have been altered to serpentinite (antigorite) within the gneiss, however, the contacts between the two units are not clear. In Beus Canyon, amphibolites are in gradational contact with ultramafic rocks containing serpentine (antigorite), clinopyroxene, and anthophyllite. Additionally, this unit also has a 2-3 m quartzite layer with a 10 cm thick iron-rich layer that somewhat resembles a BIF. Ultramafic lenses in the FCC consist of

Figure 2-8. Farmington Canyon ultramafic field photos. (A) Composite knocker of komatiite (under hammer), amphibolite (halfway up slope), and quartzite (chert?) (top of slope) in Farmington Canyon Complex near Ogden, Utah. (B) Closeup of komatiite surface (see photo A) showing weathered serpentinite-like texture (C) Large antigorite-rich ultramafic block near Ogden, Utah (D) Closeup of photo C, showing serpentinite-like texture. (E) (F) Close-up of anthophyllitic texture in ultramafics (note shear fabric).

serpentine (antigorite), orthopyroxene with minor clinopyroxene, anthophyllites and amphiboles.

Greenschist facies overprint is easily seen in the ultramafic rocks and is recognized easily in shear zones throughout the FCC, however, it is not as well distinguished elsewhere in the FCC. Cataclasis from shearing and retrograde metamorphism is probably related to the Sevier Orogeny (Bell, 1951), and is not consistent with the amphibolite-grade metamorphism of the surrounding gneiss (Bryant et al., 1988a).

Quartzite

Quartzites (Fig 2-9) are generally white to pale greenish grey in color and form blocks, typically ~10-20 m thick and ~100 m in length. Some quartzites can be quite large, such as the quartzites in the Sessions Mountains to the southeast of Bountiful, which can be 100-200 m thick and up to ~3.4 kilometers in length with 0.3 to 10 cm thick intercalated amphibolite layers (Fig 2-5). Quartzites are more common south of Francis Peak and generally have thicker (20-60 cm) layers. In many outcrops, the amphibolite and quartzite have the same foliation orientations and appear together in distinct meter to decameter scale "blocks". Most quartzite units are associated with fuchsite and some are Fe-rich. The quartzites have no visible relict sedimentary structures such as bedding or crossbeds, however there is centimeter-scale to massive layering defined by the alignment of mica grains, and have a felspathic component with minor muscovite and/or fuchsite, which give the appearance of layering. Bryant (1988a) suggests that this is compositional layering. Feldspathic quartzites are very numerous

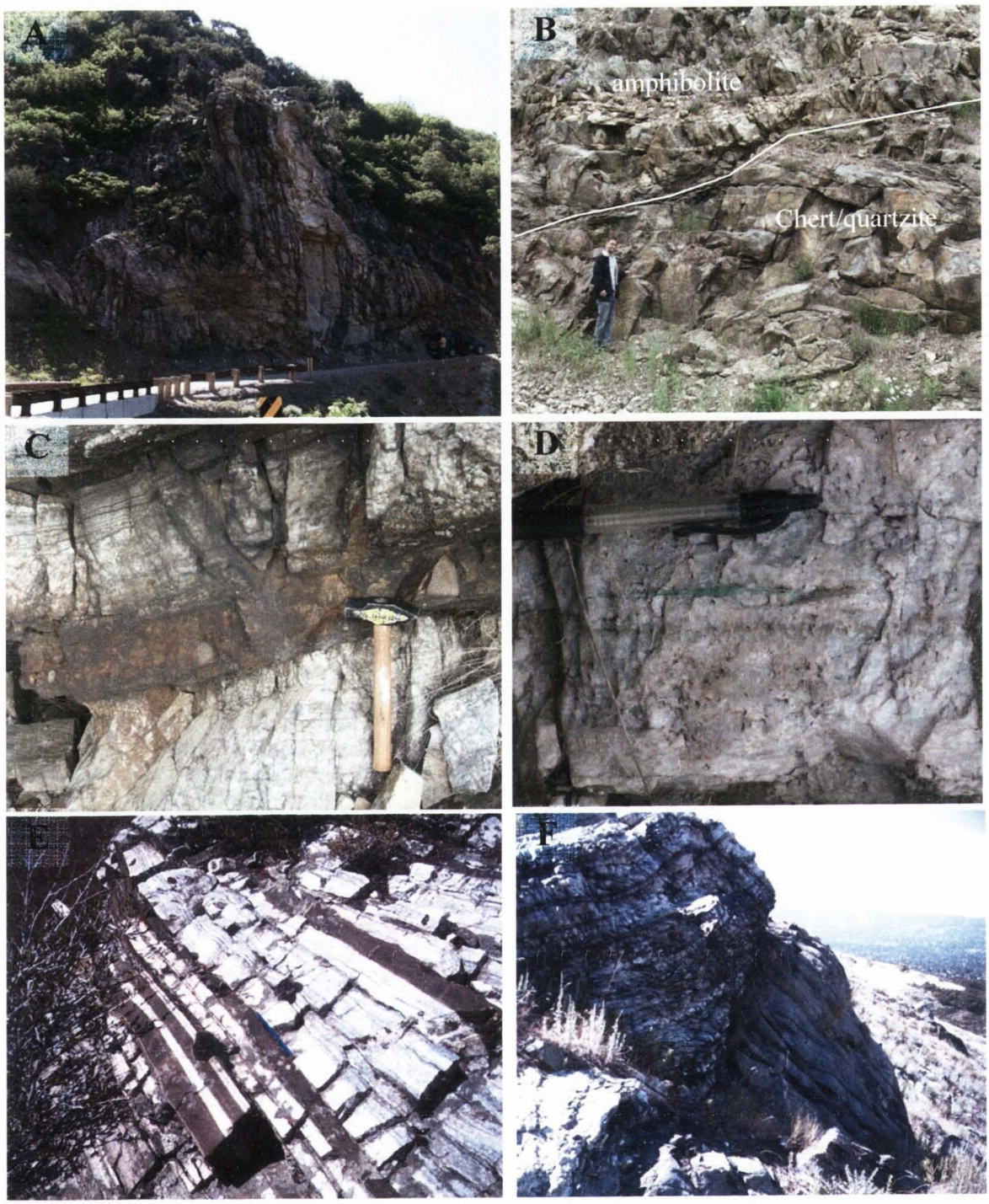

Figure 2-9. Farmington Canyon quartzite field photos. (A) Large knocker of banded quartzite (chert), cut by amphibolite dikes, in Farmington Canyon, Utah. (B) Composite knocker of amphibolite (upper part of outcrop) and quartzite (lower part of outcrop), Centerville Canyon, white line denotes approximate boundary. (C) Quartzite outcrop of a composite knocker near Ogden, Utah, showing a ~20 cm thick layer of ironstone. (D) Close-up of typical quartzite with green fuchsite layer in Sessions Mountains (note faint bedding laminations). (E) Quartzite layers with interbedded schist partings in Farmington Canyon. (F) Composite knocker of quartzite (top of outcrop) and amphibolite (bottom of oucrop) in Centerville Canyon. Contact is sharp and quartzite is overlain by amphibolite above (not shown in photo).

and commonly found near the contacts of quartzite, schist and gneiss. Some quartzite layers (5-15 cm) are observed to be intercalated with schists (1-3 cm) and are commonly associated with associated amphibolite outcrops. Some quartzite layers have sharp contacts, while others are gradational with schist and gneiss.

Granites and Pegmatites

Granitic rocks of the FCC (Fig 2-10) form two distinct groups: (1) granite containing pale grey feldspar, quartz, and mafic minerals, and commonly a weak metamorphic fabric (quartz-monzonite of Bryant (1988a)), and (2) granite plutons and stocks, with no metamorphic fabrics, containing quartz, and two feldspars (creamy white plagioclase and more abundant pink orthoclase), and muscovite with the possibility of a mafic phase. Textures vary from coarse-grained hypidiomorphic granular to pegmatitic, with little to no metamorphic fabrics. The granitic plutons, stocks and pegmatite bodies were all mapped as granite in this study.

The "quartz monzonite" mapped by Bryant (1988a) is classified as granite using the IUGS classification that is now standard (LeMaitre, 2002), but lies outside the detailed map areas of this report. The quartz monzonite is weakly foliated, and one large (2 km) long pluton at the head of Burch Canyon near Ogden, has been dated by Hedge et al., (1983) at 1.79 Ga using K-Ar ages from biotite.

Pegmatite bodies of pink granite can be as large as 200 m thick and 700 m long. The concordant pegmatites show gradational contacts, but concordant and discordant pegmatites may show either gradational or sharp contacts. Pegmatites show foliations defined by biotite minerals where cut by shear zones. Some pegmatites occur in thin

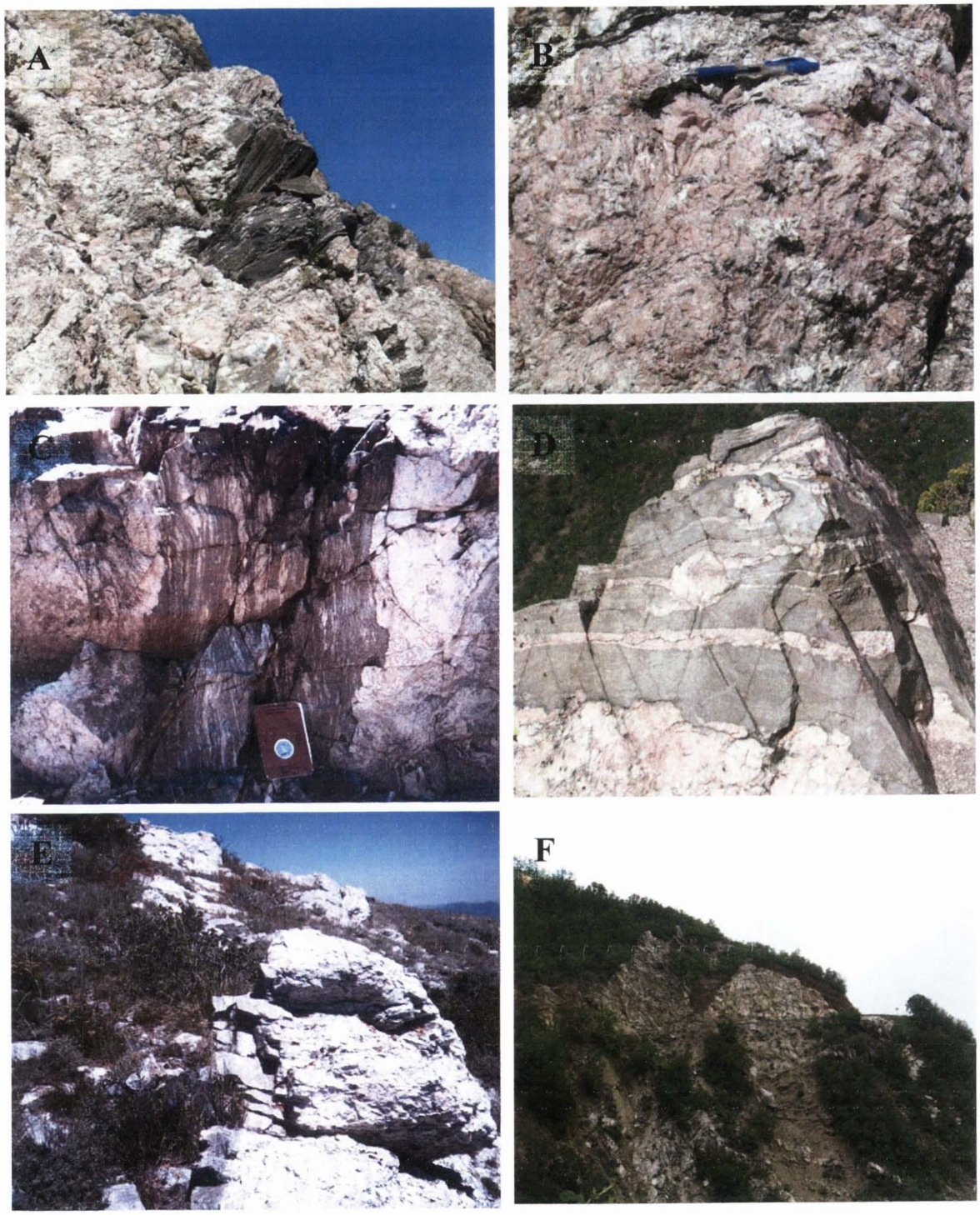

Figure 2-10. Farmington Canyon granite field photos. (A) Foliated gneiss block which has been brought up from depth by the surrounding pegmatite. (B) Close-up of previous pegmatite (photo A) showing texture and high orthoclase content. (C) Granite intruding alongside amphibolitic gneiss near Francis Peak. (D) Pegmatite intruding in gneiss near Bountiful Peak. (E) 3 m wide granite sill intruding between amphibolite to the left and quartzite on the left of photo. (F) Large granite intrusions of Centerville Canyon which intrudes through altered amphibolites.

stringers and pods (2-8 cm thick) with indistinct contacts. Pegmatites contain quartz, plagioclase, and microcline in varying proportions, and may contain garnet and/or biotite. Hornblende is common where the country rock contains abundant hornblende, such as is exposed at Devil's Gate.

CHAPTER 3

WHOLE-ROCK CHEMISTRY

METHODS

Selected samples of Farmington Canyon Complex were analyzed for major and trace elements via x-ray fluorescence spectrometry, electron microprobe, and ICP-MS. Selected quartzite and associated gneiss samples were analyzed for oxygen isotope data. Samples for analysis were selected based on the following criteria both in the field and laboratory. The first criterion, performed in the field, was to collect fresh, representative samples of each suite. To determine freshness in the field, properties such as fracturing and general appearance were used. To further sort samples in the laboratory, samples from each suite were more carefully analyzed using the previous qualities, as well as removing pieces of crushed samples that were largely altered that would not represent the original chemistry.

One hundred and twenty-six analyses were performed with a Philips PW 2400 XRF for major and trace element analysis by using pressed powder samples prepared with a 2% polyvinyl alcohol solution. Loss on Ignition (LOI) was performed by heating 2-3 grams of sample for three or more hours at 950° C. Machine calibration was performed using pressed powder standards from the USGS that were prepared with seven grams of unignited materials (Standards listed in the Appendix).

Ninety-one amphibolite and gneiss samples were analyzed for major element chemistry using fused bead electron microprobe analyses (FB-EMPA) (Shervais et al., 1990) on a Cameca SX 50 electron microprobe at Brigham Young University. Samples

were prepared by fusing 100-200 milligrams of powdered sample in a molybdenum crucible under an electric current, and then mounting the fused glass on probe mounts. Operating conditions for the beam were 15 kV and 10 nA. Calibration was performed using natural and synthetic standards from the National Museum of Natural History, including Juan de Fuca volcanic glass standard VG2 (Appendix). All values for the major elements given have been normalized to one hundred percent by weight (anhydrous) for plotting. Iron is reported as FeO*, which refers to the total analyzed iron reported as Fe^{2+}.

One-hundred and four samples were analyzed for REEs and other trace elements on a PerkinElmer ELAN 6000 ICP-MS (mass spectrometer) at Centenary College in Louisiana. Samples were prepared by weighing 0.1 gram of sample, and adding 6 ml of nitric acid (HNO_3) and 3 ml of hydrofluoric acid (HF) in a polyethylene test tube and heating to 95° C for 4 hours, until samples were dissolved and the solution had almost evaporated. The dissolved samples were then filled to 50 ml with 4% nitric acid and a 2 ml aliquot of the sample was spiked with 15μL of a prepared internal standard solution. The spiked aliquot solution was then diluted to 15 ml with 4% nitric acid. Machine calibration was performed using four standard solutions that were prepared with known values (Standards listed in Appendix A).

Major and trace element data for all samples are reported in Tables 3-1 to 3-5. The term Mg# as used in this thesis is defined by the following equation:

Mg# = 100*(MgO/40.32)/(MgO/40.32+FeO*/71.85) (Cox et al., 1979).

Twenty-nine selected samples of quartzite, amphibolite, and gneiss were sent to Southern Methodist University to be analyzed for oxygen isotopes. Amphibolite and gneiss samples were sent as powders for whole rock oxygen isotopes. Quartzite samples were crushed and sieved in order to obtain fine sand-sized grains, and individual quartz grains were hand selected to minimize contamination from lithics and feldspar. One fuchsite separate was analyzed for oxygen isotopes and deuterium (see Table 3-6).

RESULTS

Gneiss and schist

Thirty-four samples of schist and quartzo-feldspathic gneiss were analyzed for major elements, and twenty-nine of those samples were analyzed for trace element geochemistry, with compositions shown in Table 3-1. Gneiss and schist samples have a wide variation in composition: SiO_2 = 55-88%, FeO* = 0.9-15%, MgO = 0.1-6.8%, Al_2O_3 = 7-24%, and TiO_2 = 0.1-1.5%. Harker diagrams show that, as SiO_2 content increases, Al_2O_3, MgO, FeO*, CaO, TiO_2, and Na_2O all decrease, while K_2O increases (Fig 3-1). There is some compositional gradation between some of the more mafic gneisses with amphibolite, which can be seen in field relationships.

The Cr contents of the gneiss and schist ranged from 0-332 ppm and Ni content ranged from 5-100 ppm. Chondrite-normalized REE discrimination diagrams show that the gneiss and schist are enriched in light REEs and often show a negative europium anomaly, indicating plagioclase removal (Fig 3-2). Primitive mantle-normalized multi-element variation diagrams (spider diagrams) show a progressive enrichment in the more

Table 3-1. Major and Trace element analyses of Paragneiss and schist, Farmington Canyon Complex.

Sample#	FCC-4-3	FCC-5-1	FCC-8-3	FCC-11-1
Lithology	Paragneiss	Paragneiss	Paragneiss	Paragneiss
SiO2%	71.73	59.83	60.79	74.75
TiO2%	0.56	1.41	0.36	0.44
Al2O3%	13.79	13.98	18.31	13.32
FeO*%	5.78	14.54	8.47	3.62
MnO%	0.07	0.20	0.04	0.12
MgO%	0.42	0.67	6.80	0.48
CaO%	1.97	4.65	0.33	3.62
Na2O%	2.48	3.41		1.89
K2O%	3.05	0.79	4.62	1.67
P2O5%	0.14	0.52	0.13	0.08
MG#	11.64	7.62	54.17	19.29
Ti (ppm)	3358	8471	2162	2645
Nb_xrf (ppm)	42.7	46.2	45.9	29.6
Nb (ppm)	41.2	35.3	21.6	25.1
Zr (ppm)	600	1067	852	484
Y_xfr (ppm)	101	150	54	98
Y (ppm)	12	88	19	78
Sr (ppm)	65	102		136
Rb (ppm)	82	28	168	73
Rb_I (ppm)	38.7	31.1	87.4	67.0
Sc_xrf (ppm)	3.7	12.9	5.4	9.4
Sc (ppm)		16.5	10.7	4.7
V_xrf (ppm)	18	19	63	15
V (ppm)	7	20	43	8
Cr (ppm)	80		18	84
Cr_I (ppm)	0	9	1	1
Ni (ppm)	5	7	19	10
Co (ppm)	61.6	43.1	38.8	65.1
Cu (ppm)	39	3	1	19
Zn (ppm)	87	203	13	59
Ba_xrf (ppm)	1401	176	283	560
Ba (ppm)	723	165	163	544
La (ppm)	12.72	113.91	7.77	73.51
Ce (ppm)	23.37	558.98		144.00
Pr (ppm)	3.44	29.78	2.01	17.92
Nd (ppm)	13.41	113.36	7.97	67.63
Eu (ppm)	0.65	3.23	0.40	2.41
Sm (ppm)	3.09	23.25	2.13	14.26
Gd (ppm)	2.94	19.82	2.88	14.50
Tb (ppm)	0.46	3.59	0.62	2.46
Dy (ppm)	2.76	21.46	4.29	15.69
Ho (ppm)	0.56	4.30	0.93	3.38
Er (ppm)	1.67	11.79	3.00	9.74
Tm (ppm)	0.26	1.61	0.42	1.33
Yb (ppm)	1.83	9.51	2.55	7.92
Lu (ppm)	0.29	1.33	0.36	1.10
Hf (ppm)	0.11	0.48	0.18	0.15
Ta (ppm)	3.40	1.25	1.24	1.76
Pb (ppm)	35.28	20.09	4.82	22.87
Th (ppm)	4.96	35.36	32.23	22.98
U (ppm)	2.24	2.60	9.11	4.23
K (ppm)	25277	6565	38330	13831
Na (ppm)	18427	25260		14046

Table 3-1. Major and Trace element analyses of Paragneiss and schist, Farmington Canyon Complex.

Sample#	FCC-12-1	FCC-26-2	FCC-42-4	FCC-46-3	FCC-50-1
Lithology	Paragneiss	Paragneiss	Paragneiss	Paragneiss	Paragneiss
SiO2%	69.49	73.18	66.45	69.80	73.26
TiO2%	0.40	0.32	0.78	0.45	0.31
Al2O3%	16.33	13.63	17.01	13.09	12.14
FeO*%	2.23	3.79	6.93	6.91	6.03
MnO%	0.04	0.07	0.04	0.17	0.02
MgO%	0.97	0.13	3.94	0.37	0.93
CaO%	1.38	1.60	0.43	2.20	0.18
Na2O%	2.64	2.34	0.60	2.26	0.13
K2O%	6.42	4.54	3.61	4.51	6.96
P2O5%	0.07	0.06	0.08	0.23	0.05
MG#	44.43	5.54	43.33	8.82	21.54
Ti (ppm)	2391	1908	4651	2690	1860
Nb_xrf (ppm)	12.3	44.5	8.1	45.5	38.3
Nb (ppm)	13.4	42.8	7.8	47.5	37.5
Zr (ppm)	144	648	161	666	619
Y_xfr (ppm)	29	116	20	135	99
Y (ppm)	12	22	26	125	26
Sr (ppm)	325	66	37	102	18
Rb (ppm)	224	131	141	125	225
Rb_I (ppm)	190.0	88.3	129.5	123.5	128.9
Sc_xrf (ppm)	3.8	4.8	4.2	8.2	3.4
Sc (ppm)	3.7		13.7	7.7	1.4
V_xrf (ppm)	67	5	109	19	15
V (ppm)	45	2	82	5	7
Cr (ppm)	262	209	169	262	120
Cr_I (ppm)	33	0	124	1	0
Ni (ppm)	18	7	54	11	8
Co (ppm)	32.7	57.5	47.2	46.3	65.9
Cu (ppm)	15	4	2	3	1
Zn (ppm)	39	158	33	123	36
Ba_xrf (ppm)	1113	1666	298	1566	1328
Ba (ppm)	1631	1081	306	3607	1086
La (ppm)	24.87	32.95	36.35	111.37	30.12
Ce (ppm)	50.23	67.40	47.66	515.91	62.40
Pr (ppm)	5.93	9.16	5.99	28.25	12.91
Nd (ppm)	21.33	34.74	21.64	108.53	35.80
Eu (ppm)	1.30	1.28	1.12	4.14	1.18
Sm (ppm)	4.17	7.12	4.03	23.76	7.51
Gd (ppm)	3.26	6.26	3.48	22.39	4.79
Tb (ppm)	0.49	1.06	0.48	4.15	0.65
Dy (ppm)	2.75	6.33	2.74	26.10	3.51
Ho (ppm)	0.52	1.24	0.53	5.39	0.68
Er (ppm)	1.44	3.55	1.57	15.60	2.22
Tm (ppm)	0.22	0.50	0.21	2.25	0.35
Yb (ppm)	1.28	3.29	1.32	14.21	2.25
Lu (ppm)	0.18	0.50	0.20	2.09	0.36
Hf (ppm)	0.06	0.23	0.22	0.54	1.87
Ta (ppm)	1.49	2.62	0.84	3.36	2.19
Pb (ppm)	96.37	43.05	3.57	27.53	33.57
Th (ppm)	12.57	9.37	10.00	31.28	13.67
U (ppm)	8.45	3.32	2.30	2.56	2.45
K (ppm)	53295	37719	29963	37439	57784
Na (ppm)	19554	17327	4480	16767	936

Table 3-1. Major and Trace element analyses of Paragneiss and schist, Farmington Canyon Complex.

Sample#	FCC-52-2	FCC-57-1	FCC-61-1	FCC-61-4	FCC-91-1
Lithology	Paragneiss	Paragneiss	Paragneiss	Paragneiss	Paragneiss
SiO2%	75.35	59.95	63.34	55.42	71.60
TiO2%	0.35	0.84	0.78	1.51	0.88
Al2O3%	11.78	23.32	19.25	14.85	12.90
FeO*%	4.41	7.27	7.52	15.41	7.27
MnO%	0.15	0.04	0.07	0.23	0.09
MgO%	0.30	2.49	3.30	3.46	0.45
CaO%	1.47	0.06	2.88	7.71	2.63
Na2O%	1.62	0.14	2.09	0.38	1.39
K2O%	4.54	5.66	0.59	0.73	2.50
P2O5%	0.03	0.08	0.14	0.28	0.29
MG#	10.92	36.60	44.41	28.40	9.85
Ti (ppm)	2091	5033	4669	9034	5296
Nb_xrf (ppm)	40.3	9.3	11.8	9.5	50.0
Nb (ppm)	40.4	11.8	11.5	9.3	56.9
Zr (ppm)	615	125	153	148	727
Y_xfr (ppm)	106	30	28	47	133
Y (ppm)	91	8	9	45	71
Sr (ppm)	88	14	186	105	81
Rb (ppm)	137	279	27	33	98
Rb_I (ppm)	135.8	233.9	19.1	31.6	102.0
Sc_xrf (ppm)	3.6	7.9	11.9	27.8	7.1
Sc (ppm)	4.8	18.1	16.2	36.8	12.3
V_xrf (ppm)	29	149	158	401	23
V (ppm)	20	125	138	358	8
Cr (ppm)	247	208	216	35	215
Cr_I (ppm)	1	140	156	5	0
Ni (ppm)	6	70	100	24	6
Co (ppm)	49.9	55.2	75.8	113.0	105.5
Cu (ppm)	90	2	125	77	8
Zn (ppm)	118	61	137	125	132
Ba_xrf (ppm)	1676	394	345	163	1537
Ba (ppm)	3759	300	289	154	3412
La (ppm)	74.65	12.38	6.22	10.51	39.63
Ce (ppm)	420.69	25.87	13.01	31.16	83.48
Pr (ppm)	18.52	3.05	1.60	4.05	11.37
Nd (ppm)	68.90	11.36	6.31	18.66	45.42
Eu (ppm)	2.81	0.51	0.91	2.37	3.27
Sm (ppm)	15.00	2.25	1.55	5.59	10.69
Gd (ppm)	13.34	1.91	1.78	7.12	11.50
Tb (ppm)	2.71	0.28	0.34	1.30	2.24
Dy (ppm)	18.07	1.58	2.26	8.39	15.79
Ho (ppm)	3.95	0.30	0.46	1.80	3.50
Er (ppm)	12.39	0.75	1.32	5.39	10.37
Tm (ppm)	1.93	0.10	0.19	0.80	1.52
Yb (ppm)	12.68	0.60	1.20	5.23	9.66
Lu (ppm)	1.90	0.09	0.18	0.80	1.44
Hf (ppm)	0.74	0.50	0.17	0.65	0.25
Ta (ppm)	3.11	1.26	0.72	0.92	3.41
Pb (ppm)	32.21	7.27	22.35	11.64	52.69
Th (ppm)	29.08	4.95	2.41	4.85	12.33
U (ppm)	4.31	1.99	3.95	1.52	3.02
K (ppm)	37698	46948	4911	6072	20768
Na (ppm)	12030	1046	15512	2810	10300

Table 3-1. Major and Trace element analyses of Paragneiss and schist, Farmington Canyon Complex.

Sample#	FCC-116-1	FCC-117-1	FCC-148-2	FCC-172-1
Lithology	Paragneiss	Paragneiss	Paragneiss	Paragneiss
SiO2%	81.58	65.13	56.32	55.05
TiO2%	0.67	1.05	1.31	0.52
Al2O3%	7.18	14.17	21.75	24.39
FeO*%	6.59	9.98	7.30	4.41
MnO%	0.08	0.20	0.11	0.05
MgO%	2.58	0.72	3.18	2.40
CaO%	0.14	3.29	2.90	6.94
Na2O%	0.10	2.14	5.60	3.61
K2O%	0.79	2.95	1.32	2.44
P2O5%	0.21	0.31	0.18	0.15
MG#	37.03	11.32	43.93	49.75
Ti (ppm)	4046	6282	7878	3139
Nb_xrf (ppm)	8.3	57.1	21.8	9.8
Nb (ppm)	5.9	56.1	20.1	8.4
Zr (ppm)	89	847	243	223
Y_xfr (ppm)	26	154	53	26
Y (ppm)	26	110	20	34
Sr (ppm)	3	67	150	146
Rb (ppm)	32	196	51	109
Rb_I (ppm)	28.3	151.7	21.4	101.5
Sc_xrf (ppm)	7.7	9.3	11.8	12.7
Sc (ppm)	16.2	15.3	20.4	12.0
V_xrf (ppm)	98	22	216	99
V (ppm)	65	10	184	82
Cr (ppm)	49	332	151	86
Cr_I (ppm)	38		108	58
Ni (ppm)	33	12	71	31
Co (ppm)	46.3	6.0	35.7	39.5
Cu (ppm)	11	6	44	33
Zn (ppm)	67	190	69	28
Ba_xrf (ppm)	128	1089	307	407
Ba (ppm)	140	1037	241	415
La (ppm)	15.26	91.79	21.73	66.50
Ce (ppm)	39.48	435.49	41.41	147.68
Pr (ppm)	3.90	24.84	5.64	18.57
Nd (ppm)	15.44	95.58	21.75	69.71
Eu (ppm)	0.78	4.06	2.03	1.81
Sm (ppm)	3.37	19.80	4.85	12.94
Gd (ppm)	2.76	17.52	4.91	9.80
Tb (ppm)	0.39	3.33	0.84	1.12
Dy (ppm)	2.72	21.85	5.04	4.97
Ho (ppm)		5.01	1.01	0.83
Er (ppm)		15.52	2.87	2.08
Tm (ppm)	0.21	2.38	0.42	0.27
Yb (ppm)		15.57	2.75	1.58
Lu (ppm)	0.22	2.31	0.42	0.23
Hf (ppm)	0.43	0.31	0.10	0.11
Ta (ppm)	0.51	3.67	2.14	0.89
Pb (ppm)	12.01	30.82	21.24	21.27
Th (ppm)	3.45	30.25	11.39	15.77
U (ppm)	2.95	3.40	2.19	2.48
K (ppm)	6579	24475	10921	20289
Na (ppm)	758	15877	41537	26762

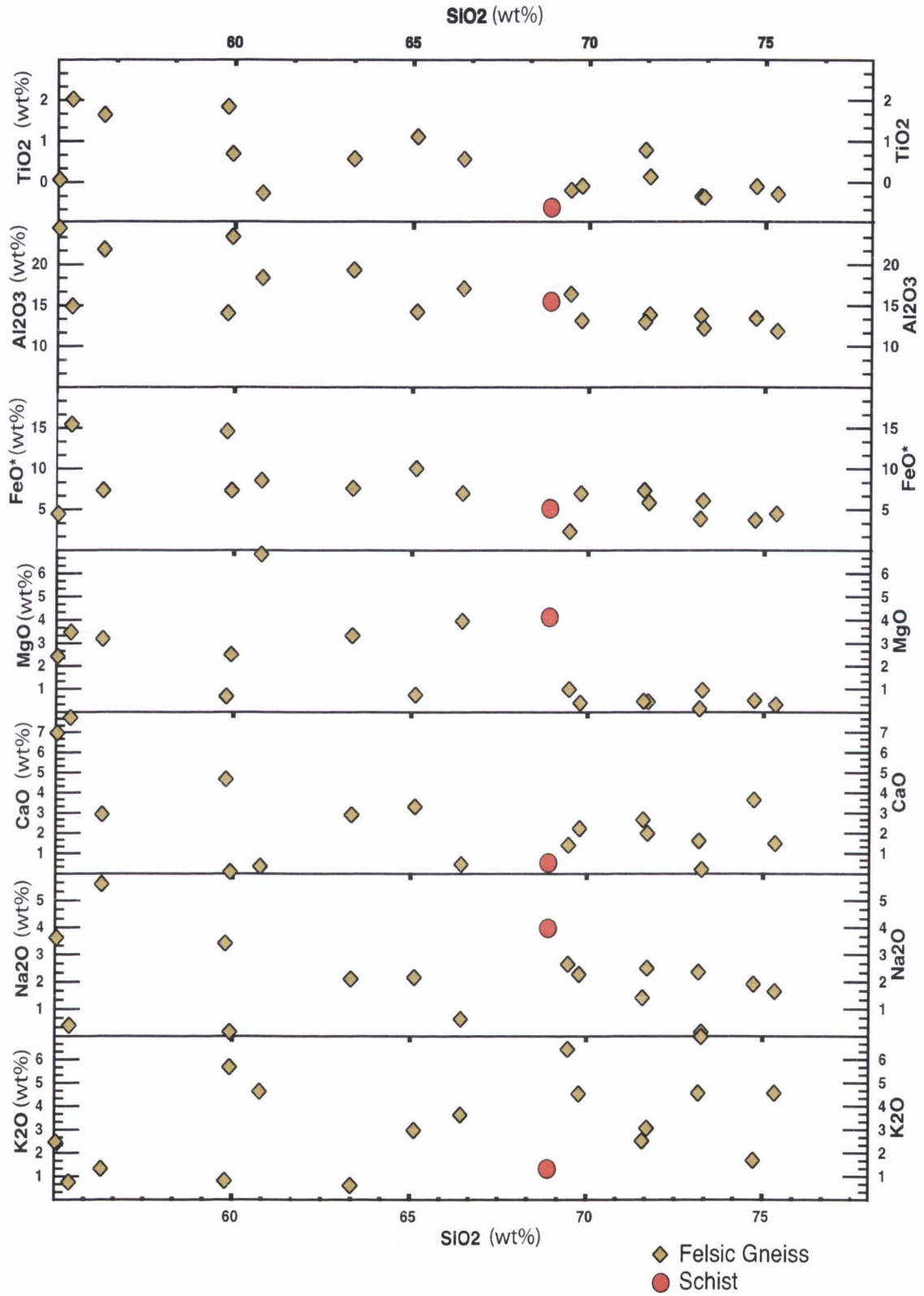

Figure 3-1. Harker variation diagram for gneiss and schist of the FCC.

incompatible elements, with significant depletions in K, Rb, Ba, Sr, Ti, and the transition metals (Fig 3-3).

Twelve gneiss/schist samples were analyzed for oxygen isotopes. The FCC gneiss/schist samples had $\delta^{18}O$ values between 4.0 and 9.5 SMOW (Table 3-6).

Amphibolite

Fifty-seven amphibolite samples were analyzed for major elements and forty-four samples were analyzed for trace elements by ICP-MS; compositions are shown in Table 3-2. The two major groups of amphibolites can be divided into four groups based on chemistry and field relations: (1) amphibolite blocks, (2) amphibolite dikes in gneiss or quartzite, (3) high-Al/ low-Ca amphibolites, which are mostly dikes, and (4) low-calcium amphibolites. The high-Al/ low Ca and low Ca groups are simply altered versions of the amphibolite dikes.

Amphibolites of the FCC have SiO_2 compositions ≈45-57%, and FeO* ≈ 8-19%. Total alkali-silica relations indicates that most of the amphibolites are mainly in the field of basalt and basaltic andesite. Amphibolite blocks have Mg-rich and normal tholeiitic compositions as shown on a Jensen diagram, whereas amphibolite dikes are Fe-tholeiites (Fig 3-4). The FeO*/(FeO*+MgO)- Al_2O_3 diagram indicates that most of the amphibolite blocks are a mixture of normal and Mg tholeiites, whereas the dikes are dominantly normal or Fe-rich (Fig 3-5).

MgO variation diagrams show that the amphibolite blocks have limited compositional variations, with MgO = 5-11.5%, TiO_2 = 0.5-2%. FeO*= 10-16%, Al_2O_3 = 11.5-18.5%, CaO= 8-13%, and Na2O= 1-3% (Table 3-2, Figs 3-6 through 3-13).

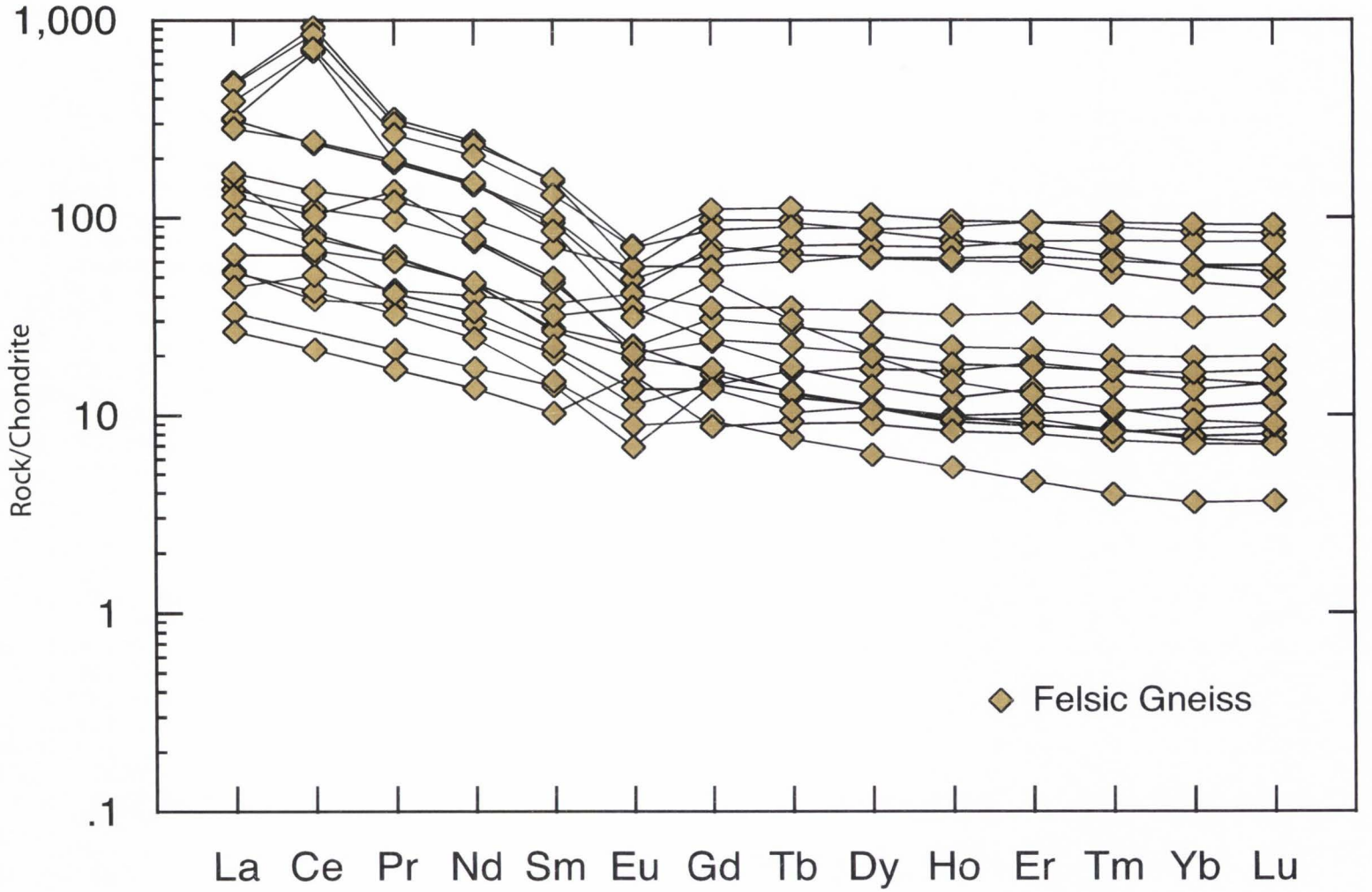

Figure 3-2. Chondrite normalized REE diagram for FCC felsic gneiss.

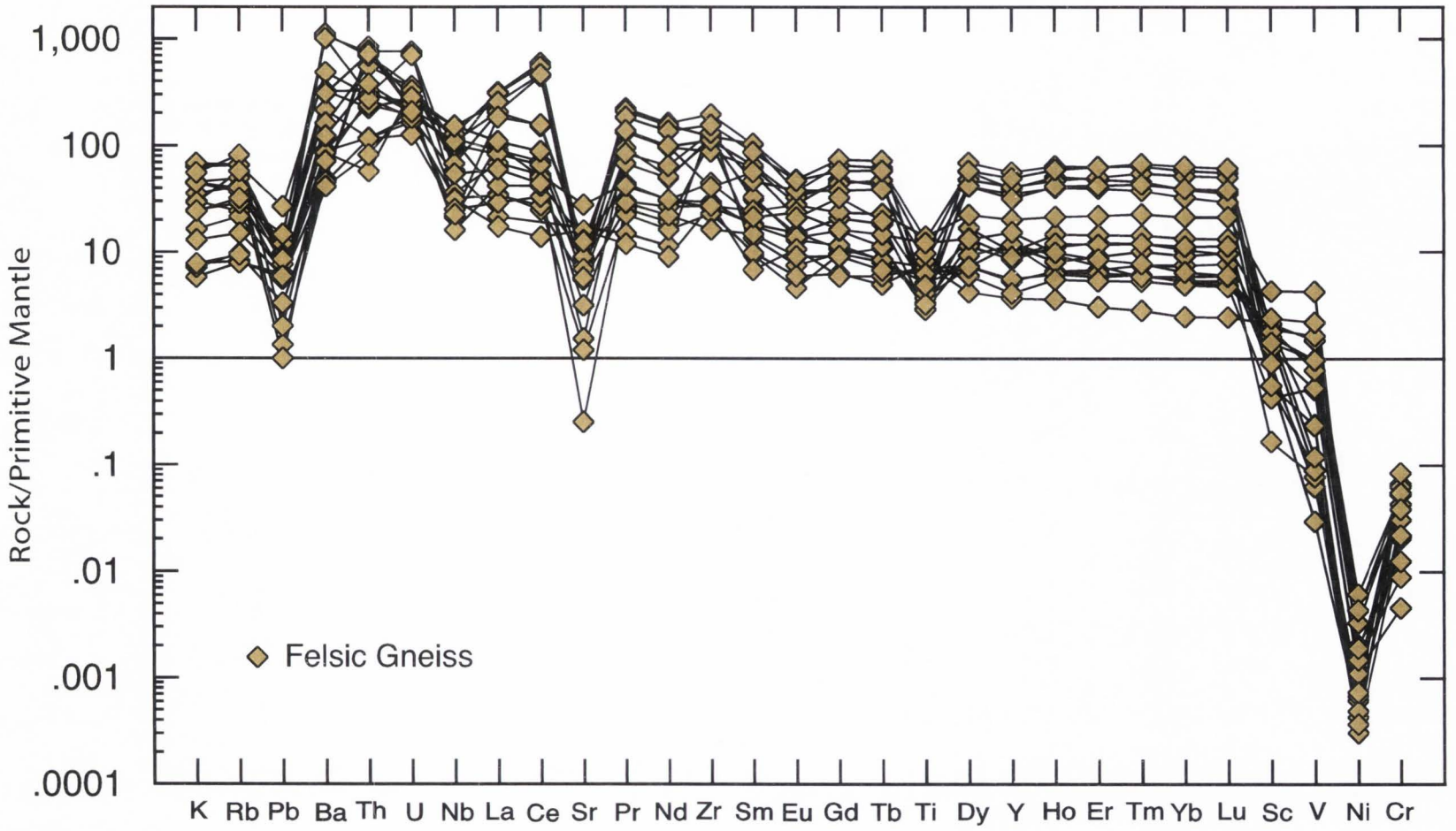

Figure 3-3. Primitive mantle normalized multi-element diagram for FCC felsic gneiss.

Table 3-2. Major and Trace element analyses of Amphibolites, Farmington Canyon Complex.

Sample#	FCC-2-1	FCC-7-1	FCC-9-2	FCC-10-1	FCC-10-2
Lithology	Amphibolite block	Amphibolite block	Amphibolite block	Amphibolite block	Amphibolite block
SiO2%	52.11	48.56	48.20	52.67	52.51
TiO2%	0.62	2.10	1.50	0.98	1.91
Al2O3%	11.54	15.42	15.10	14.29	15.35
FeO*%	11.59	14.35	13.33	11.61	14.24
MnO%	0.23	0.23	0.18	0.20	0.23
MgO%	11.12	8.07	7.57	6.40	4.89
CaO%	9.37	7.98	11.09	10.53	8.59
Na2O%	1.20	2.02	2.10	2.54	0.72
K2O%	1.56	1.02	0.57	0.59	1.00
P2O5%	0.49	0.20	0.35	0.16	0.53
MG#	63.57	50.20	50.71	49.29	37.64
Ti (ppm)	3734	12612	8970	5893	11468
Nb_xrf (ppm)	3.8	8.9	6.6	4.4	13.9
Nb (ppm)	3.5		4.3	3.1	
Zr (ppm)	70	113	75	58	250
Y_xfr (ppm)	17	22	19	19	51
Y (ppm)	15		6	20	
Sr (ppm)	43	134	203	159	96
Rb (ppm)	105	72	17	21	48
Rb_I (ppm)	86.1		6.7	19.7	
Sc_xrf (ppm)	27.3	26.4	33.9	33.2	25.2
Sc (ppm)	26.3		13.8	39.8	
V_xrf (ppm)	195	340	273	324	312
V (ppm)	179		253	303	
Cr (ppm)	883	262	281	43	134
Cr_I (ppm)	1531		188	23	
Ni (ppm)	206	114	115	45	62
Co (ppm)	55.8		47.9	47.9	
Cu (ppm)	11	60	103	204	73
Zn (ppm)	97	105	106	101	139
Ba_xrf (ppm)	400	132	206	120	79
Ba (ppm)	369		112	137	
La (ppm)	10.36		5.23	7.65	
Ce (ppm)	21.27		12.87	16.84	
Pr (ppm)	2.61		1.39	2.24	
Nd (ppm)	10.35		5.91	9.93	
Eu (ppm)	0.76		0.48	1.00	
Sm (ppm)	2.40		1.35	2.62	
Gd (ppm)	2.56		1.41	3.28	
Tb (ppm)	0.44		0.22	0.57	
Dy (ppm)	2.78		1.40	3.74	
Ho (ppm)	0.59		0.28	0.81	
Er (ppm)	1.74		0.82	2.41	
Tm (ppm)	0.25		0.11	0.35	
Yb (ppm)	1.63		0.72	2.31	
Lu (ppm)	0.25		0.11	0.35	
Hf (ppm)	0.71		0.59	0.93	
Ta (ppm)	0.28		0.30	0.28	
Pb (ppm)	9.49		6.66	4.20	
Th (ppm)	2.74		0.31	1.40	
U (ppm)	0.51		0.20	0.51	
K (ppm)	12988	8487	4759	4900	8297
Na (ppm)	8938	15022	15549	18810	5357

Table 3-2. Major and Trace element analyses of Amphibolites, Farmington Canyon Complex.

Sample#	FCC-25-1	FCC-28-1	FCC-29-1	FCC-30-1	FCC-30-3
Lithology	Amphibolite block	Amphibolite block	Amphibolite block	Amphibolite block	Amphibolite block
SiO2%	52.62	49.59	53.12	47.43	48.86
TiO2%	0.97	1.30	0.86	1.41	1.36
Al2O3%	14.57	14.85	15.03	12.70	14.16
FeO*%	11.55	14.16	10.53	15.72	13.44
MnO%	0.16	0.23	0.22	0.24	0.20
MgO%	6.55	5.79	6.99	9.56	8.29
CaO%	9.62	10.33	10.64	11.09	10.79
Na2O%	2.67	2.86	0.95	1.20	2.10
K2O%	1.07	0.57	1.44	0.51	0.48
P2O5%	0.20	0.26	0.17	0.14	0.26
MG#	50.56	41.61	54.23	52.56	52.00
Ti (ppm)	5794	7773	5163	8478	8163
Nb_xrf (ppm)	4.3	6.6	3.4	4.8	4.9
Nb (ppm)	2.6	4.7	2.3		4.2
Zr (ppm)	59	80	55	76	64
Y_xfr (ppm)	18	25	19	25	20
Y (ppm)	17	13	9		17
Sr (ppm)	181	192	150	98	163
Rb (ppm)	59	16	78	14	15
Rb_I (ppm)	54.0	8.9	27.9		11.9
Sc_xrf (ppm)	32.7	31.8	32.9	40.1	29.3
Sc (ppm)	38.0	28.5	24.3		29.3
V_xrf (ppm)	289	359	295	404	287
V (ppm)	269	340	266		259
Cr (ppm)	156	33	284	126	339
Cr_I (ppm)	7	8	39		196
Ni (ppm)	36	53	66	65	155
Co (ppm)	44.8	54.0	46.8		54.6
Cu (ppm)	117	168	75	11	34
Zn (ppm)	99	111	91	143	113
Ba_xrf (ppm)	282	130	175	127	129
Ba (ppm)	294	106	137		144
La (ppm)	6.81	8.19	4.56		11.48
Ce (ppm)	14.39	18.79	9.99		23.70
Pr (ppm)	1.97	2.39	1.34		2.98
Nd (ppm)	8.57	10.12	5.84		12.56
Eu (ppm)	0.87	0.85	0.55		1.10
Sm (ppm)	2.32	2.55	1.54		2.96
Gd (ppm)	2.83	2.87	1.79		3.38
Tb (ppm)	0.49	0.50	0.31		0.56
Dy (ppm)	3.26	3.12	2.00		3.48
Ho (ppm)	0.70	0.66	0.43		0.73
Er (ppm)	2.09	1.90	1.24		2.12
Tm (ppm)	0.31	0.27	0.17		0.31
Yb (ppm)	1.99	1.74	1.16		1.99
Lu (ppm)	0.30	0.26	0.17		0.31
Hf (ppm)	0.77	0.99	0.67		0.96
Ta (ppm)	0.22	0.40	0.20		0.34
Pb (ppm)	17.25	8.01	11.16		11.58
Th (ppm)	1.07	0.80	0.67		0.89
U (ppm)	0.31	0.33	0.28		1.21
K (ppm)	8847	4763	11913	4202	4024
Na (ppm)	19802	21247	7054	8931	15602

Table 3-2. Major and Trace element analyses of Amphibolites, Farmington Canyon Complex.

Sample#	FCC-30-4	FCC-39-2	FCC-40-2	FCC-42-1	FCC-42-2
Lithology	Amphibolite block	Amphibolite block	Amphibolite block	Amphibolite block	Amphibolite block
SiO2%	47.38	49.44	49.70	49.82	48.44
TiO2%	1.11	1.94	1.29	1.51	1.27
Al2O3%	16.62	14.56	14.04	14.35	14.09
FeO*%	11.80	12.81	13.81	12.57	12.25
MnO%	0.15	0.13	0.16	0.20	0.19
MgO%	8.61	7.32	7.39	8.37	9.90
CaO%	11.29	10.28	10.70	9.99	11.04
Na2O%	0.82	2.77	2.31	1.89	2.24
K2O%	1.90	0.43	0.35	1.03	0.37
P2O5%	0.28	0.28	0.20	0.25	0.18
MG#	56.67	50.17	49.26	54.69	59.55
Ti (ppm)	6649	11634	7706	9046	7611
Nb_xrf (ppm)	4.3	8.7	4.7	7.4	6.1
Nb (ppm)		7.9	3.8	6.6	4.2
Zr (ppm)	64	108	65	93	65
Y_xfr (ppm)	18	23	23	22	15
Y (ppm)		19	13	18	10
Sr (ppm)	155	219	140	138	192
Rb (ppm)	102	11	15	41	10
Rb_I (ppm)		7.7	8.5	26.2	4.8
Sc_xrf (ppm)	26.3	26.9	33.6	29.5	32.4
Sc (ppm)		23.5	28.2	22.1	18.9
V_xrf (ppm)	230	296	309	309	266
V (ppm)		281	276	282	231
Cr (ppm)	368	187	162	263	378
Cr_I (ppm)		163	105	310	322
Ni (ppm)	205	119	68	167	144
Co (ppm)		51.3	45.7	62.4	56.9
Cu (ppm)	3	52	173	58	31
Zn (ppm)	101	87	81	100	86
Ba_xrf (ppm)	322	85	33	84	74
Ba (ppm)		112	48	99	61
La (ppm)		10.65	4.47	10.81	5.97
Ce (ppm)		25.39	10.86	25.88	15.45
Pr (ppm)		3.69	1.56	3.55	2.11
Nd (ppm)		16.65	7.40	15.78	9.51
Eu (ppm)		1.42	0.88	1.37	0.89
Sm (ppm)		4.26	2.19	4.00	2.47
Gd (ppm)		4.57	2.76	4.32	2.58
Tb (ppm)		0.71	0.48	0.65	0.41
Dy (ppm)		4.24	3.05	3.86	2.40
Ho (ppm)		0.82	0.63	0.76	0.47
Er (ppm)		2.23	1.79	2.04	1.28
Tm (ppm)		0.30	0.25	0.28	0.17
Yb (ppm)		1.88	1.62	1.75	1.06
Lu (ppm)		0.28	0.24	0.25	0.15
Hf (ppm)		0.84	0.83	0.86	0.66
Ta (ppm)		0.50	0.29	0.56	0.35
Pb (ppm)		2.82	4.95	5.33	11.90
Th (ppm)		1.67	0.51	1.47	0.69
U (ppm)		0.43	0.30	0.53	0.26
K (ppm)	15783	3602	2885	8559	3035
Na (ppm)	6099	20513	17146	14022	16610

Table 3-2. Major and Trace element analyses of Amphibolites, Farmington Canyon Complex.

Sample#	FCC-55-1	FCC-60-1	FCC-62-1	FCC-70-1	FCC-74-1
Lithology	Amphibolite block	Amphibolite block	Amphibolite block	Amphibolite block	Amphibolite block
SiO2%	56.77	51.84	49.93	49.98	52.62
TiO2%	1.56	0.84	0.81	0.46	0.80
Al2O3%	12.16	14.92	14.49	12.05	16.16
FeO*%	11.20	11.20	11.60	11.12	10.31
MnO%	0.23	0.22	0.20	0.23	0.15
MgO%	7.12	7.72	9.18	10.39	6.09
CaO%	7.30	9.74	11.07	12.66	9.29
Na2O%	2.72	2.29	1.95	1.99	2.85
K2O%	0.66	1.05	0.54	0.93	1.53
P2O5%	0.22	0.18	0.20	0.04	0.19
MG#	53.22	55.05	59.30	57.85	51.32
Ti (ppm)	9325	5035	4875	2759	4767
Nb_xrf (ppm)	9.2	3.3	3.9	4.2	6.3
Nb (ppm)	6.9	2.4	2.5	2.0	5.3
Zr (ppm)	116	54	47	41	78
Y_xfr (ppm)	27	17	16	15	20
Y (ppm)	10	17	12	14	15
Sr (ppm)	101	129	178	228	245
Rb (ppm)	23	52	30	37	65
Rb_I (ppm)	11.8		18.0		29.7
Sc_xrf (ppm)	25.2	31.3	32.6	37.3	33.5
Sc (ppm)	12.7	40.1	35.2	37.6	27.0
V_xrf (ppm)	371	260	254	231	254
V (ppm)	277		243		217
Cr (ppm)	457	56	57	178	30
Cr_I (ppm)	244		42		17
Ni (ppm)	88	83	108	142	57
Co (ppm)	36.4		55.9		39.9
Cu (ppm)	59	92	68	18	106
Zn (ppm)	526	95	98	82	94
Ba_xrf (ppm)	139	214	143	229	240
Ba (ppm)	92	192	143	198	203
La (ppm)	6.62	6.68	4.68	7.70	11.66
Ce (ppm)	16.75	14.57	10.79	16.28	25.30
Pr (ppm)	2.26	1.97	1.42	2.13	3.16
Nd (ppm)	10.01	8.42	6.30	8.45	12.90
Eu (ppm)	0.69	0.86	0.65	0.81	0.84
Sm (ppm)	2.62	2.24	1.69	2.14	3.02
Gd (ppm)	2.77	2.80	2.04	2.52	3.24
Tb (ppm)	0.45	0.52	0.35	0.45	0.55
Dy (ppm)	2.58	3.24	2.28	2.55	3.42
Ho (ppm)	0.50	0.72	0.49	0.59	0.72
Er (ppm)	1.30	2.08	1.45	1.60	2.06
Tm (ppm)	0.18	0.31	0.20	0.26	0.29
Yb (ppm)	1.06	1.97	1.35	1.51	1.85
Lu (ppm)	0.15	0.31	0.21	0.26	0.27
Hf (ppm)	0.52	0.86	0.69	0.65	0.63
Ta (ppm)	0.56	0.27	0.34	0.22	0.40
Pb (ppm)	20.42	20.49	12.52	7.21	15.51
Th (ppm)	1.40	1.17	0.35	2.74	2.59
U (ppm)	1.16	0.89	0.16	0.76	0.76
K (ppm)	5472	8704	4464	7729	12661
Na (ppm)	20180	16956	14475	14784	21122

Table 3-2. Major and Trace element analyses of Amphibolites, Farmington Canyon Complex.

Sample#	FCC-74-2	FCC-75-1	FCC-79-1	FCC-81-1	FCC-89-1
Lithology	Amphibolite block	Amphibolite block	Amphibolite block	Amphibolite block	Amphibolite block
SiO2%	52.95	49.70	49.45	50.55	52.34
TiO2%	0.84	1.11	1.00	1.02	0.81
Al2O3%	15.23	15.81	13.62	18.57	13.07
FeO*%	10.59	12.57	12.86	11.20	11.55
MnO%	0.15	0.24	0.16	0.17	0.19
MgO%	6.53	6.99	9.11	6.60	9.83
CaO%	8.53	9.94	11.03	8.37	10.49
Na2O%	2.98	1.80	2.17	1.06	0.63
K2O%	2.03	1.55	0.38	2.31	0.79
P2O5%	0.13	0.26	0.22	0.13	0.15
MG#	52.22	49.92	55.61	50.74	60.25
Ti (ppm)	5063	6639	6020	6124	4869
Nb_xrf (ppm)	4.3	8.2	4.9	15.8	5.0
Nb (ppm)	3.8	6.9	2.7	16.2	3.4
Zr (ppm)	80	107	68	197	60
Y_xfr (ppm)	21	28	21	36	14
Y (ppm)	12	8	18	1	21
Sr (ppm)	182	191	255	35	69
Rb (ppm)	98	82	10	255	54
Rb_I (ppm)	48.5	29.0	7.8	37.7	
Sc_xrf (ppm)	27.1	31.8	32.9	7.7	30.2
Sc (ppm)	24.3	13.2	36.6	6.7	14.8
V_xrf (ppm)	240	273	286	225	233
V (ppm)	230	250	266	172	
Cr (ppm)	16	174	137	254	1100
Cr_I (ppm)	7	8	41	170	
Ni (ppm)	55	63	112	98	264
Co (ppm)	39.9	53.9	55.4	42.8	
Cu (ppm)	41	9	126	49	12
Zn (ppm)	139	92	103	144	93
Ba_xrf (ppm)	606	314	126	840	65
Ba (ppm)	545	191	121	73	52
La (ppm)	8.76	6.64	6.73	2.47	7.38
Ce (ppm)	18.37	14.75	15.22	2.80	14.98
Pr (ppm)	2.31	1.73	2.07	0.61	1.86
Nd (ppm)	9.57	7.04	9.25	2.21	7.12
Eu (ppm)	0.75	0.48	0.89	0.09	0.65
Sm (ppm)	2.38	1.60	2.51	0.41	1.72
Gd (ppm)	2.52	1.63	3.03	0.34	1.97
Tb (ppm)	0.42	0.27	0.54	0.04	0.34
Dy (ppm)	2.66	1.76	3.58	0.22	2.16
Ho (ppm)	0.57	0.37	0.77	0.05	0.49
Er (ppm)	1.63	1.08	2.25	0.11	1.47
Tm (ppm)	0.23	0.16	0.33	0.02	0.23
Yb (ppm)	1.49	1.03	2.11	0.11	1.57
Lu (ppm)	0.22	0.15	0.32	0.02	0.26
Hf (ppm)	0.60	0.62	0.89	0.15	0.47
Ta (ppm)	0.33	0.57	0.23	1.81	0.25
Pb (ppm)	11.95	8.14	12.82	12.97	5.36
Th (ppm)	1.56	0.69	0.42	0.87	1.25
U (ppm)	0.59	1.59	0.14	2.55	0.39
K (ppm)	16884	12857	3132	19190	6581
Na (ppm)	22071	13368	16118	7850	4686

Table 3-2. Major and Trace element analyses of Amphibolites, Farmington Canyon Complex.

Sample#	FCC-101-1	FCC-107-1	FCC-109-1	FCC-123-2	FCC-124-1
Lithology	Amphibolite block	Amphibolite block	Amphibolite block	Amphibolite block	Amphibolite block
SiO2%	48.83	50.09	51.89	52.63	50.61
TiO2%	1.72	0.96	1.03	1.06	0.46
Al2O3%	13.47	14.92	12.01	13.26	16.47
FeO*%	13.59	12.11	11.72	11.98	8.35
MnO%	0.20	0.22	0.20	0.12	0.12
MgO%	9.41	7.57	9.91	7.92	9.48
CaO%	9.73	11.92	10.72	11.27	12.06
Na2O%	2.07	0.83	0.73	0.13	1.81
K2O%	0.67	1.11	1.50	1.36	0.40
P2O5%	0.23	0.21	0.19	0.19	0.19
MG#	54.66	51.97	59.54	54.47	67.26
Ti (ppm)	10295	5775	6196	6330	2764
Nb_xrf (ppm)	5.1	3.3	3.6	3.0	2.3
Nb (ppm)	3.3	2.3	2.3	2.8	1.3
Zr (ppm)	72	55	59	59	36
Y_xfr (ppm)	18	19	16	17	12
Y (ppm)	14	6	16	18	3
Sr (ppm)	147	120	122	182	152
Rb (ppm)	79	72	82	96	7
Rb_I (ppm)	44.6	20.0	78.6	94.4	3.2
Sc_xrf (ppm)	30.4	33.2	31.4	34.0	30.8
Sc (ppm)	29.3	17.6	36.5	41.7	11.9
V_xrf (ppm)	280	302	285	307	206
V (ppm)	255	259	277	312	159
Cr (ppm)	397	414	745	411	353
Cr_I (ppm)	332	37	1194	519	244
Ni (ppm)	92	74	182	89	140
Co (ppm)	41.5	44.6	53.2	70.6	34.5
Cu (ppm)	116	47	107	8	57
Zn (ppm)	95	95	94	99	38
Ba_xrf (ppm)	258	125	139	292	73
Ba (ppm)	229	71	135	311	32
La (ppm)	8.65	3.51	4.56	3.25	1.61
Ce (ppm)	19.37	6.26	11.65	9.34	4.16
Pr (ppm)	2.49	1.05	1.75	1.58	0.47
Nd (ppm)	10.68	4.29	8.42	8.52	2.01
Eu (ppm)	0.96	0.34	0.96	0.94	0.19
Sm (ppm)	2.59	1.09	2.58	2.99	0.54
Gd (ppm)	2.88	1.15	3.25	3.68	0.66
Tb (ppm)	0.45	0.21	0.56	0.61	0.11
Dy (ppm)	2.83	1.24	3.52	3.68	0.72
Ho (ppm)	0.60	0.27	0.70	0.74	0.16
Er (ppm)	1.72	0.75	1.92	2.01	0.45
Tm (ppm)	0.25	0.11	0.25	0.27	0.06
Yb (ppm)	1.59	0.67	1.58	1.63	0.41
Lu (ppm)	0.25	0.10	0.23	0.24	0.06
Hf (ppm)	0.72	0.45	0.82	0.26	0.44
Ta (ppm)	0.30	0.21	0.19	0.20	0.13
Pb (ppm)	15.67	20.36	10.96	3.75	4.07
Th (ppm)	0.83	0.32	0.50	0.18	0.25
U (ppm)	0.83	0.69	0.14	0.23	0.24
K (ppm)	5536	9217	12442	11250	3360
Na (ppm)	15337	6191	5440	991	13449

Table 3-2. Major and Trace element analyses of Amphibolites, Farmington Canyon Complex.

Sample#	FCC-124-2	FCC-129-1	FCC-163-1	FCC-175-3A	FCC-177-1
Lithology	Amphibolite block	Amphibolite block	Amphibolite block	Amphibolite block	Amphibolite block
SiO2%	45.82	49.54	52.51	52.10	52.69
TiO2%	1.45	0.78	0.96	1.07	1.27
Al2O3%	12.38	14.72	14.84	16.47	13.02
FeO*%	15.32	11.27	12.29	10.44	11.48
MnO%	0.19	0.17	0.16	0.16	0.17
MgO%	11.09	11.54	6.47	8.03	7.34
CaO%	10.87	9.03	9.48	8.55	10.64
Na2O%	1.98	0.82	2.15	0.93	2.18
K2O%	0.52	1.70	0.90	2.09	0.95
P2O5%	0.25	0.23	0.20	0.10	0.26
MG#	56.05	64.79	47.69	57.98	53.27
Ti (ppm)	8712	4658	5763	6414	7610
Nb_xrf (ppm)	7.5	3.3	4.9	5.0	8.8
Nb (ppm)		2.9	3.9	4.9	8.0
Zr (ppm)	88	64	76	78	107
Y_xfr (ppm)	25	16	19	24	37
Y (ppm)		10	16	6	31
Sr (ppm)	70	73	174	66	172
Rb (ppm)	12	136	65	128	52
Rb_I (ppm)		54.4	45.7	40.4	43.8
Sc_xrf (ppm)	24.4	30.2	27.7	26.0	34.9
Sc (ppm)		28.2	32.4	9.4	36.8
V_xrf (ppm)	255	226	287	238	419
V (ppm)		200	260	213	367
Cr (ppm)	747	1227	278	422	106
Cr_I (ppm)		2192	69	205	31
Ni (ppm)	210	289	89	82	65
Co (ppm)		57.1	49.3	34.1	39.2
Cu (ppm)	7	43	129	55	6
Zn (ppm)	77	103	70	62	73
Ba_xrf (ppm)	38	145	117	208	163
Ba (ppm)		103	130	109	160
La (ppm)		6.66	8.38	5.04	15.48
Ce (ppm)		14.48	18.72	11.53	33.60
Pr (ppm)		1.84	2.55	1.58	4.41
Nd (ppm)		7.71	10.93	6.23	18.56
Eu (ppm)		0.67	1.00	0.40	1.22
Sm (ppm)		1.77	2.89	1.52	4.60
Gd (ppm)		1.92	3.32	1.54	5.26
Tb (ppm)		0.32	0.56	0.24	0.91
Dy (ppm)		2.06	3.31	1.48	5.96
Ho (ppm)		0.44	0.71	0.30	1.27
Er (ppm)		1.35	1.93	0.84	3.77
Tm (ppm)		0.20	0.30	0.12	0.56
Yb (ppm)		1.37	1.71	0.76	3.53
Lu (ppm)		0.21	0.28	0.11	0.53
Hf (ppm)		0.57	1.19	0.40	0.99
Ta (ppm)		0.21	0.92	0.48	0.88
Pb (ppm)		9.06	7.09	5.85	6.97
Th (ppm)		0.97	1.90	0.75	3.76
U (ppm)		0.29	0.57	0.63	1.48
K (ppm)	4305	14092	7506	17348	7869
Na (ppm)	14669	6087	15967	6925	16143

Table 3-2. Major and Trace element analyses of Amphibolites, Farmington Canyon Complex.

Sample#	FCC-5-2	FCC-16-1	FCC-32-1	FCC-33-2	FCC-36-2
Lithology	Amphibolite dike	Amphibolite dike	Amphibolite dike	Amphibolite dike	Amphibolite dike
SiO2%	48.60	49.54	50.87	52.13	49.74
TiO2%	2.42	3.36	0.90	1.15	1.91
Al2O3%	12.89	12.16	14.85	14.94	16.22
FeO*%	17.91	14.10	11.52	13.75	19.20
MnO%	0.26	0.24	0.20	0.18	0.21
MgO%	4.44	9.92	7.83	5.68	4.04
CaO%	8.72	7.50	10.88	9.37	6.34
Na2O%	3.07	2.12	1.30	0.96	0.41
K2O%	1.19	0.49	1.51	1.52	1.70
P2O5%	0.45	0.49	0.13	0.28	0.21
MG#	30.36	54.95	54.57	41.91	27.12
Ti (ppm)	14491	20142	5421	6904	11449
Nb_xrf (ppm)	10.9	24.2	3.9	5.7	7.1
Nb (ppm)	10.4	13.9	2.3		8.2
Zr (ppm)	171	250	54	103	118
Y_xfr (ppm)	51	40	17	29	31
Y (ppm)	45	12	13		25
Sr (ppm)	140	93	171	186	118
Rb (ppm)	35	21	77	112	128
Rb_I (ppm)	29.4	8.4	42.8		97.8
Sc_xrf (ppm)	28.4	22.2	34.6	30.4	17.0
Sc (ppm)	33.0	1.8	34.5		20.4
V_xrf (ppm)	401	318	308	314	244
V (ppm)	379	247	261		231
Cr (ppm)	52	650	236	119	39
Cr_I (ppm)	22	738	55		11
Ni (ppm)	33	377	61	55	49
Co (ppm)	44.7	78.6	44.2		51.1
Cu (ppm)	126	110	52	6	40
Zn (ppm)	164	71	89	104	83
Ba_xrf (ppm)	242	93	238	197	358
Ba (ppm)	264	129	239		316
La (ppm)	20.83	20.53	5.54		20.75
Ce (ppm)	46.46	48.18	12.36		40.69
Pr (ppm)	6.28	5.92	1.64		5.26
Nd (ppm)	27.09	23.69	7.18		20.35
Eu (ppm)	2.20	1.29	0.75		1.47
Sm (ppm)	6.78	4.86	1.97		4.44
Gd (ppm)	8.05	4.27	2.36		4.64
Tb (ppm)	1.39	0.63	0.40		0.71
Dy (ppm)	8.87	3.34	2.67		4.53
Ho (ppm)	1.91	0.60	0.57		0.94
Er (ppm)	5.60	1.52	1.66		2.73
Tm (ppm)	0.81	0.20	0.24		0.40
Yb (ppm)	5.26	1.14	1.56		2.57
Lu (ppm)	0.81	0.15	0.24		0.40
Hf (ppm)	1.75	0.52	0.85		0.59
Ta (ppm)	0.80	1.27	0.23		0.83
Pb (ppm)	15.05	9.73	10.85		10.97
Th (ppm)	2.36	1.50	0.92		7.10
U (ppm)	1.37	1.07	0.47		1.90
K (ppm)	9880	4104	12495	12615	14149
Na (ppm)	22777	15745	9635	7105	3030

Table 3-2. Major and Trace element analyses of Amphibolites, Farmington Canyon Complex.

Sample#	FCC-45-1	FCC-46-4	FCC-53-1	FCC-61-6	FCC-82-1
Lithology	Amphibolite dike	Amphibolite dike	Amphibolite dike	Amphibolite dike	Amphibolite dike
SiO2%	47.71	48.37	45.27	50.26	51.44
TiO2%	1.99	2.21	2.51	1.88	2.28
Al2O3%	12.23	13.26	17.54	15.20	15.12
FeO*%	19.61	15.84	17.35	17.59	14.44
MnO%	0.27	0.20	0.39	0.26	0.23
MgO%	4.91	6.20	3.94	4.66	4.00
CaO%	9.36	9.63	9.40	8.72	8.54
Na2O%	2.42	2.97	1.71	0.71	2.54
K2O%	1.24	0.98	1.50	0.47	0.76
P2O5%	0.23	0.27	0.36	0.23	0.62
MG#	30.77	40.85	28.52	32.36	33.20
Ti (ppm)	11933	13243	15074	11286	13646
Nb_xrf (ppm)	20.0	8.3	12.5	11.1	20.6
Nb (ppm)	21.4	7.4	11.9	11.3	19.1
Zr (ppm)	163	110	184	144	367
Y_xfr (ppm)	72	33	44	59	63
Y (ppm)	65	30	41	50	22
Sr (ppm)	63	105	156	66	244
Rb (ppm)	35	38	86	15	23
Rb_I (ppm)	29.9	34.9	76.7	13.5	9.6
Sc_xrf (ppm)	28.5	30.3	30.2	28.5	25.5
Sc (ppm)	42.9	32.3	38.5	39.2	9.4
V_xrf (ppm)	587	340	411	464	324
V (ppm)	1075	308	355	846	274
Cr (ppm)	87	120	129	482	98
Cr_I (ppm)	5	108	35	12	55
Ni (ppm)	44	105	61	46	56
Co (ppm)	60.1	50.5	57.2	43.0	34.4
Cu (ppm)	156	213	193	33	5
Zn (ppm)	163	134	139	164	131
Ba_xrf (ppm)	119	138	244	236	534
Ba (ppm)	140	128	227	193	477
La (ppm)	32.64	10.29	34.06	18.61	45.83
Ce (ppm)	71.31	24.45	67.18	43.09	89.01
Pr (ppm)	9.41	3.43	8.59	5.81	10.95
Nd (ppm)	38.58	15.96	35.01	24.85	40.63
Eu (ppm)	1.97	1.44	2.33	2.03	1.55
Sm (ppm)	9.33	4.42	7.41	6.71	7.01
Gd (ppm)	10.59	5.49	7.78	8.32	6.14
Tb (ppm)	1.87	0.95	1.27	1.54	0.90
Dy (ppm)	12.06	6.11	7.90	9.87	5.25
Ho (ppm)	2.59	1.29	1.71	2.01	1.06
Er (ppm)	7.87	3.75	5.11	5.73	3.01
Tm (ppm)	1.18	0.53	0.76	0.82	0.42
Yb (ppm)	7.68	3.38	5.11	5.12	2.72
Lu (ppm)	1.16	0.52	0.82	0.76	0.40
Hf (ppm)	2.02	1.49	0.64	0.95	0.70
Ta (ppm)	2.06	0.57	1.04	1.22	1.29
Pb (ppm)	12.01	7.28	10.07	13.15	20.52
Th (ppm)	2.53	1.66	3.61	5.95	3.33
U (ppm)	1.03	0.34	0.75	1.71	1.08
K (ppm)	10286	8131	12491	3867	6297
Na (ppm)	17987	22041	12704	5288	18829

Table 3-2. Major and Trace element analyses of Amphibolites, Farmington Canyon Complex.

Sample#	FCC-114-1	FCC-130-1	FCC-131-1	FCC-143-1	FCC-149-1
Lithology	Amphibolite dike	Amphibolite dike	Amphibolite dike	Amphibolite dike	Amphibolite dike
SiO2%	51.39	48.46	49.32	45.63	48.41
TiO2%	1.84	2.13	0.62	2.73	1.61
Al2O3%	13.66	15.17	13.73	12.81	15.81
FeO*%	16.84	17.69	14.00	17.63	13.17
MnO%	0.29	0.25	0.23	0.45	0.20
MgO%	3.79	4.42	8.00	6.62	6.76
CaO%	6.83	9.67	10.36	10.27	10.35
Na2O%	2.13	0.89	1.96	1.45	1.22
K2O%	2.64	1.03	1.58	1.74	2.08
P2O5%	0.52	0.29	0.17	0.66	0.35
MG#	28.65	30.77	50.55	39.65	47.54
Ti (ppm)	11030	12758	3743	16362	9668
Nb_xrf (ppm)	20.8	18.5	7.8	9.7	5.0
Nb (ppm)	19.9	20.5	6.6	8.8	
Zr (ppm)	355	177	78	145	89
Y_xfr (ppm)	75	60	20	37	25
Y (ppm)	68	44	5	34	
Sr (ppm)	68	44	157	69	162
Rb (ppm)	209	38	78	75	149
Rb_I (ppm)	187.7	34.6	30.1	66.4	
Sc_xrf (ppm)	21.2	30.7	29.9	26.7	32.3
Sc (ppm)	26.3	33.5	12.0	36.7	
V_xrf (ppm)	216	480	318	371	294
V (ppm)	182	914	287	369	
Cr (ppm)	444	55	290	246	360
Cr_I (ppm)	93	6	109	154	
Ni (ppm)	56	32	92	131	95
Co (ppm)	31.4	48.3	45.9	57.3	
Cu (ppm)	8	8	15	13	79
Zn (ppm)	323	204	113	751	116
Ba_xrf (ppm)	336	219	305	393	284
Ba (ppm)	364	183	168	414	
La (ppm)	52.46	17.99	3.97	21.21	
Ce (ppm)	106.04	43.24	10.27	46.99	
Pr (ppm)	14.08	6.21	1.18	6.32	
Nd (ppm)	57.25	27.22	5.13	27.41	
Eu (ppm)	3.79	2.31	0.39	2.25	
Sm (ppm)	12.02	7.30	1.26	6.47	
Gd (ppm)	12.33	8.27	1.27	6.83	
Tb (ppm)	2.07	1.46	0.22	1.09	
Dy (ppm)	12.87	9.23	1.29	6.58	
Ho (ppm)	2.70	1.87	0.27	1.38	
Er (ppm)	8.12	5.30	0.75	3.98	
Tm (ppm)	1.25	0.75	0.10	0.56	
Yb (ppm)	8.53	4.61	0.66	3.66	
Lu (ppm)	1.36	0.67	0.09	0.56	
Hf (ppm)	1.08	1.27	0.70	1.19	
Ta (ppm)	2.18	1.54	0.52	0.55	
Pb (ppm)	15.28	12.10	9.08	19.39	
Th (ppm)	8.49	3.72	0.47	1.99	
U (ppm)	3.22	1.32	0.37	0.68	
K (ppm)	21890	8556	13091	14435	17267
Na (ppm)	15828	6628	14546	10791	9061

Table 3-2. Major and Trace element analyses of Amphibolites, Farmington Canyon Complex.

Sample#	FCC-165-2	FCC-171-2	FCC-1-4	FCC-3-1	FCC-4-1
Lithology	Amphibolite dike	Amphibolite dike	High-Al amphibolite	High-Al amphibolite	High-Al amphibolite
SiO2%	51.35	52.49	45.41	51.12	50.17
TiO2%	1.08	1.75	1.18	0.99	0.99
Al2O3%	13.62	14.84	20.26	27.54	20.43
FeO*%	12.60	15.32	16.99	10.41	13.51
MnO%	0.21	0.24	0.20	0.02	0.24
MgO%	7.86	5.89	12.59	2.79	2.93
CaO%	11.00	5.25	0.94	0.45	8.04
Na2O%	1.25	0.23	0.89	0.37	0.92
K2O%	0.81	3.23	1.37	6.23	2.66
P2O5%	0.19	0.52	0.07	0.05	0.11
MG#	52.71	39.78	56.44	31.91	27.61
Ti (ppm)	6448	10498	7072	5959	5911
Nb_xrf (ppm)	6.8	18.0	4.0	9.5	15.0
Nb (ppm)	6.4	17.7		12.5	15.2
Zr (ppm)	78	269	56	183	243
Y_xfr (ppm)	20	67	17	59	53
Y (ppm)	17	62		14	54
Sr (ppm)	120	106	5	47	128
Rb (ppm)	59	185	89	345	133
Rb_I (ppm)	43.7	174.9		150.6	129.2
Sc_xrf (ppm)	31.0	20.5	10.4	10.8	19.1
Sc (ppm)	33.6	32.3		20.2	29.5
V_xrf (ppm)	315	331	292	222	241
V (ppm)	276	257		188	209
Cr (ppm)	315	162	636	208	75
Cr_I (ppm)	235	72		175	1
Ni (ppm)	94	68	223	96	26
Co (ppm)	48.9	69.5		52.5	35.5
Cu (ppm)	35	35	50	44	36
Zn (ppm)	81	141	235	51	160
Ba_xrf (ppm)	109	938	100	610	541
Ba (ppm)	118	905		450	553
La (ppm)	9.70	56.56		15.28	45.35
Ce (ppm)	22.94	101.00		33.01	92.56
Pr (ppm)	3.12	12.91		4.01	11.29
Nd (ppm)	13.37	50.36		15.40	43.93
Eu (ppm)	1.07	1.98		0.71	2.17
Sm (ppm)	3.24	10.28		3.28	9.83
Gd (ppm)	3.50	10.99		2.86	10.28
Tb (ppm)	0.58	1.90		0.44	1.69
Dy (ppm)	3.54	12.04		2.99	10.41
Ho (ppm)	0.73	2.47		0.70	2.16
Er (ppm)	2.06	7.13		2.35	6.39
Tm (ppm)	0.30	1.02		0.36	0.94
Yb (ppm)	1.88	6.64		2.52	5.95
Lu (ppm)	0.28	1.01		0.38	0.89
Hf (ppm)	0.75	0.28		0.31	0.53
Ta (ppm)	0.52	2.09		1.23	1.37
Pb (ppm)	5.08	10.74		11.26	16.22
Th (ppm)	1.64	7.82		11.70	16.72
U (ppm)	0.64	4.18		5.55	2.38
K (ppm)	6709	26773	11382	51696	22076
Na (ppm)	9291	1737	6578	2769	6851

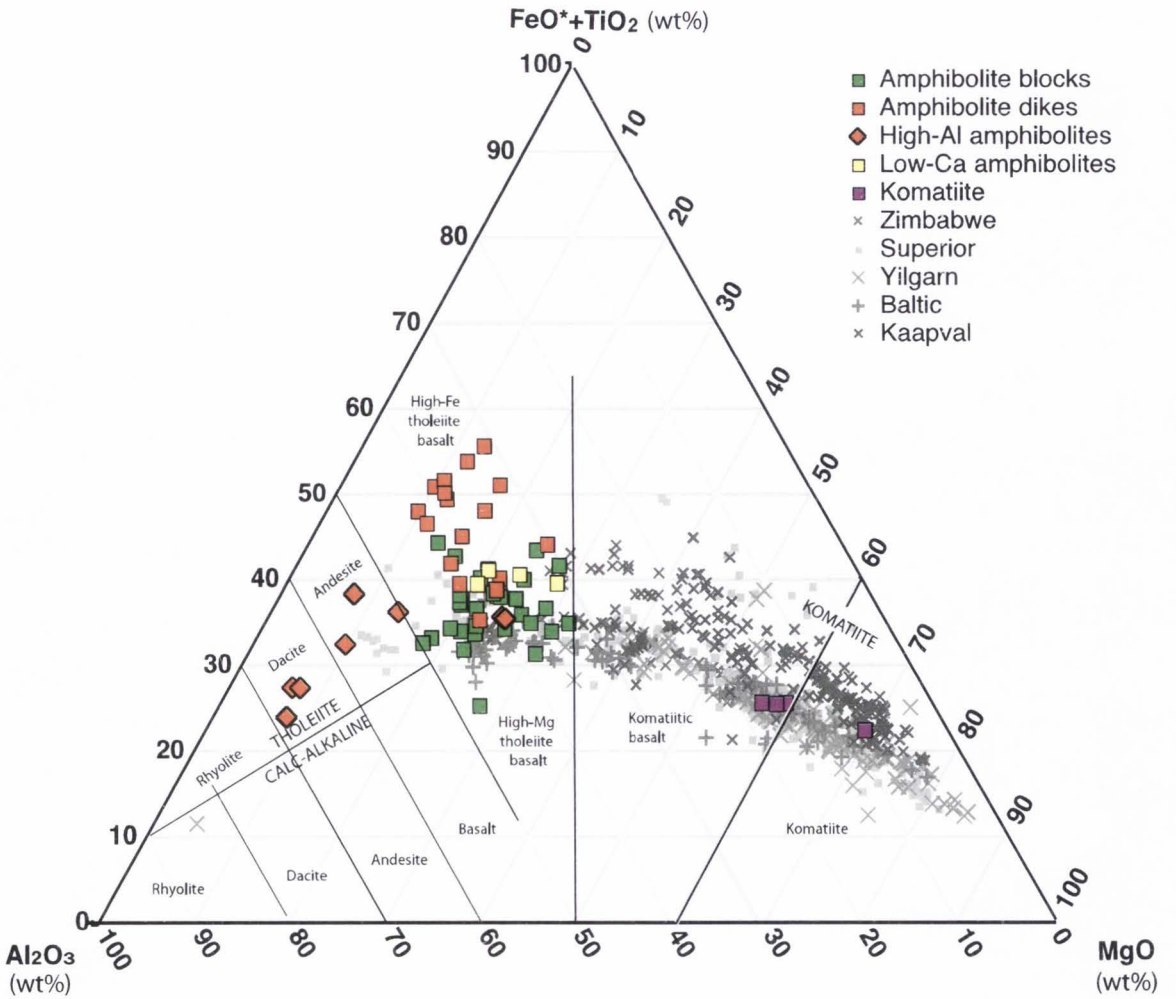

Figure 3-4. Jensen Diagram of amphibolites showing classification fields.

Nickel and Cr are low compared to komatiites and incompatible elements are moderate to high (Figs 3-12 and 3-13). Amphibolite dikes have MgO compositions between 3.8-10% and are higher in titanium and FeO* compared to the amphibolite blocks (Fig 3-6 and 3-7). Both groups are somewhat enriched in K2O, possibly in response to alteration or metamorphism (Fig 3-11).

High-aluminum amphibolites have Al_2O_3 compositions between 19-29%. MgO variation diagrams show that the high-Al amphibolites are low in MgO, CaO, and Na_2O but relatively high in K2O (Fig 3-9 through 3-11); they are also low in FeO* and TiO_2 compared to other amphibolite dikes. The FeO*/(FeO*+MgO)- Al_2O_3 diagram indicates that most of the high-Al amphibolites fall into the normal tholeiitic field (Fig 3-5). The low-calcium amphibolites are characterized by low CaO concentrations (CaO $\approx$ 0.8-1.7%) but otherwise resemble the normal amphibolite blocks and dikes (Fig 3-9). The FeO*/(FeO*+MgO)- Al_2O_3 diagram indicates that the low-Ca amphibolites fall into the normal tholeiitic field (Fig 3-5).

The results of the trace-element chemical analyses of the amphibolites are also shown in Figs 3-12 and 3-13 and Table 3-2. The Cr contents of the amphibolite blocks range from 16-1227 ppm and Ni content range from 26-289 ppm. The amphibolite dikes have Cr amounts between 39-650 ppm and Ni content between 32 and 377 ppm. Amphibolite dikes are also high in high-field-strength elements (HFSE's).

The amphibolite blocks have relatively flat chondrite-normalized REE diagrams that are only slightly enriched in LREE's (Fig 3-14). The amphibolite dikes show a very slight slope to their chondrite-normalized REE concentrations, which is similar to the

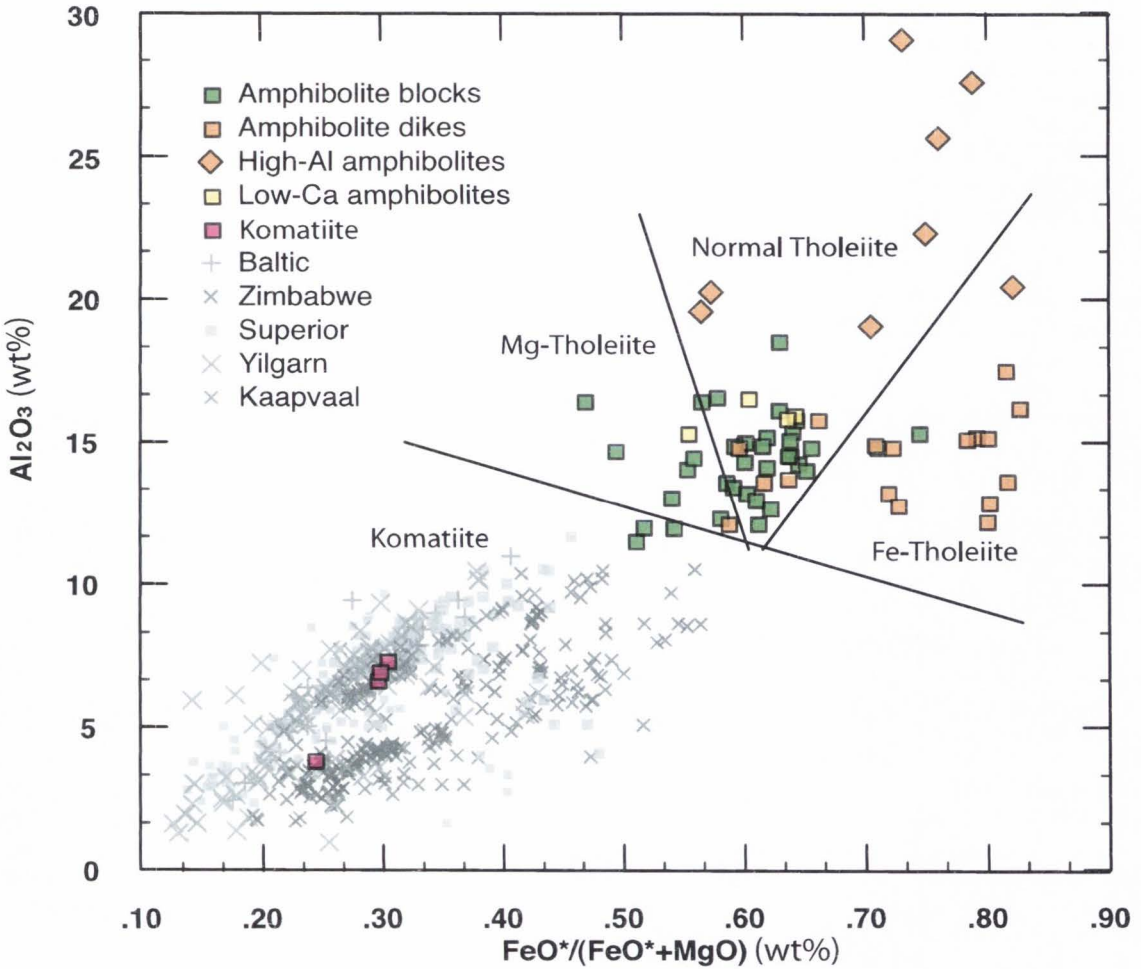

Figure 3-5. Al_2O_3 vs FeO*/(FeO*+MgO) diagram for FCC Amphibolites.

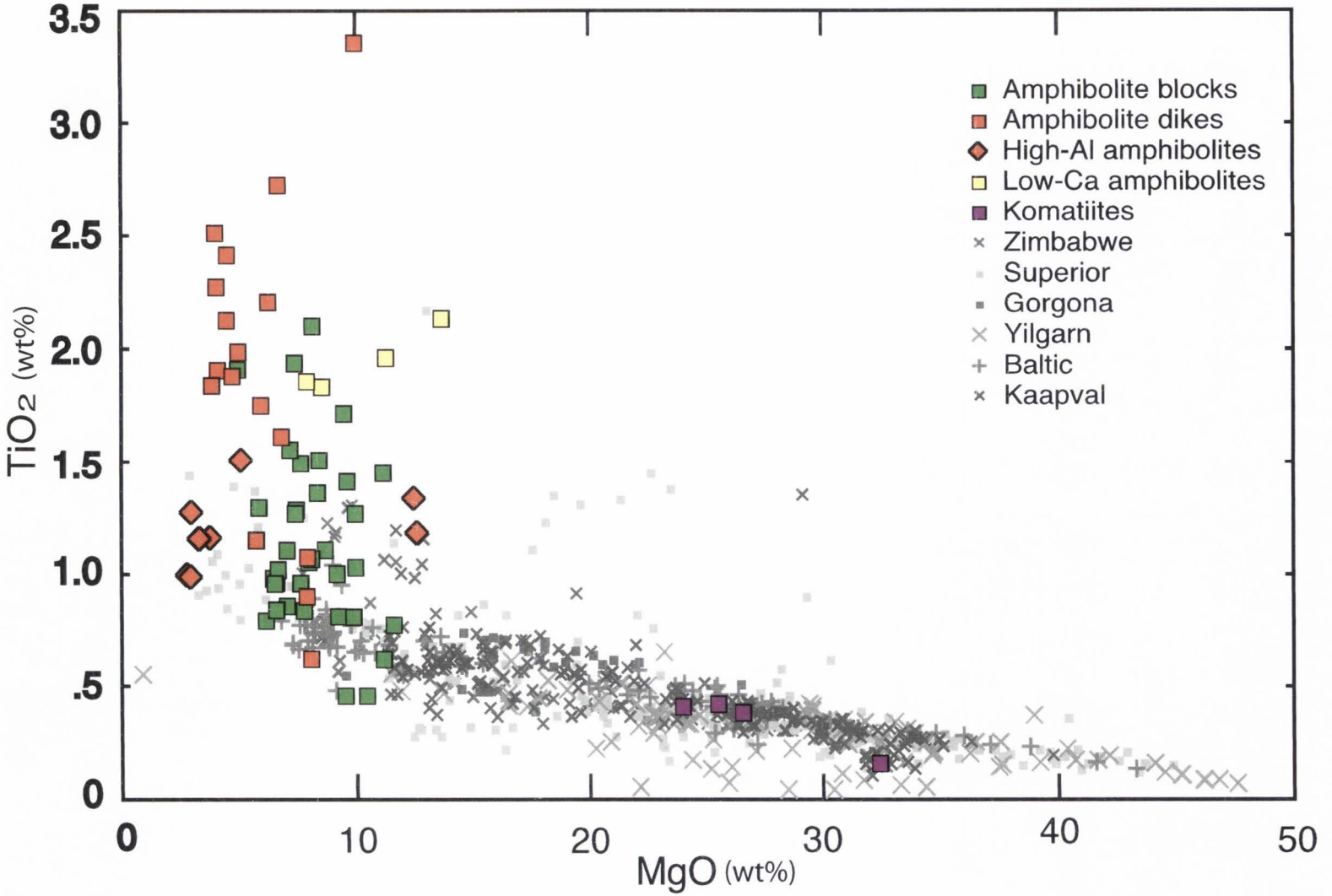

Figure 3-6. TiO_2 vs MgO plot for FCC amphibolites.

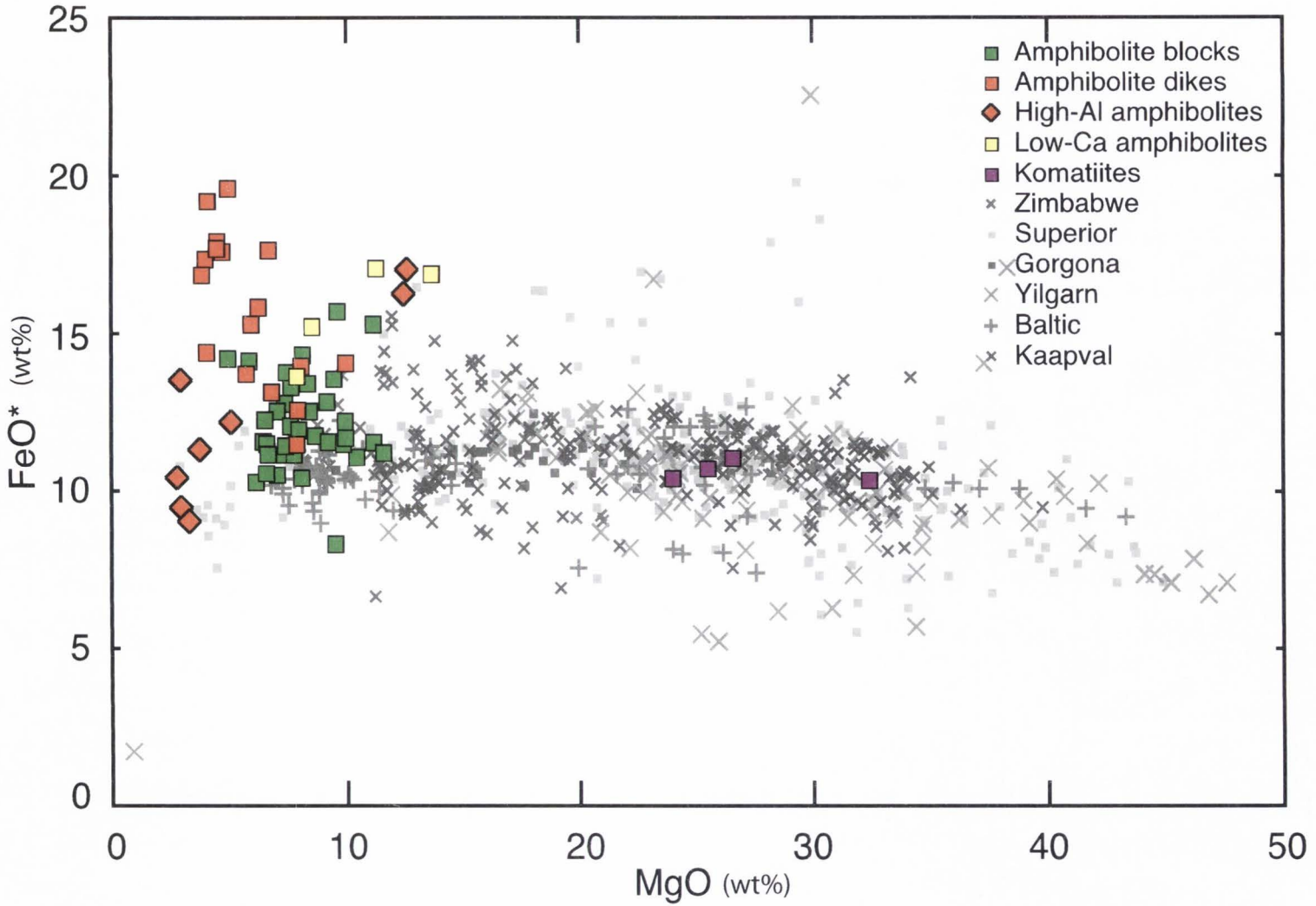

Figure 3-7. FeO* vs MgO plot for FCC amphibolites.

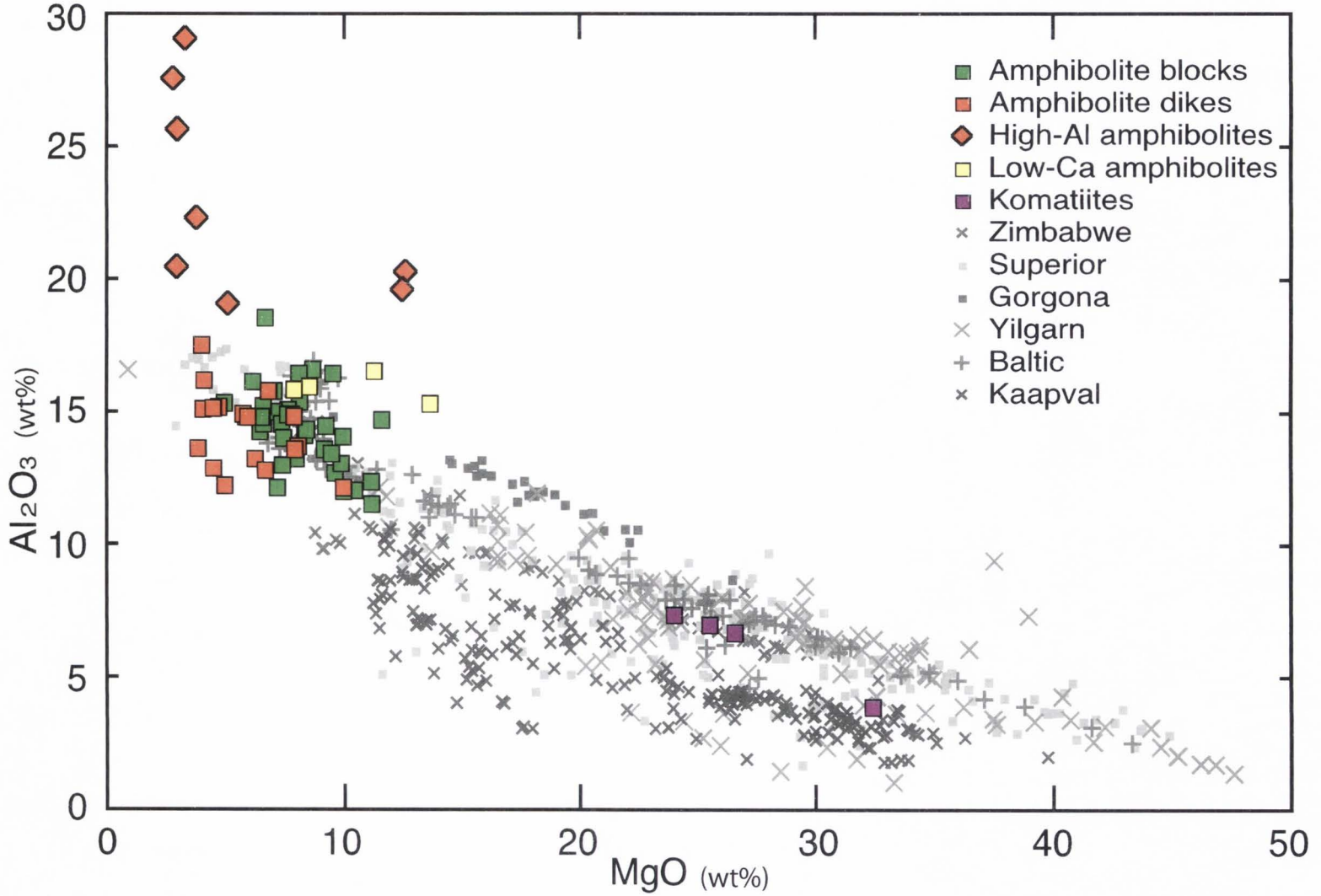

Figure 3-8. Al_2O_3 vs MgO plot for the FCC amphibolites.

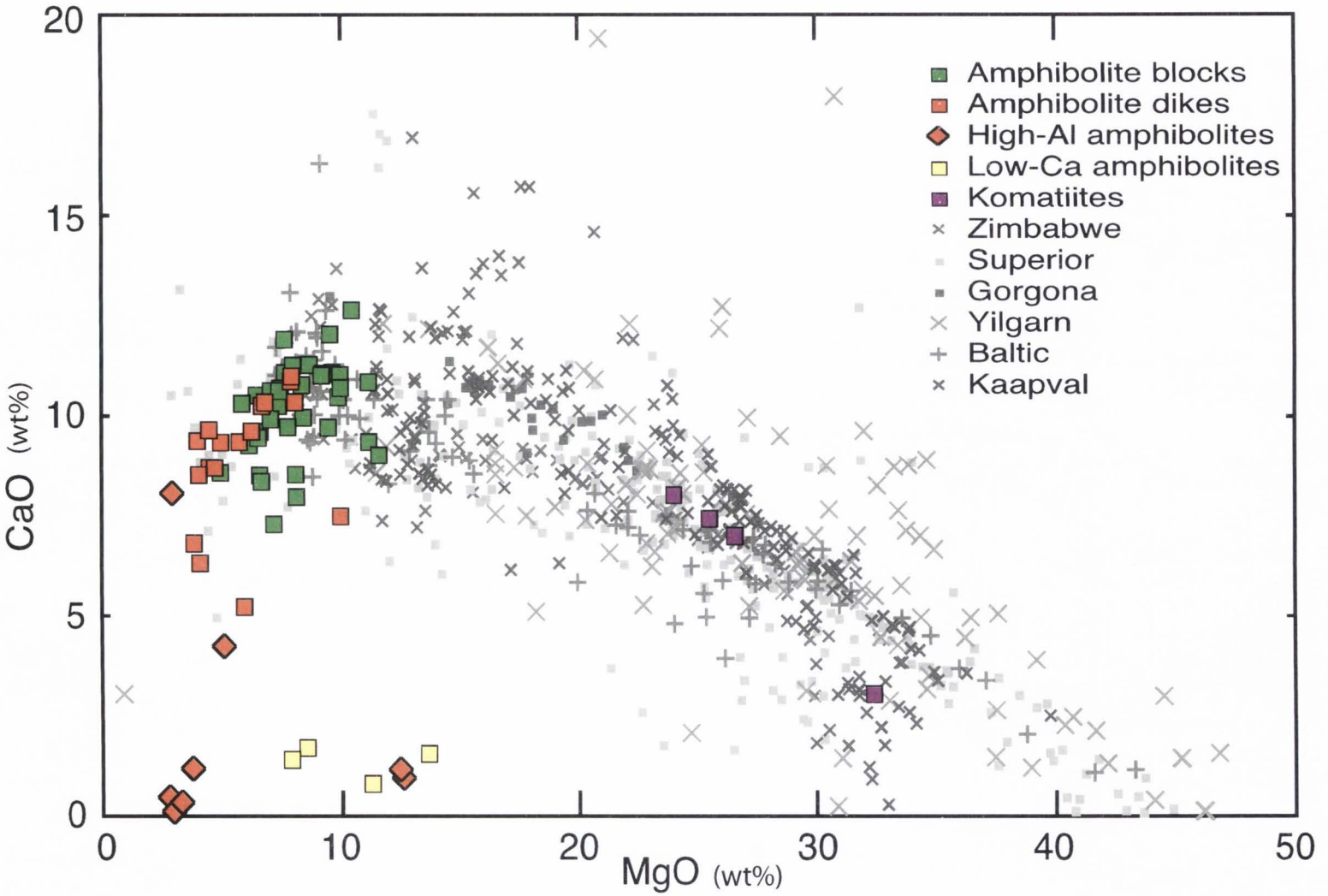

Figure 3-9. CaO vs MgO plot for the FCC amphibolites.

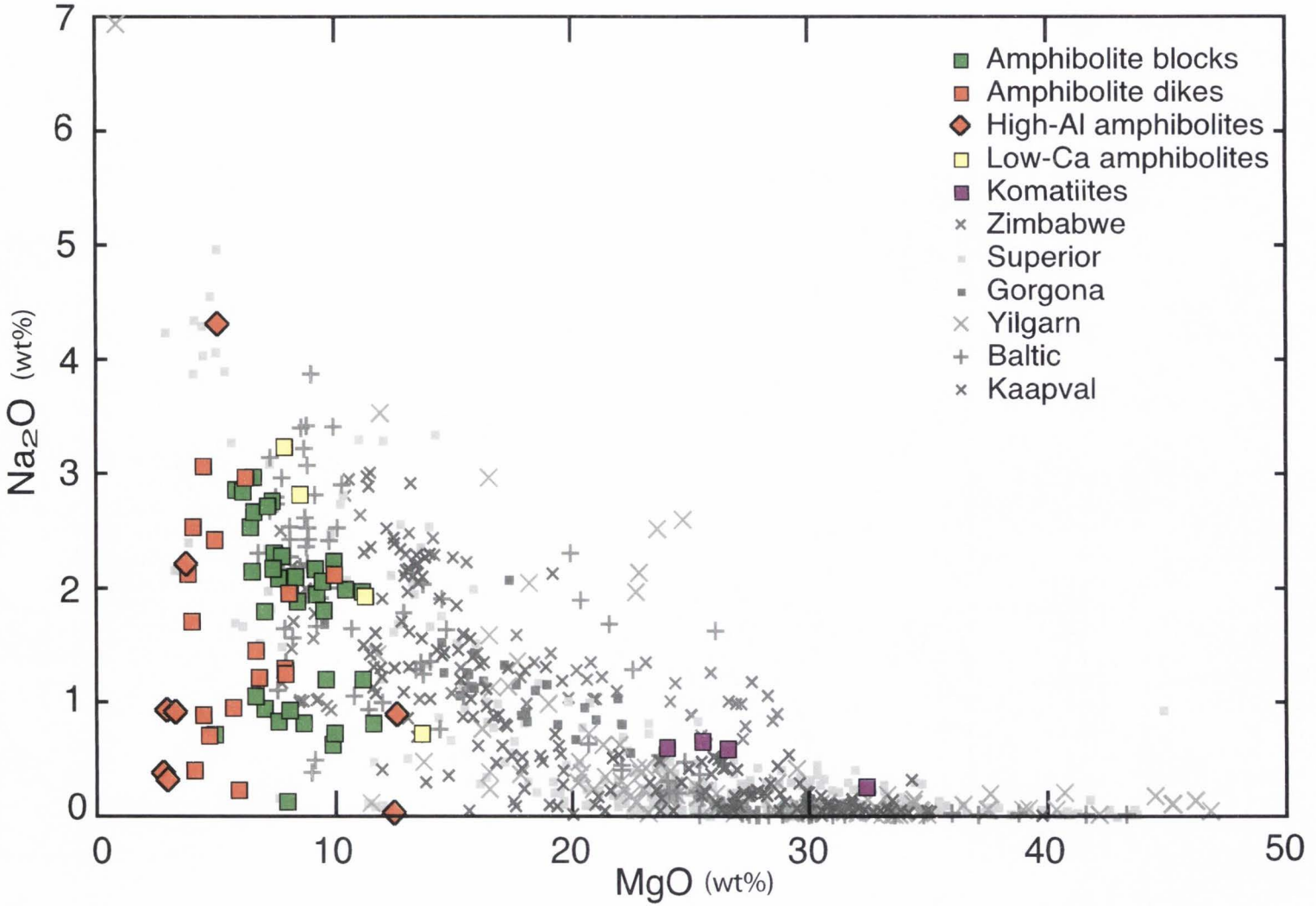

Figure 3-10. A Na_2O vs MgO plot of the FCC amphibolites.

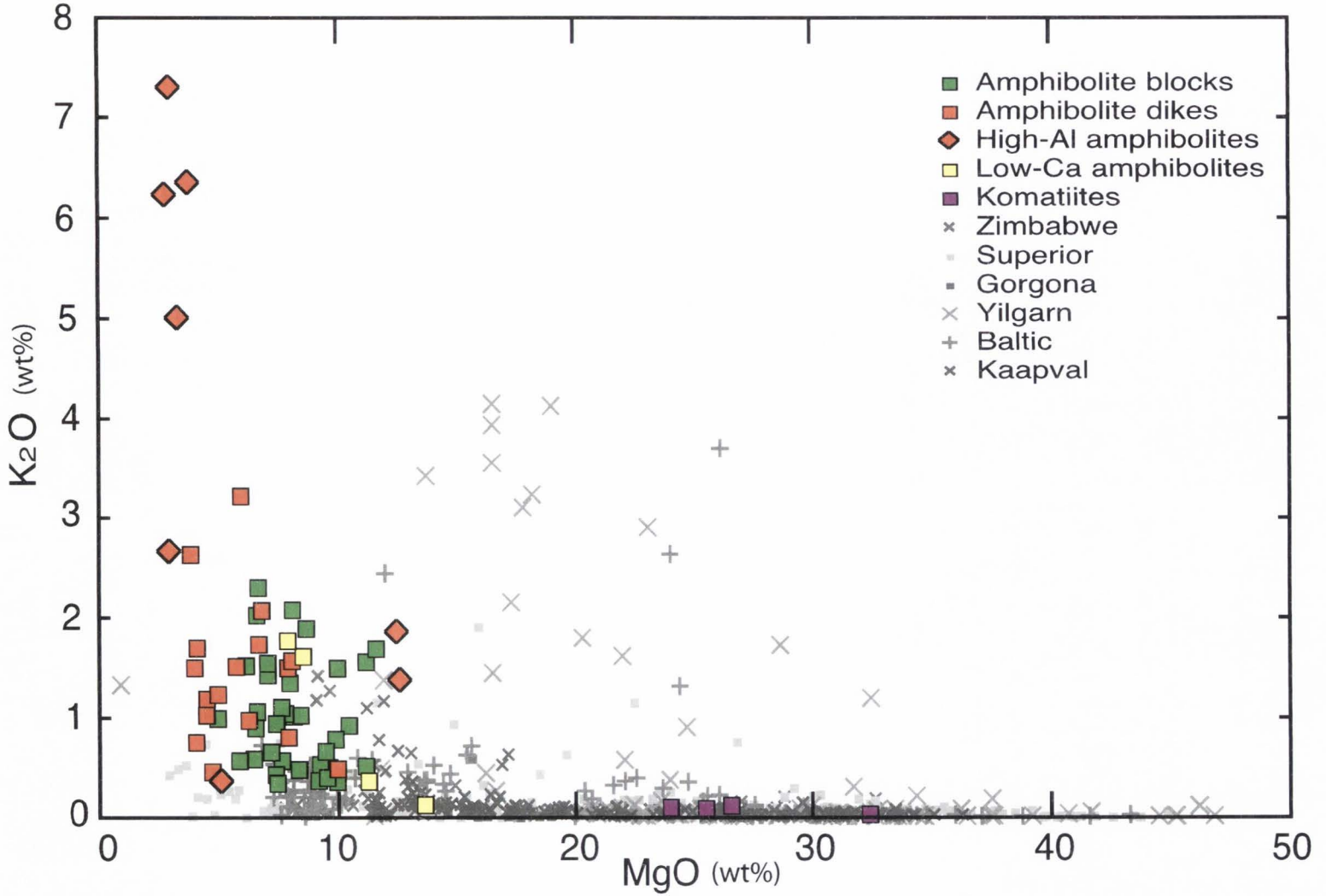

Figure 3-11. K_2O vs MgO plot for the FCC amphibolites.

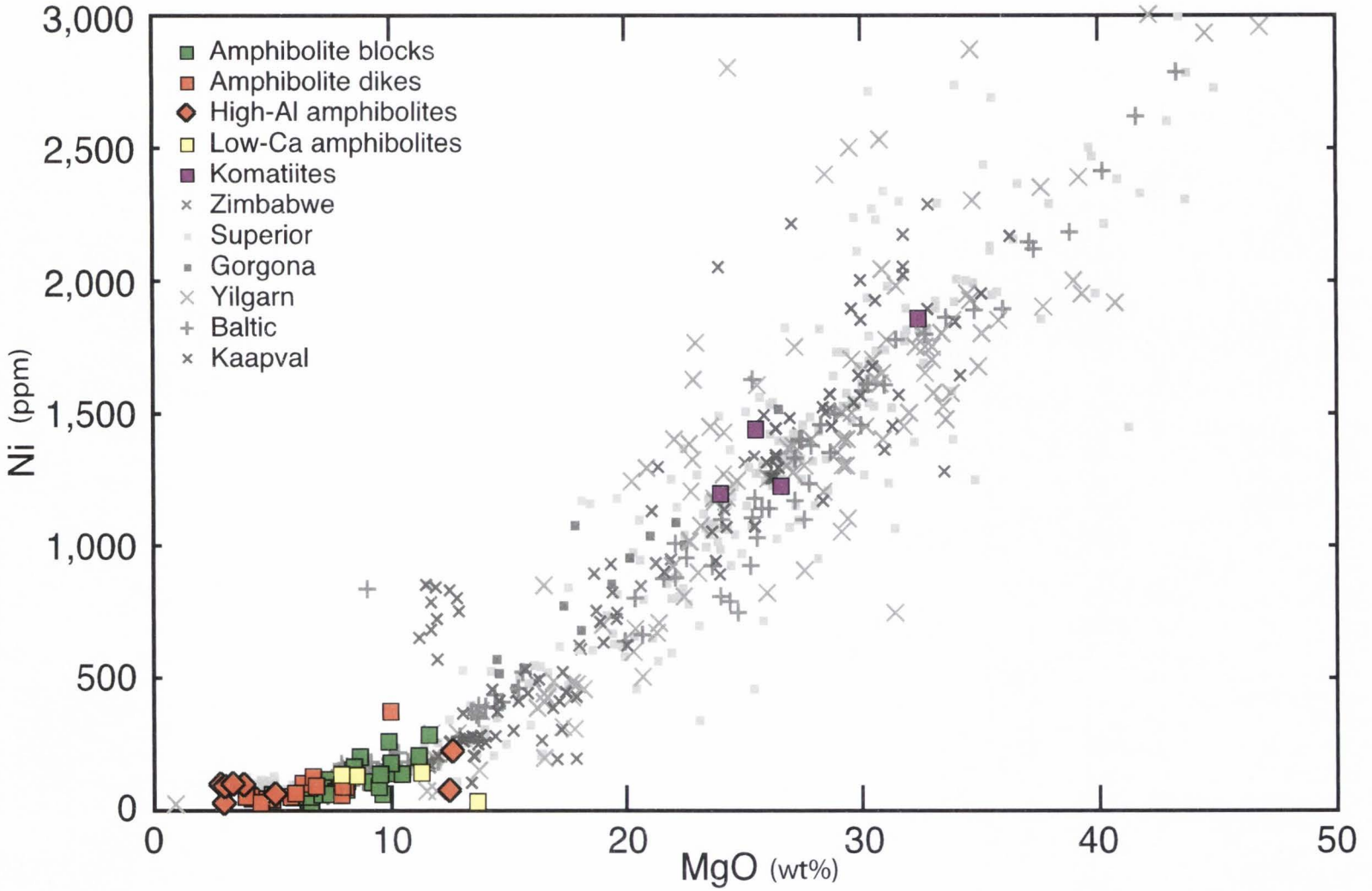

Figure 3-12. Ni vs MgO plot for the FCC amphibolites.

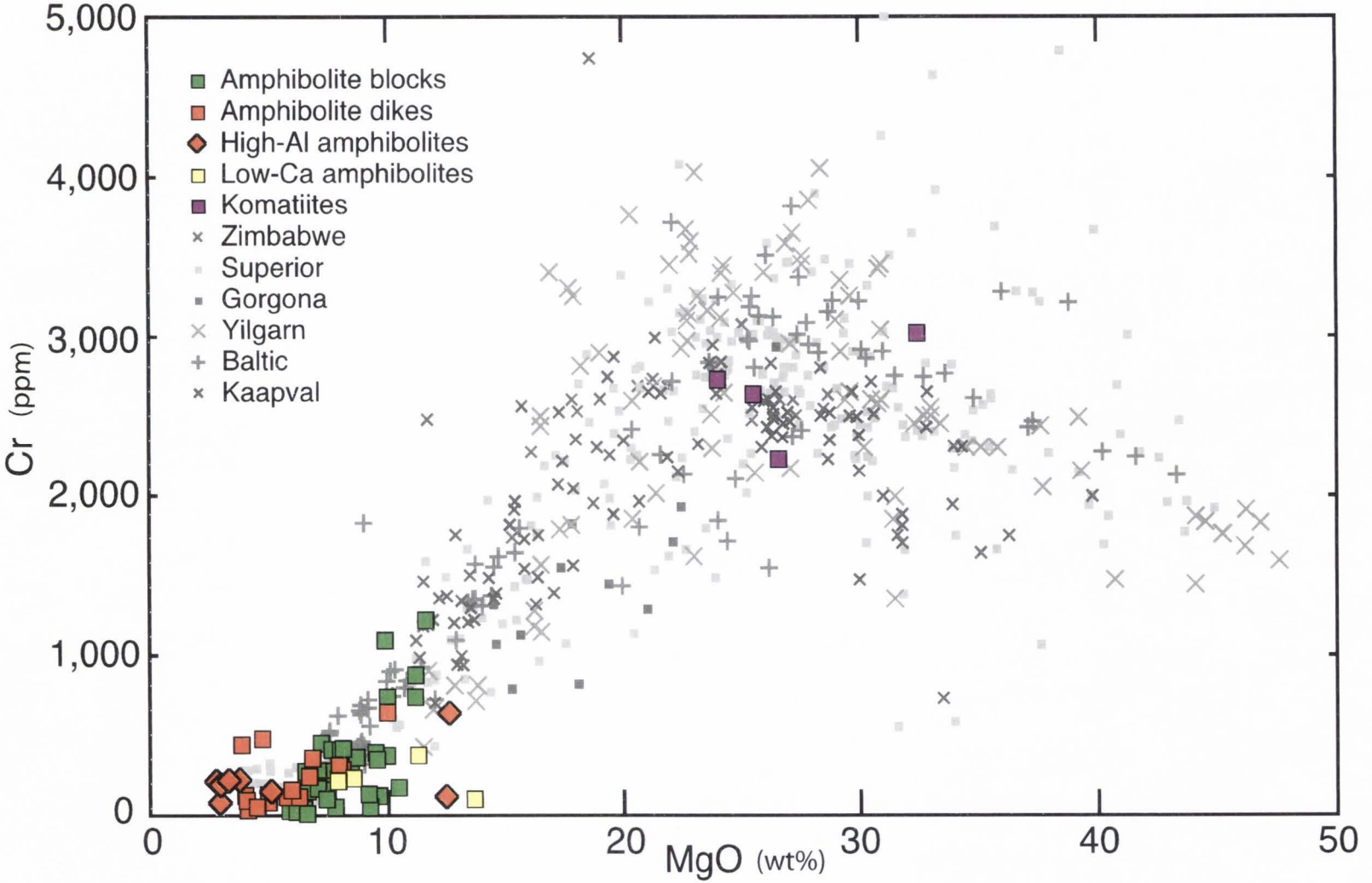

Figure 3-13. Cr vs MgO plot for the FCC amphibolites.

amphibolite blocks, however, the concentrations are slightly higher (Fig 3-15). The high-Al and low-Ca amphibolites have chondrite-normalized REE concentrations similar to the other amphibolites (Fig 3-16).

Multi-element (spider) diagrams for the amphibolites, normalized to primitive mantle, show that all have slight negative slopes, that is, they are progressively enriched in more incompatible elements (Fig 3-17). The amphibolite blocks have relatively flat slopes that are only slightly enriched in the more incompatible elements, with overall concentrations of the moderately incompatible elements of ≈2-10x primitive mantle and a prominent negative Th anomaly (Fig 3-17). The amphibolite dikes have a slightly steeper slope with higher overall concentrations of ≈8-30x primitive mantle for the moderately incompatible elements and prominent negative anomalies for Th, Sr, and Sc (Fig 3-18). The high-Al and low-Ca amphibolites have primitive mantle-normalized concentrations similar to the amphibolite dikes, but with even more prominent negative anomalies for Th, Sr, Sc, and V (Fig 3-19).

Thirteen amphibolite were analyzed for oxygen isotopes. The FCC amphibolites had $\delta^{18}O$ values between 3.4 and 6.4 SMOW. Mantle oxygen values of $\delta^{18}O$ are ~5.6-6.2 SMOW (Table 3-6).

Ultramafics (Komatiites)

Four ultramafic samples were analyzed for major and trace element geochemistry with compositions shown in Table 3-3. The ultramafics have chemical compositions that identify them as komatiites, with SiO_2 ≈ 47-49.5%, FeO* ≈ 10.4-11%, MgO 24-32.4%, Al_2O_3 ≈ 4-7% and TiO_2 is less than 0.4% (Table 3-3). In a Jensen

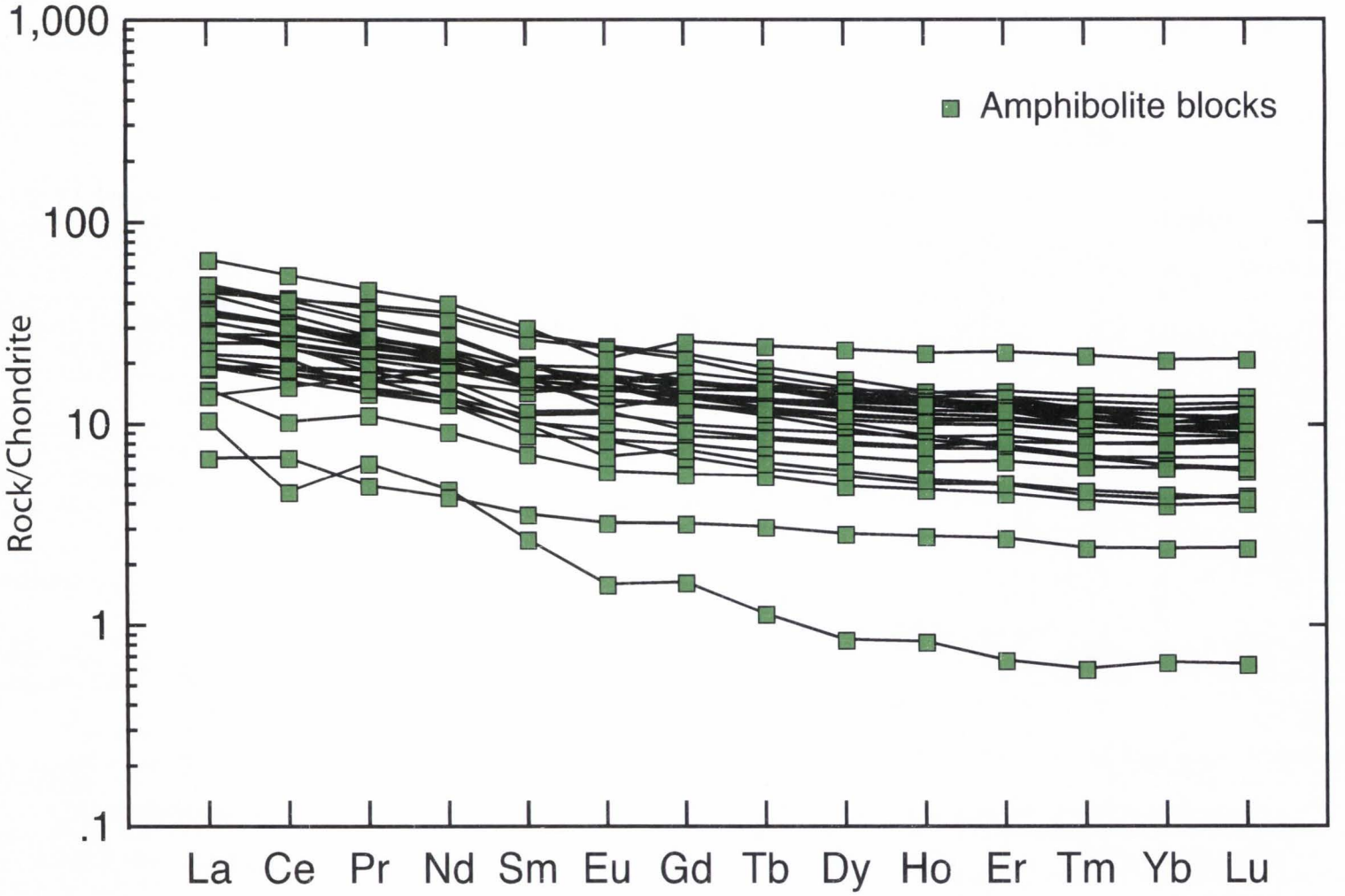

Figure 3-14. A chondrite normalized REE plot for amphibolite blocks.

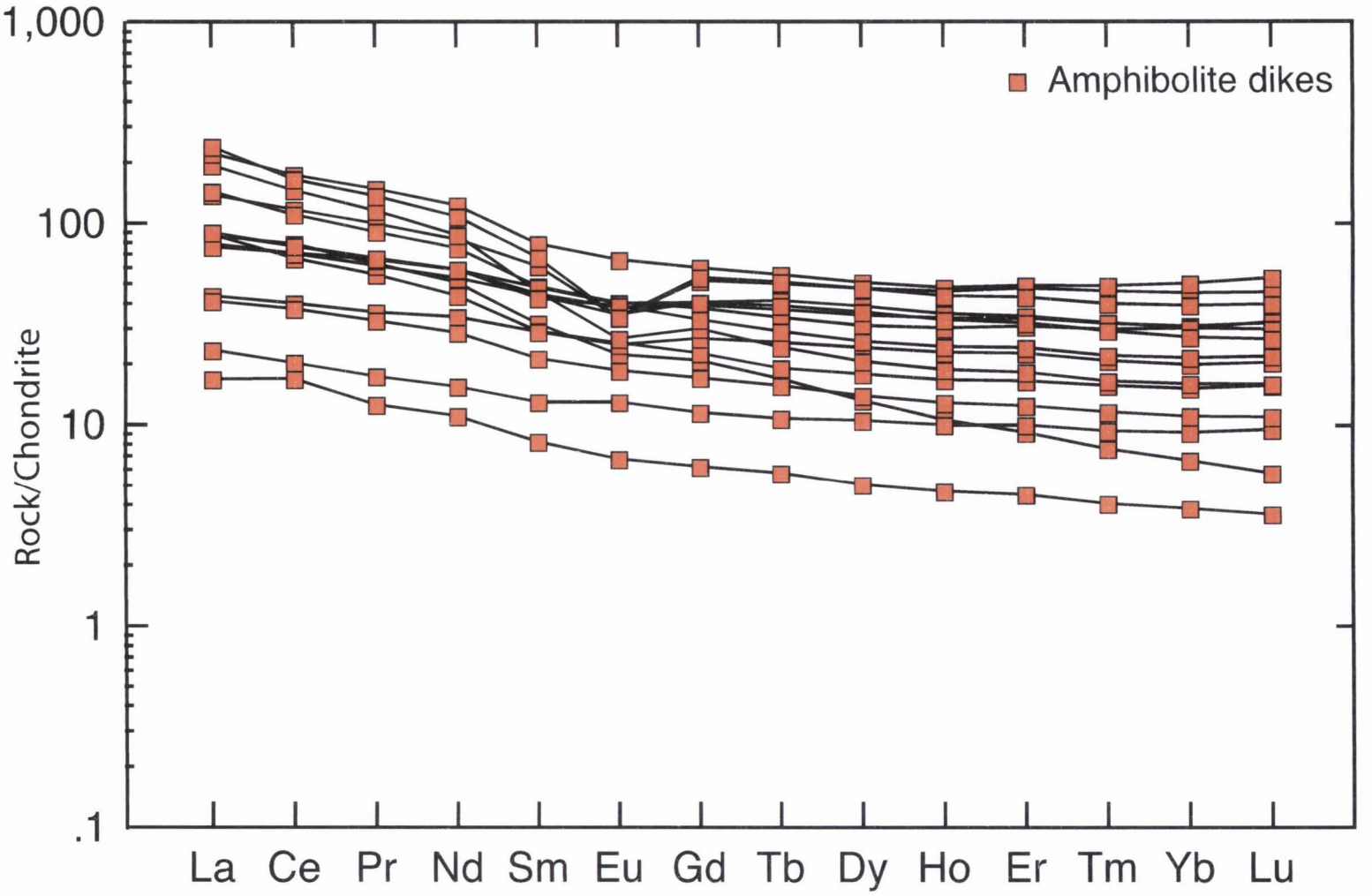

Figure 3-15. A chondrite normalized REE plot of the FCC amphibolite dikes.

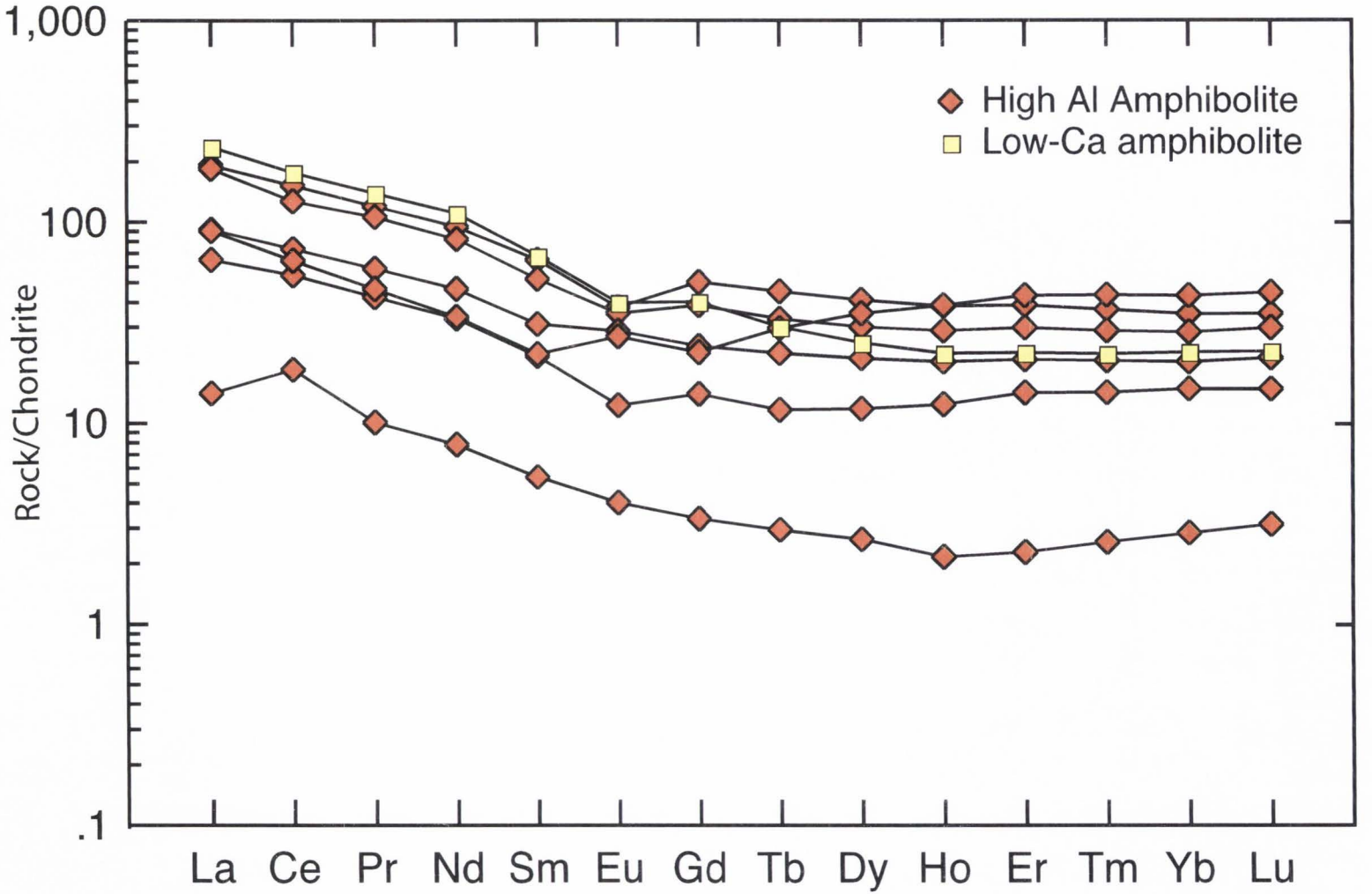

Figure 3-16. A chondrite normalized REE plot for the FCC High-Al/Low-Ca amphibolites.

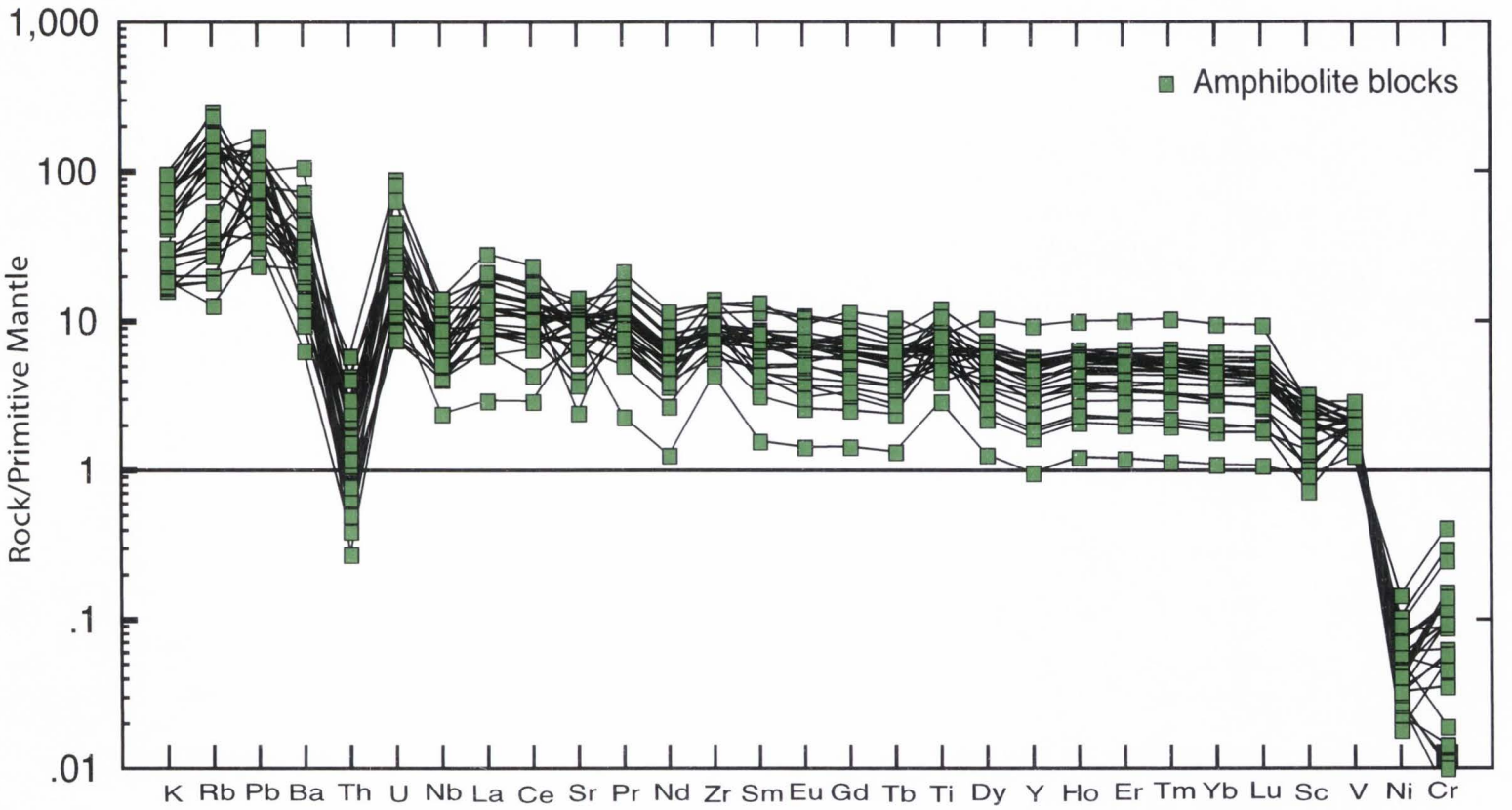

Figure 3-17. Primitive mantle normalized multi-element plots for the FCC amphibolite blocks.

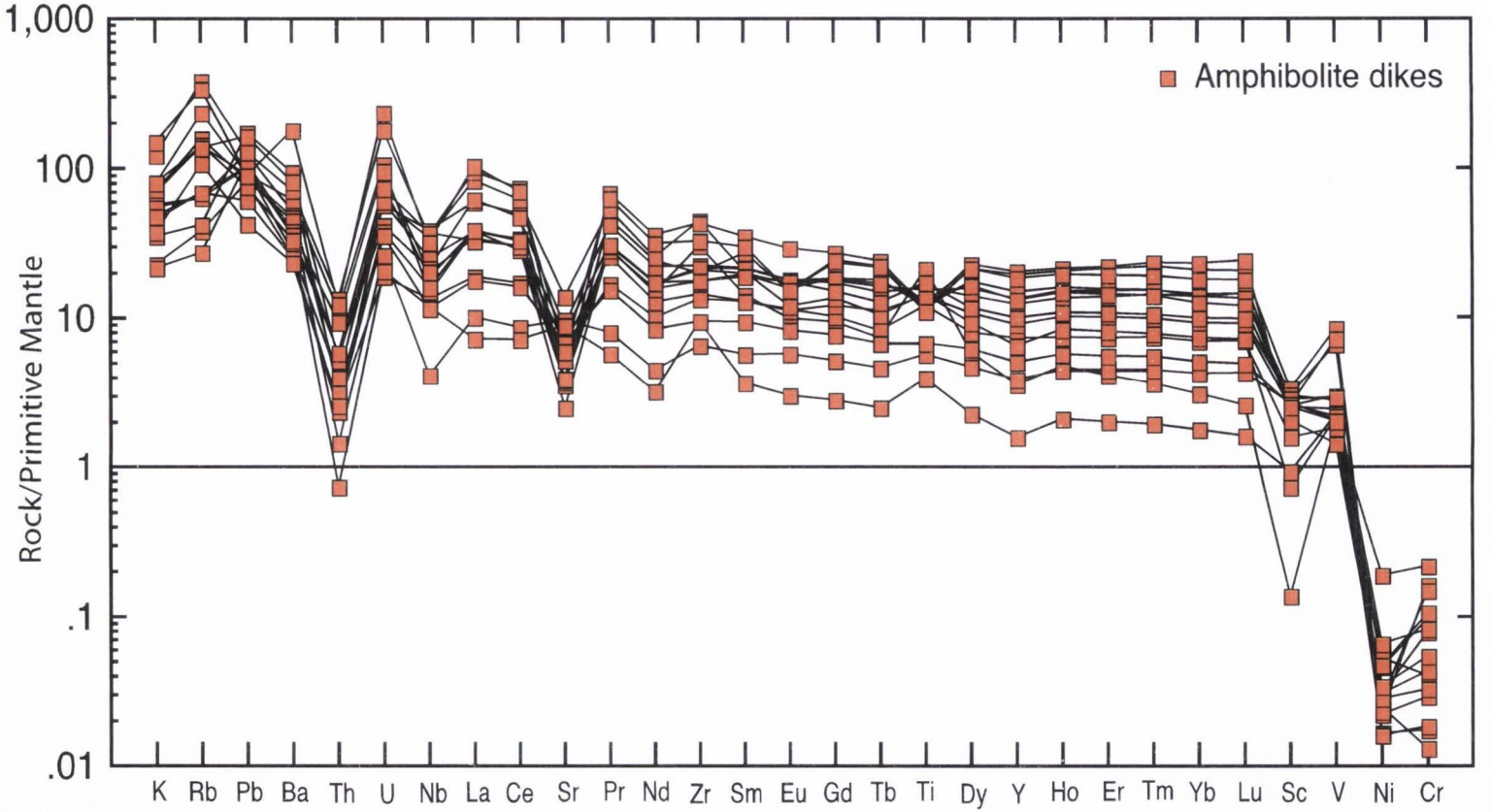

Figure 3-18. Primitive mantle normalized multi-element diagram for the FCC amphibolite dikes.

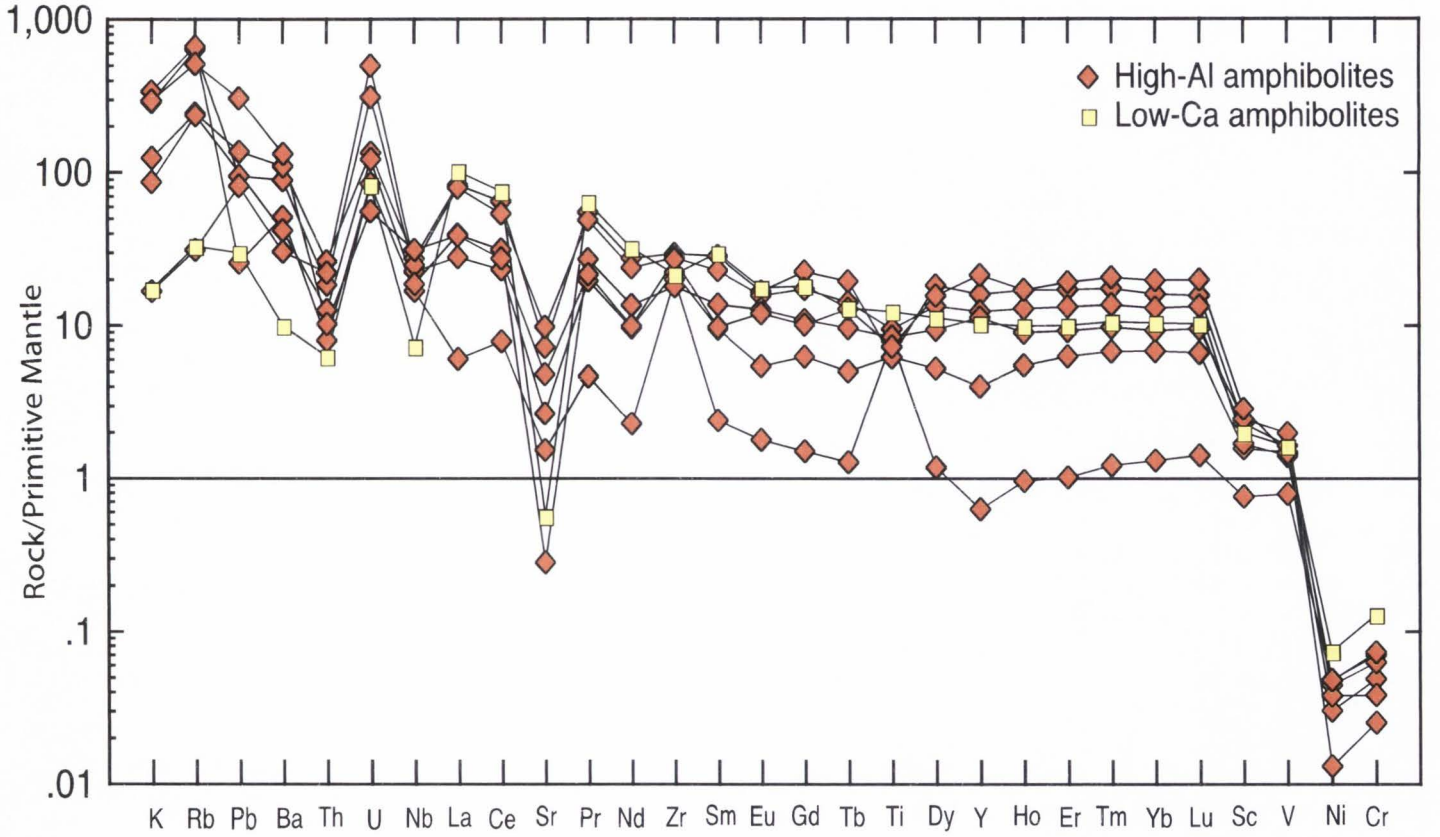

Figure 3-19. Primitive mantle normalized multi-element digram of the FCC high-Al and low-Ca amphibolites.

Table 3-3. Major and Trace element analyses of Komatiites, Farmington Canyon Complex.

Sample#	FCC-122-1	FCC-122-2	FCC-124-3	FCC-124-4
Lithology	Komatiites	Komatiites	Komatiites	Komatiites
SiO2%	49.53	46.87	48.27	47.46
TiO2%	0.16	0.39	0.41	0.42
Al2O3%	3.89	6.70	7.38	6.99
FeO*%	10.38	11.10	10.44	10.75
MnO%	0.08	0.15	0.17	0.13
MgO%	32.37	26.55	23.98	25.49
CaO%	3.07	7.02	8.04	7.45
Na2O%	0.26	0.59	0.61	0.66
K2O%	0.04	0.12	0.10	0.09
P2O5%	0.05	0.11	0.13	0.13
MG#	86.03	81.13	80.00	80.73
Ti (ppm)	963	2312	2478	2538
Nb_xrf (ppm)	1.2	1.8	1.5	2.6
Nb (ppm)	0.6	0.8	1.0	1.1
Zr (ppm)	18	21	23	29
Y_xfr (ppm)	6	6	8	9
Y (ppm)	4	6	7	8
Sr (ppm)	17	20	11	67
Rb (ppm)	1	2		2
Rb_I (ppm)				
Sc_xrf (ppm)	11.5	18.1	22.1	20.0
Sc (ppm)	0.2	15.5	22.6	16.8
V_xrf (ppm)	121	138	162	164
V (ppm)				
Cr (ppm)	3025	2234	2734	2642
Cr_I (ppm)				
Ni (ppm)	1861	1226	1198	1443
Co (ppm)				
Cu (ppm)	11	58	60	6
Zn (ppm)	84	50	58	66
Ba_xrf (ppm)	11		30	17
Ba (ppm)	15	2	22	22
La (ppm)	1.24	0.97	1.38	3.01
Ce (ppm)	3.10	2.90	3.91	5.73
Pr (ppm)	0.48	0.49	0.62	0.97
Nd (ppm)	2.28	2.46	2.96	4.32
Eu (ppm)	0.20	0.17	0.21	0.34
Sm (ppm)	0.66	0.79	0.92	1.17
Gd (ppm)	0.91	1.05	1.23	1.48
Tb (ppm)	0.16	0.20	0.22	0.27
Dy (ppm)	0.95	1.20	1.34	1.59
Ho (ppm)	0.20	0.26	0.29	0.34
Er (ppm)	0.56	0.70	0.79	0.93
Tm (ppm)	0.08	0.10	0.12	0.13
Yb (ppm)	0.50	0.60	0.69	0.78
Lu (ppm)	0.08	0.09	0.11	0.13
Hf (ppm)	0.31	0.55	0.76	0.68
Ta (ppm)	0.07	0.11	0.16	0.11
Pb (ppm)	3.01	2.34	2.07	7.46
Th (ppm)	0.07	0.11	0.18	0.19
U (ppm)	0.04	0.04	0.06	0.14
K (ppm)	319	1036	867	763
Na (ppm)	1939	4413	4490	4897

diagram they are classed as borderline basaltic komatiite and komatiite (Fig 3-4), but on the MgO variation diagrams they are fully komatiite. FeO*/(FeO*+MgO)-Al_2O_3 (Fig 3-5), MgO-Al_2O_3 (Fig 3-8) diagram shows that the FCC komatiites do not appear to trend with the Al-depleted Barberton komatiites, but they do fall in with the "normal" Superior Province komatiites. The MgO variation diagrams (Fig 3-6 through 3-13) and Sun-Nesbitt diagrams show that the FCC komatiites fall well within the ranges of other Archean komatiites and lack the distinctly high CaO/TiO_2 and Al_2O_3/TiO_2 ratios that characterize Phanerozoic boninites (Fig 3-20 and 3-21).

The Cr contents of the komatiites ranged from 2234-3025 ppm and Ni content ranged from 1198-1861 ppm (Table 3-3). Cr and Ni correlate positively with MgO, while the incompatible elements like Zr show a negative correlation (Fig 3-12 and 3-13). Fig 3-22 shows a REE diagram for the FCC komatiites, and shows that initial concentrations are close to that of chondrite and are slightly enriched. Fig 3-23 shows a multi-element plot for the FCC komatiites. This diagram shows a slight enrichment of the compatible elements compared to primitive mantle suggesting sourcing from an enriched source.

Quartzite/ Metachert

Twenty-seven quartzite samples were analyzed for major elements, and twenty-six samples were analyzed for trace element geochemistries as shown in Table 3-4. Quartzite samples have SiO_2 ranging from 85-99.6%, and amounts of Al_2O_3 range from 0.4-12%. One ironstone sample contained as much as 18.3% FeO* while typical values were less than 0.2% FeO*. Harker diagrams show that, as SiO_2 content decreases, both

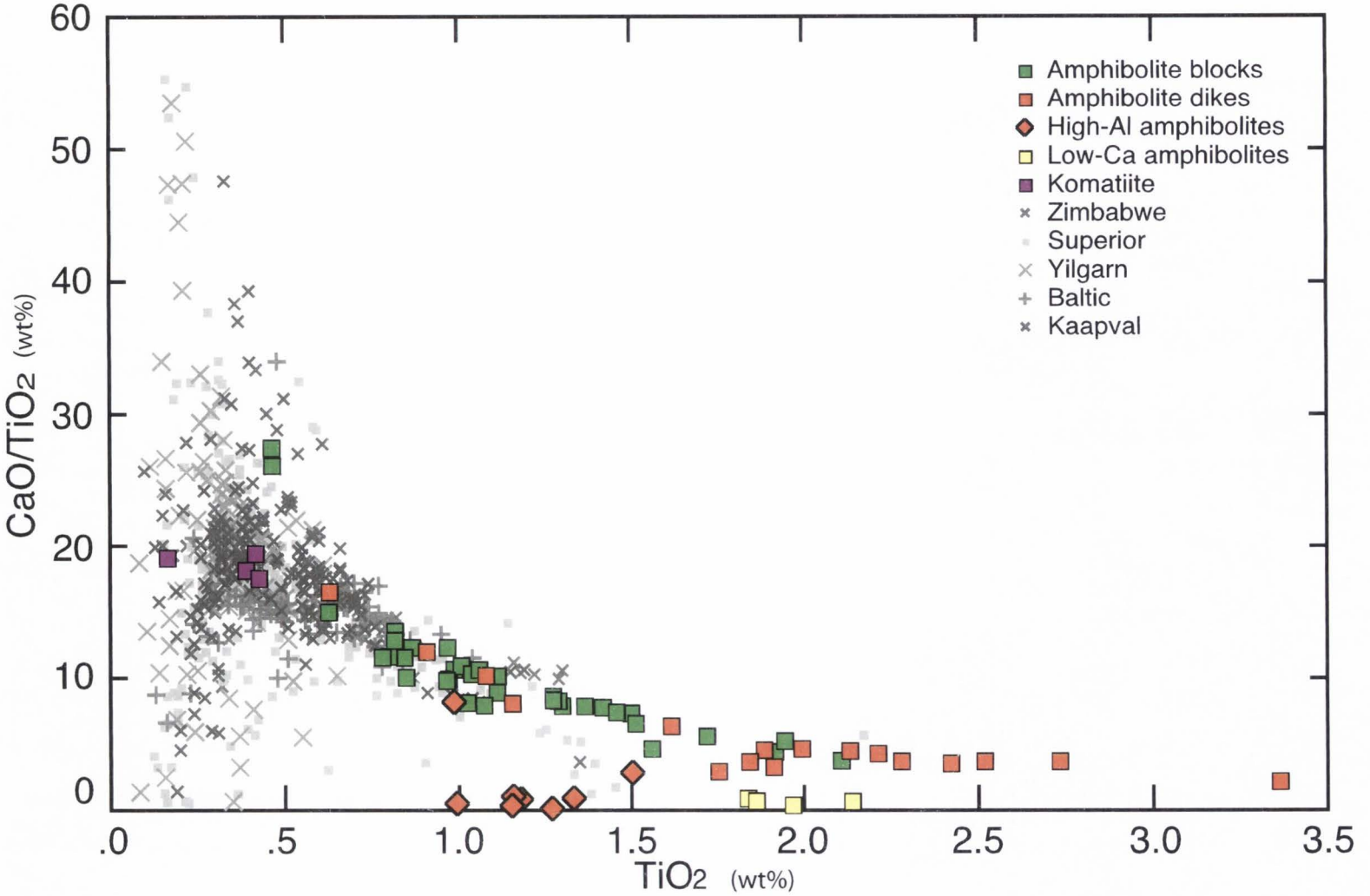

Figure 3-20. Sun & Nesbitt plots for komatiites and related basalts.

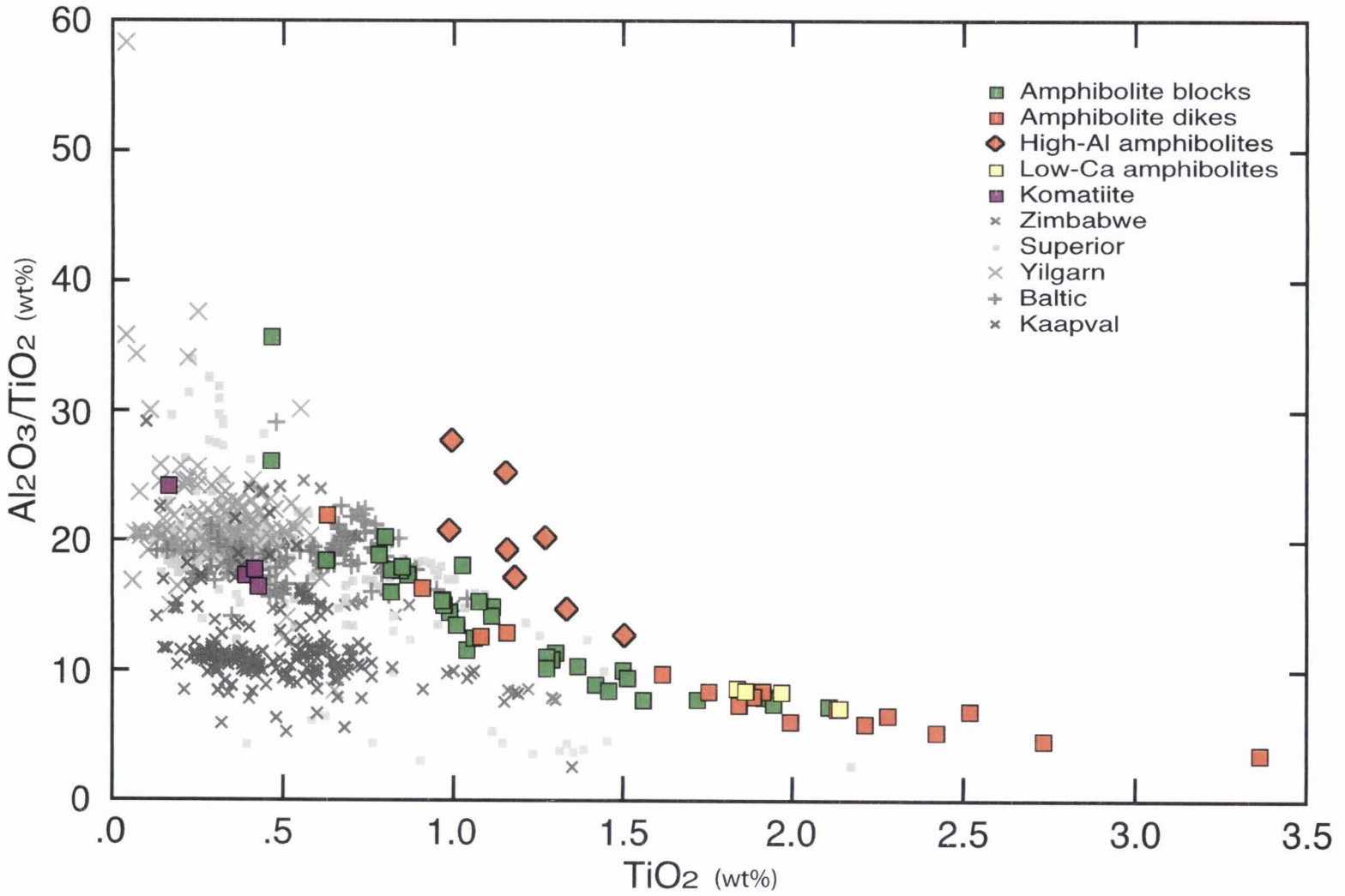

Figure 3-21. Sun & Nesbitt plots for komatiites and related basalts.

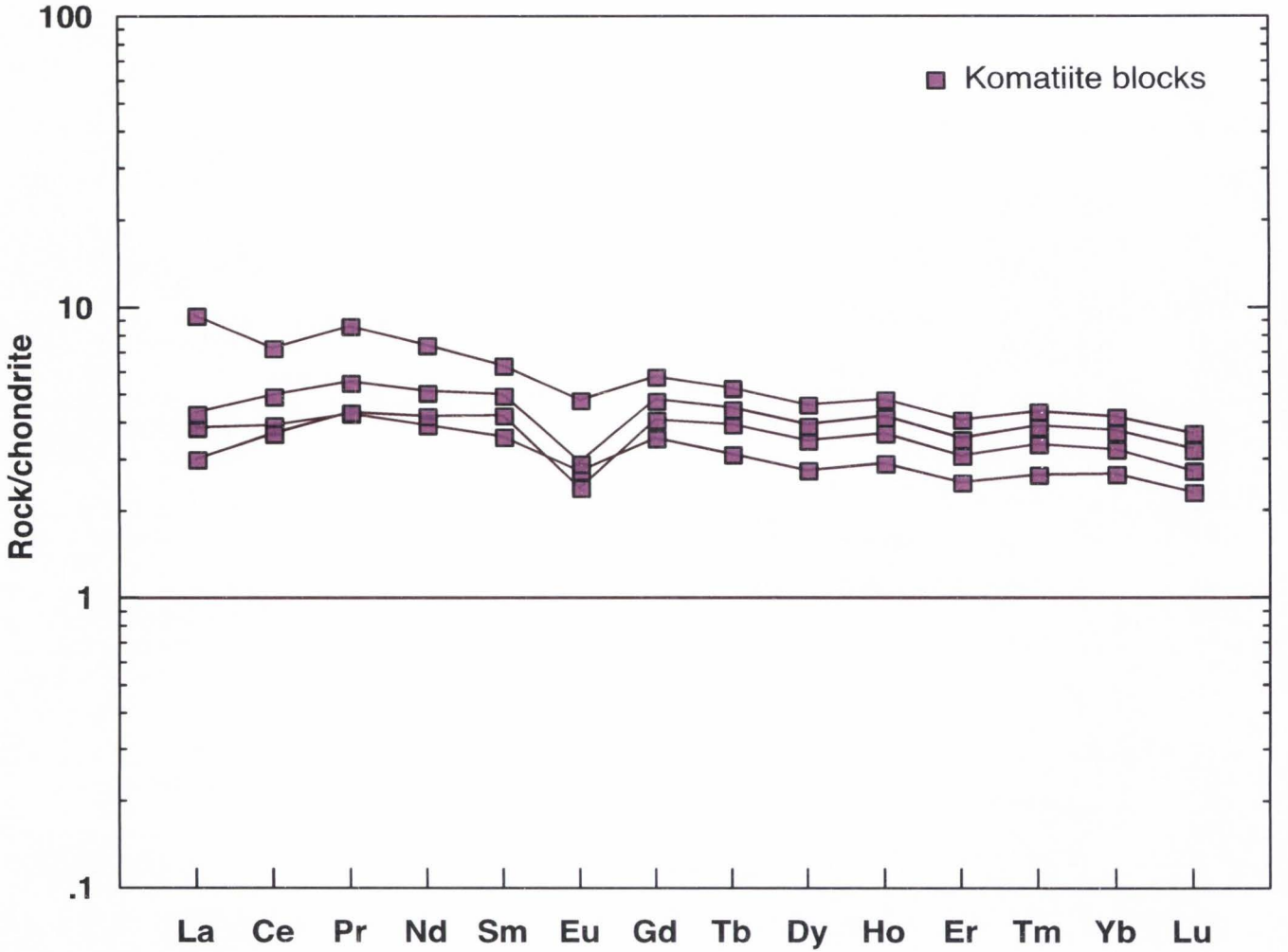

Figure 3-22. Chondrite normalized REE diagram for FCC komatiites.

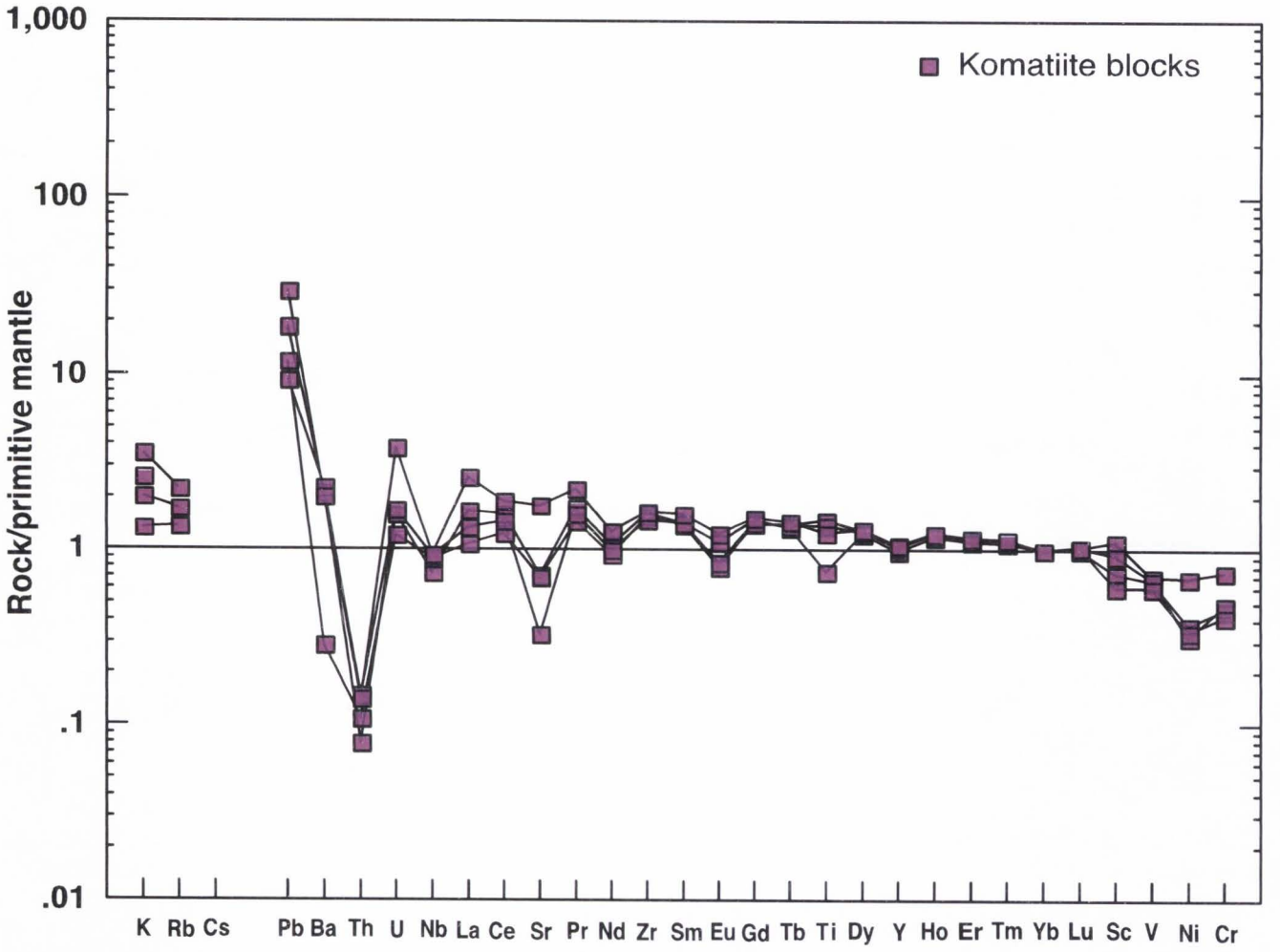

Figure 3-23. Primitive mantle normalized multi-element diagram of the FCC komatiites.

Table 3-4. Major and Trace element analyses of Metacherts and Quartzite, Farmington Canyon Complex.

Sample#	FCC-7-3	FCC-7-4	FCC-13-1	FCC-14-1	FCC-15-1
Lithology	Metachert	Metachert	Metachert	Metachert	Metachert
SiO2%	88.06	95.72	88.84	90.01	86.31
TiO2%	0.19	0.02	0.07	0.05	0.11
Al2O3%	8.05	2.72	6.63	7.77	7.99
FeO*%	1.07	0.26	0.66	0.15	0.88
MnO%	0.01	0.01	0.01		0.01
MgO%	0.66	0.18	0.23	0.16	0.36
CaO%		0.18	0.53		0.18
Na2O%		0.53	2.78		1.69
K2O%	1.82	0.35	0.19	1.95	2.39
P2O5%	0.04	0.01	0.02	0.01	0.02
MG#	50.58	50.04	36.39	59.01	38.66
Ti (ppm)	1139	120	420	300	659
Nb_xrf (ppm)	4.1	1.5	2.9	1.1	2.1
Nb (ppm)	1.7	0.4	1.6	0.5	1.5
Zr (ppm)	173	29	40	35	51
Y_xfr (ppm)	31	3	1	2	4
Y (ppm)	2	3	0		2
Sr (ppm)		20	48	5	42
Rb (ppm)	65	8	2	45	37
Rb_I (ppm)	32.5	7.2	1.8	30.0	31.7
Sc_xrf (ppm)	1.0	2.9	3.6	0.1	0.6
Sc (ppm)	0.6		0.5	1.1	
V_xrf (ppm)	24	10	15	13	28
V (ppm)	15	3	11	7	15
Cr (ppm)	275	20	29		28
Cr_I (ppm)	47	4	16	6	26
Ni (ppm)	13		2		8
Co (ppm)	119.7	142.4	170.9	93.0	66.3
Cu (ppm)	1		136		
Zn (ppm)	1	1	3		4
Ba_xrf (ppm)	221	58	81	37	304
Ba (ppm)	127	54	77	18	277
La (ppm)	14.83	5.12	3.77	0.24	12.35
Ce (ppm)	21.61	7.21	6.22	0.48	21.59
Pr (ppm)	3.89	1.18	0.81	0.06	2.69
Nd (ppm)	14.25	3.82	2.81	0.20	9.12
Eu (ppm)	0.38	0.14	0.23		0.30
Sm (ppm)	2.11	0.59	0.44	0.04	1.41
Gd (ppm)	1.31	0.52	0.28	0.02	0.88
Tb (ppm)	0.15	0.09	0.03		0.11
Dy (ppm)	0.77	0.60	0.15	0.01	0.59
Ho (ppm)	0.10	0.12	0.02		0.09
Er (ppm)	0.20	0.36	0.06	0.01	0.21
Tm (ppm)	0.02	0.05	0.01		0.03
Yb (ppm)	0.09	0.33	0.03		0.18
Lu (ppm)	0.01	0.05	0.01		0.03
Hf (ppm)	0.05	0.06	0.03	0.01	0.02
Ta (ppm)	0.11	0.13	0.19	0.06	0.15
Pb (ppm)	1.01	11.04	3.02	0.72	6.21
Th (ppm)	1.42	2.59	1.81	0.37	3.75
U (ppm)	1.62	2.34	0.17	0.51	0.32
K (ppm)	15108	2905	1577	16187	19839
Na (ppm)		3932	20623		12537

Table 3-4. Major and Trace element analyses of Metacherts and Quartzite, Farmington Canyon Complex.

Sample#	FCC-33-3	FCC-39-3	FCC-36-1	FCC-40-1	FCC-41-1
Lithology	Metachert	Metachert	Metachert	Metachert	Metachert
SiO2%	99.60	88.00	96.43	96.71	98.51
TiO2%	0.01	0.10		0.07	0.04
Al2O3%	0.41	7.43	2.58	2.00	1.26
FeO*%		0.91	0.03	0.32	
MnO%		0.02		0.01	
MgO%	0.10	0.65	0.11	0.29	0.11
CaO%		0.31			
Na2O%		2.37	0.56	0.48	
K2O%	0.04	0.17	0.29	0.16	0.21
P2O5%		0.03		0.01	
MG#	93.72	56.89	81.48	54.65	88.06
Ti (ppm)	60	621		420	240
Nb_xrf (ppm)	4.6	3.9	2.5	1.4	1.8
Nb (ppm)	0.1	2.4	0.1	0.5	0.2
Zr (ppm)	243	72	155	43	28
Y_xfr (ppm)	1	2	3	1	1
Y (ppm)	1	1	0	1	1
Sr (ppm)		20	8	5	1
Rb (ppm)		2	6	11	13
Rb_I (ppm)	2.0	3.4	7.7	11.3	13.4
Sc_xrf (ppm)	2.0	0.9	1.9		0.8
Sc (ppm)		1.4	1.0		
V_xrf (ppm)	6	26		14	6
V (ppm)	1	17	1	5	2
Cr (ppm)		89	3	24	7
Cr_I (ppm)	0	32		16	15
Ni (ppm)		11		2	
Co (ppm)	210.0	69.7	181.5	120.3	114.0
Cu (ppm)		1			
Zn (ppm)		8		17	1
Ba_xrf (ppm)	1	40	49		10
Ba (ppm)	2	46	38	3	14
La (ppm)	0.54	4.71	0.11	4.75	6.57
Ce (ppm)	1.02	8.78	0.25	8.21	12.00
Pr (ppm)	0.11	1.18	0.03	1.12	1.46
Nd (ppm)	0.36	4.25	0.09	3.72	5.08
Eu (ppm)	0.01	0.19	0.02	0.09	0.10
Sm (ppm)	0.06	0.72	0.03	0.54	0.76
Gd (ppm)	0.05	0.48	0.02	0.32	0.41
Tb (ppm)	0.01	0.06		0.04	0.04
Dy (ppm)	0.12	0.31	0.03	0.17	0.20
Ho (ppm)	0.03	0.07	0.01	0.03	0.03
Er (ppm)	0.11	0.13	0.02	0.06	0.06
Tm (ppm)	0.02	0.02		0.01	0.01
Yb (ppm)	0.11	0.16	0.02	0.05	0.03
Lu (ppm)	0.02	0.01		0.01	
Hf (ppm)	0.23	0.08	0.63	0.07	0.06
Ta (ppm)	0.01	0.34	0.02	0.05	0.06
Pb (ppm)		6.44	2.27	8.76	2.31
Th (ppm)	0.30	4.14	0.93	2.07	1.76
U (ppm)	0.15	0.46	1.62	0.44	0.32
K (ppm)	332	1442	2407	1328	1743
Na (ppm)		17598	4154	3561	

Table 3-4. Major and Trace element analyses of Metacherts and Quartzite, Farmington Canyon Complex.

Sample#	FCC-42-3	FCC-54-1	FCC-56-2	FCC-63-2	FCC-67-1
Lithology	Metachert	Metachert	Metachert	Metachert	Metachert
SiO2%	97.08	95.81	94.75	92.28	85.00
TiO2%	0.05	0.04	0.05	0.03	0.11
Al2O3%	2.43	3.54	3.41	4.51	11.94
FeO*%		0.08	0.05	0.20	0.22
MnO%				0.01	0.01
MgO%	0.09	0.09	0.13	0.15	0.10
CaO%			0.21	0.02	
Na2O%		0.02	1.29	0.45	0.24
K2O%	0.46	0.48	0.06	2.26	2.38
P2O5%	0.01			0.01	
MG#	93.82	64.04	75.57	51.79	41.09
Ti (ppm)	300	240	300	180	659
Nb_xrf (ppm)	4.1	2.4	4.0	2.4	3.3
Nb (ppm)	0.6	0.7	0.5	1.5	
Zr (ppm)	62	36	151	32	85
Y_xfr (ppm)	1	1		7	2
Y (ppm)	0		0	0	
Sr (ppm)	5	5	19	59	12
Rb (ppm)	14	21	8	64	129
Rb_I (ppm)	14.1	18.1	7.6	51.8	
Sc_xrf (ppm)	0.4	3.5	3.6	3.8	2.7
Sc (ppm)					
V_xrf (ppm)	4	3	6	10	31
V (ppm)	1	5	3	3	
Cr (ppm)		21	14	20	195
Cr_I (ppm)	6	5	18	5	
Ni (ppm)				1	
Co (ppm)	208.5	194.6	194.1	120.4	
Cu (ppm)				3	2
Zn (ppm)			1	1	2
Ba_xrf (ppm)	51	10	48	498	74
Ba (ppm)	45	12	40	262	
La (ppm)	2.54	0.44	1.01	0.65	
Ce (ppm)	5.93	0.97	1.61	1.03	
Pr (ppm)	0.76	0.11	0.26	0.15	
Nd (ppm)	2.95	0.35	0.86	0.60	
Eu (ppm)	0.07	0.01	0.04	0.05	
Sm (ppm)	0.52	0.05	0.14	0.16	
Gd (ppm)	0.28	0.02	0.08	0.10	
Tb (ppm)	0.03		0.01	0.02	
Dy (ppm)	0.11	0.01	0.05	0.10	
Ho (ppm)	0.01		0.01	0.02	
Er (ppm)	0.03		0.02	0.06	
Tm (ppm)				0.01	
Yb (ppm)	0.01		0.02	0.07	
Lu (ppm)				0.01	
Hf (ppm)	0.05	0.04	0.09	0.05	
Ta (ppm)	0.13	0.08	0.06	0.38	
Pb (ppm)	2.29	0.80	2.64	16.50	
Th (ppm)	1.21	0.39	0.81	0.49	
U (ppm)	0.43	0.19	0.21	0.95	
K (ppm)	3818	3984	498	18760	19756
Na (ppm)		148	9570	3338	1780

Table 3-4. Major and Trace element analyses of Metacherts and Quartzite, Farmington Canyon Complex.

Sample#	FCC-71-1	FCC-88-3	FCC-97-3	FCC-100-1	FCC-122-4B
Lithology	Metachert	Metachert	Metachert	Metachert	Metachert
SiO2%	95.40	86.26	90.99	96.18	96.35
TiO2%	0.05	0.11	0.03	0.02	0.14
Al2O3%	3.00	7.86	7.35	2.44	3.00
FeO*%	0.11	1.01	0.09	0.13	0.05
MnO%	0.01	0.01			
MgO%	0.16	0.39	0.13	0.11	0.11
CaO%	0.17	1.35			
Na2O%	0.93	1.72	0.22	0.72	0.02
K2O%	0.16	1.21	1.17	0.36	0.36
P2O5%		0.05		0.01	
MG#	67.92	41.75	69.09	59.22	70.36
Ti (ppm)	300	634	180	120	839
Nb_xrf (ppm)	1.1	5.5	1.5	1.2	6.3
Nb (ppm)	0.2	4.2	0.9	0.7	0.8
Zr (ppm)	37	62	38	10	219
Y_xfr (ppm)		7		2	3
Y (ppm)	0	2		0	2
Sr (ppm)	23	202	10	15	1
Rb (ppm)	3	47	63	16	9
Rb_I (ppm)	2.8	37.5	40.3	14.9	12.2
Sc_xrf (ppm)	4.1	3.7	2.1	2.0	2.8
Sc (ppm)	0.2	1.6			
V_xrf (ppm)	13	19	11	8	8
V (ppm)	7	14	6	4	4
Cr (ppm)	16	136		54	152
Cr_I (ppm)	8	13	7	3	38
Ni (ppm)		7			
Co (ppm)	132.3	63.8	134.9	266.8	110.1
Cu (ppm)		5			
Zn (ppm)		16	1	2	
Ba_xrf (ppm)	1	788	79	15	
Ba (ppm)	6	751	38	22	20
La (ppm)	0.95	11.59	0.19	0.88	11.23
Ce (ppm)	1.03	23.16	0.41	1.77	23.79
Pr (ppm)	0.19	2.71	0.05	0.19	2.86
Nd (ppm)	0.64	9.66	0.20	0.73	9.73
Eu (ppm)	0.06	0.62	0.01	0.04	0.18
Sm (ppm)	0.11	1.75	0.04	0.17	1.32
Gd (ppm)	0.06	1.11	0.02	0.14	0.95
Tb (ppm)	0.01	0.14		0.02	0.15
Dy (ppm)	0.04	0.64	0.01	0.11	0.80
Ho (ppm)	0.01	0.10		0.02	0.12
Er (ppm)	0.01	0.18		0.04	0.22
Tm (ppm)		0.02		0.01	0.02
Yb (ppm)	0.01	0.09		0.04	0.08
Lu (ppm)		0.01		0.01	0.01
Hf (ppm)	0.02	0.11	0.03	0.02	0.06
Ta (ppm)	0.03	0.42	0.14	0.07	0.13
Pb (ppm)	1.56	30.78	1.60	1.11	1.58
Th (ppm)	0.12	4.42	0.29	0.14	10.55
U (ppm)	0.05	0.86	0.12	0.77	0.93
K (ppm)	1328	10074	9712	2988	2988
Na (ppm)	6899	12756	1632	5341	148

Table 3-4. Major and Trace element analyses of Metacherts and Quartzite, Farmington Canyon Complex.

Sample#	FCC-125-1C	FCC-152-1	FCC-163-2	FCC-165-1	FCC-167-1
Lithology	Metachert	Metachert	Metachert	Metachert	Metachert
SiO2%	90.11	96.57	89.77	86.14	87.88
TiO2%	0.09	0.01	0.03	0.04	0.07
Al2O3%	7.95	1.28	7.96	10.97	10.35
FeO*%	0.47	1.74	0.06	0.23	0.23
MnO%		0.01			
MgO%	0.24	0.51	0.11	0.18	0.10
CaO%					
Na2O%	0.12		0.43	0.19	0.03
K2O%	0.97	0.01	1.68	2.24	1.38
P2O5%				0.01	
MG#	42.38	33.08	74.80	53.91	44.10
Ti (ppm)	540	60	180	240	420
Nb_xrf (ppm)	5.1	0.5	0.5	5.8	2.2
Nb (ppm)	2.4	0.0	0.2	2.5	1.3
Zr (ppm)	158		34	50	57
Y_xfr (ppm)	1		2	3	3
Y (ppm)		0		0	0
Sr (ppm)	11	2	8	15	3
Rb (ppm)	43	1	70	89	59
Rb_I (ppm)	24.5	1.0	50.5	39.3	35.7
Sc_xrf (ppm)	3.0	0.3	0.6	1.9	0.3
Sc (ppm)		0.5	0.3		
V_xrf (ppm)	15	13	1	12	16
V (ppm)	10	10	3	8	9
Cr (ppm)	103	120	2	17	107
Cr_I (ppm)	74	1	5	19	13
Ni (ppm)	2	5		1	
Co (ppm)	187.5	184.3	154.7	116.1	94.0
Cu (ppm)	5	56			
Zn (ppm)	7	16	2		2
Ba_xrf (ppm)	73	8	52	196	13
Ba (ppm)	37	8	22	38	4
La (ppm)	0.20	0.08	0.59	1.30	2.02
Ce (ppm)	0.33	0.07	1.08	2.55	4.08
Pr (ppm)	0.05	0.02	0.13	0.34	0.49
Nd (ppm)	0.17	0.08	0.42	1.17	1.63
Eu (ppm)	0.01	0.01	0.01	0.02	0.02
Sm (ppm)	0.03	0.03	0.06	0.17	0.25
Gd (ppm)	0.02	0.03	0.02	0.09	0.14
Tb (ppm)		0.01		0.01	0.02
Dy (ppm)	0.01	0.04	0.02	0.06	0.09
Ho (ppm)		0.01		0.01	0.01
Er (ppm)	0.01	0.03		0.02	0.03
Tm (ppm)					
Yb (ppm)		0.02		0.01	0.01
Lu (ppm)					
Hf (ppm)	0.09		0.02	0.04	0.02
Ta (ppm)	0.09	0.03	0.04	0.26	0.22
Pb (ppm)	2.01	2.96	2.86	2.07	1.20
Th (ppm)	0.07	0.04	0.64	2.04	3.49
U (ppm)	0.11	0.88	0.20	0.57	0.73
K (ppm)	8052	83	13946	18594	11455
Na (ppm)	890		3190	1409	223

Table 3-4. Major and Trace element analyses of Metacherts and Quartzite, Farmington Canyon Complex.

Sample#	FCC-175-3B	FCC-1-1B	FCC-122-5	FCC-44-1
Lithology	Metachert	Schist parting	Ironstone	Tintic Fm
SiO2%	84.76	68.90	72.67	99.74
TiO2%	0.08	0.20	0.52	0.05
Al2O3%	9.41	15.55	5.89	0.27
FeO*%	0.73	5.18	18.29	0.00
MnO%	0.01	0.06	0.07	0.00
MgO%	0.51	4.15	1.87	0.09
CaO%	1.83	0.55	0.43	0.00
Na2O%	0.79	3.99		0.00
K2O%	1.83	1.34	0.02	0.05
P2O5%	0.01	0.01	0.18	
MG#	48.49	53.89	15.02	95.00
Ti (ppm)	480	1199	3117	300
Nb_xrf (ppm)	1.2	3.9	7.5	2.7
Nb (ppm)	0.7	2.0	3.8	0.6
Zr (ppm)	55	104	485	71
Y_xfr (ppm)		7	48	6
Y (ppm)	0	2	45	3
Sr (ppm)	58	10		3
Rb (ppm)	68	58		
Rb_I (ppm)	34.4	23.6	0.8	1.6
Sc_xrf (ppm)	4.1	5.7	5.3	1.4
Sc (ppm)		8.6	18.3	1.6
V_xrf (ppm)	19	75	199	
V (ppm)	11	46	175	1
Cr (ppm)	20	90	387	
Cr_I (ppm)	12	35	167	2
Ni (ppm)	5	35	26	
Co (ppm)	92.1	29.0	81.3	285.6
Cu (ppm)		20	23	
Zn (ppm)	4	61	20	
Ba_xrf (ppm)	162	55	30	13
Ba (ppm)	144	36	26	31
La (ppm)	1.23	5.22	39.14	3.97
Ce (ppm)	1.48	7.83	97.35	9.27
Pr (ppm)	0.16	0.99	11.90	1.13
Nd (ppm)	0.43	3.77	43.33	4.39
Eu (ppm)	0.10	0.23	0.74	0.14
Sm (ppm)	0.07	0.65	8.06	0.85
Gd (ppm)	0.02	0.53	6.69	0.56
Tb (ppm)		0.07	1.22	0.08
Dy (ppm)	0.02	0.41	8.63	0.54
Ho (ppm)		0.08	2.01	0.11
Er (ppm)	0.01	0.21	6.51	0.35
Tm (ppm)		0.03	1.03	0.05
Yb (ppm)	0.01	0.19	6.74	0.37
Lu (ppm)		0.03	1.00	0.06
Hf (ppm)	0.03	0.07	0.16	0.61
Ta (ppm)	0.08	0.32	0.31	0.02
Pb (ppm)	6.11	5.23	1.03	0.80
Th (ppm)	1.29	2.38	32.06	1.06
U (ppm)	0.11	0.58	3.97	0.59
K (ppm)	15191	11123	166	415
Na (ppm)	5861	29599		

Al_2O_3 and K_2O increase (Fig 3-24). A ternary diagram of MgO-Al_2O_3-FeO* shows that the FCC quartzites are clustered together in the Al_2O_3 field indicating high clay-bearing compositions, and no hydrothermal Fe (Fig 3-25). Ternary diagrams such as a K_2O-CaO-MgO (Fig 3-26) and Na_2O-CaO-MgO (Fig 3-27) have been used to discriminate between marine and freshwater depositional environments for cherts (Dasgupta et al., 1998) and can aid in the depositional interpretation of the FCC cherts. The results suggest that these cherts are marine; however, the relationship between Archean cherts and ocean water chemistry is not well known, and these diagrams have not been tested on Archean cherts.

Trace-element analyses of the quartzites show that Th values are typically between 0.04-3.75 ppm (Table 3-4). However, the ironstone has a value of 32 ppm, supporting a hydrothermal origin. REE diagrams normalized to Post-Archean Average Shale (PAAS) show a wide range in absolute concentrations, with La ranging from 0.002x to 0.35x PAAS (1x PAAS for the ironstone; Fig 3-28). Slopes range from slightly LREE-enriched to slightly LREE-depleted and modest positive Eu anomalies are common. This is seen more clearly in PAAS-normalized REE diagrams that are also normalized to Lu (Fig 3-29). These diagrams also illustrate the relatively flat REE-concentration pattern of the schistose parting in FCC quartzite, at about 0.1x PAAS, and the slightly LREE-depleted pattern of the ironstone, with its small negative Eu anomaly.

Spider diagrams normalized to upper continental crust show a marked depletion in HFS elements and U, Zr, and Y. These diagrams also show high concentrations of chromium, nickel and cobalt (Fig 3-30). These elements are high because chromite (Cr)

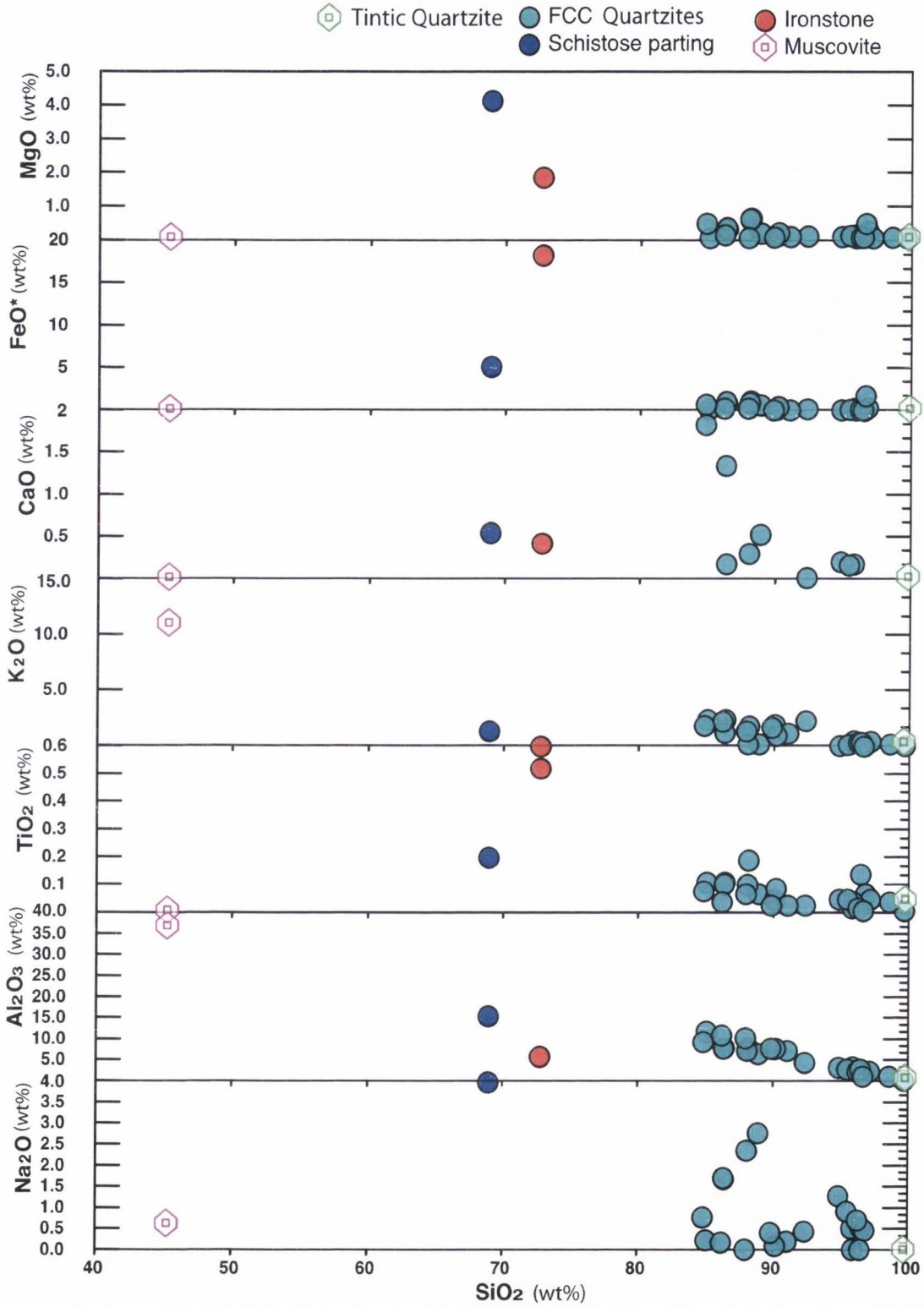

Figure 3-24. Harker diagrams for the FCC quartzites. (Muscovite shows approxiamate composition of fuchsite)

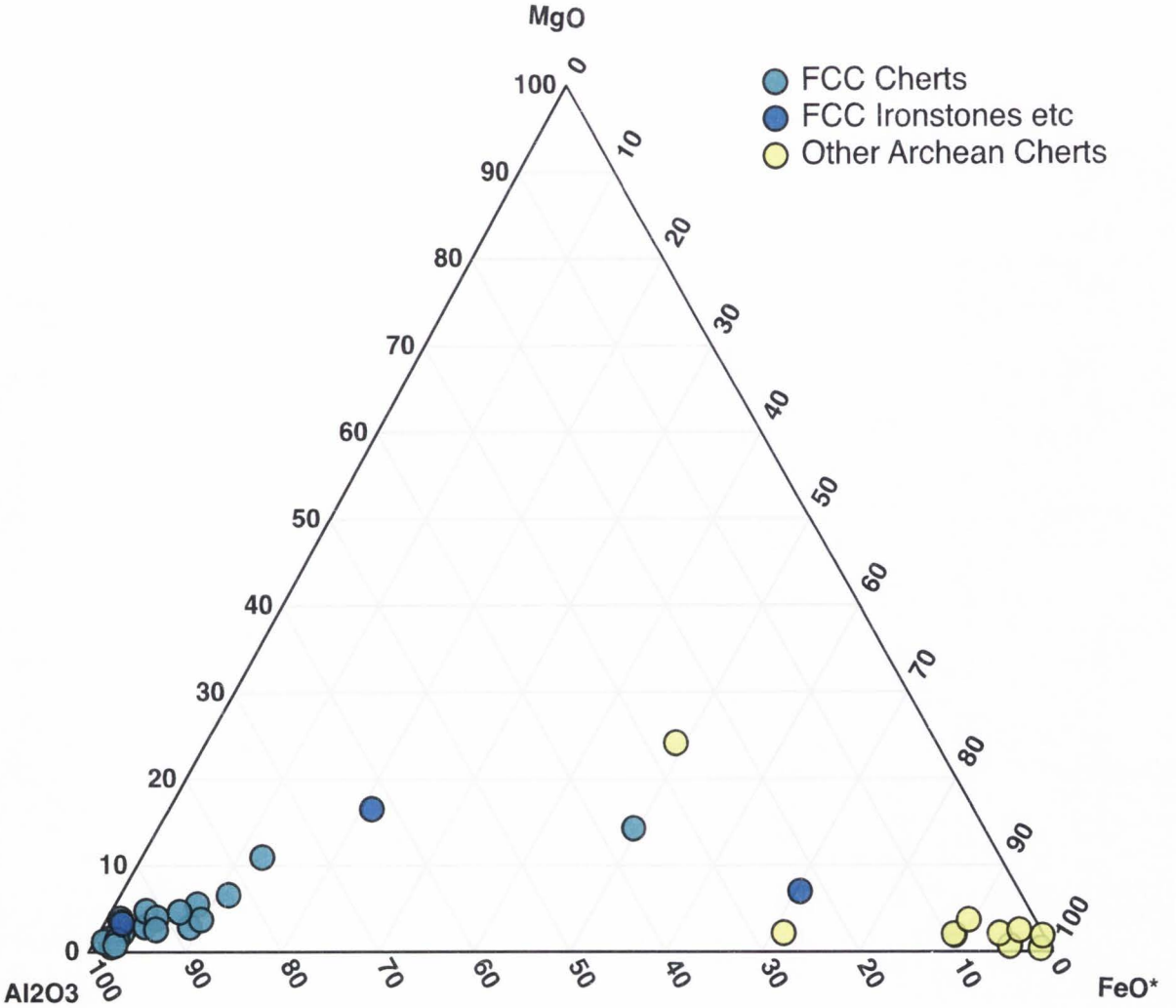

Figure 3-25. MgO vs FeO* vs Al_2O_3 ternary diagram for the FCC cherts.

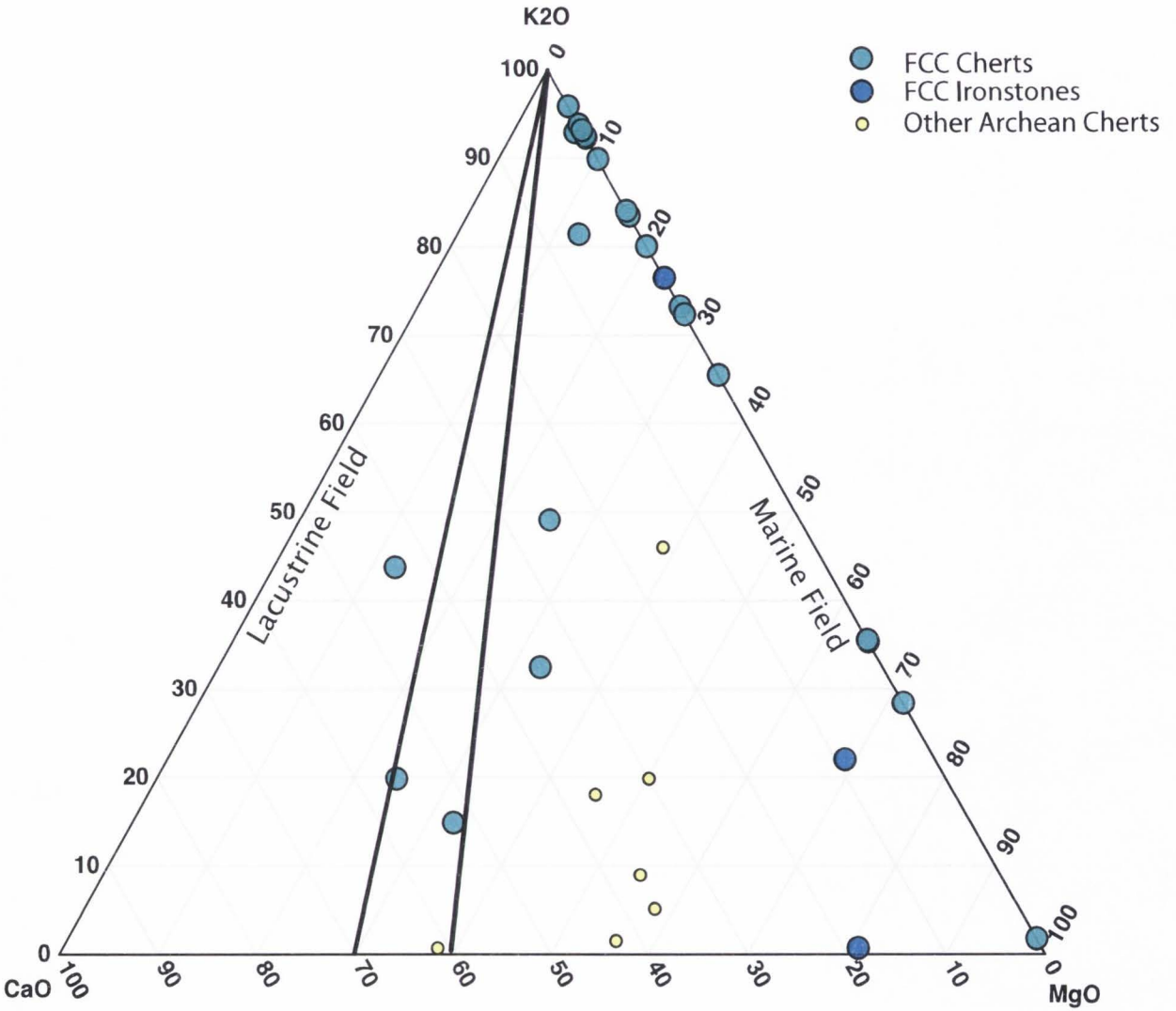

Figure 3-26. K_2O vs CaO vs MgO ternary plot of the FCC cherts.

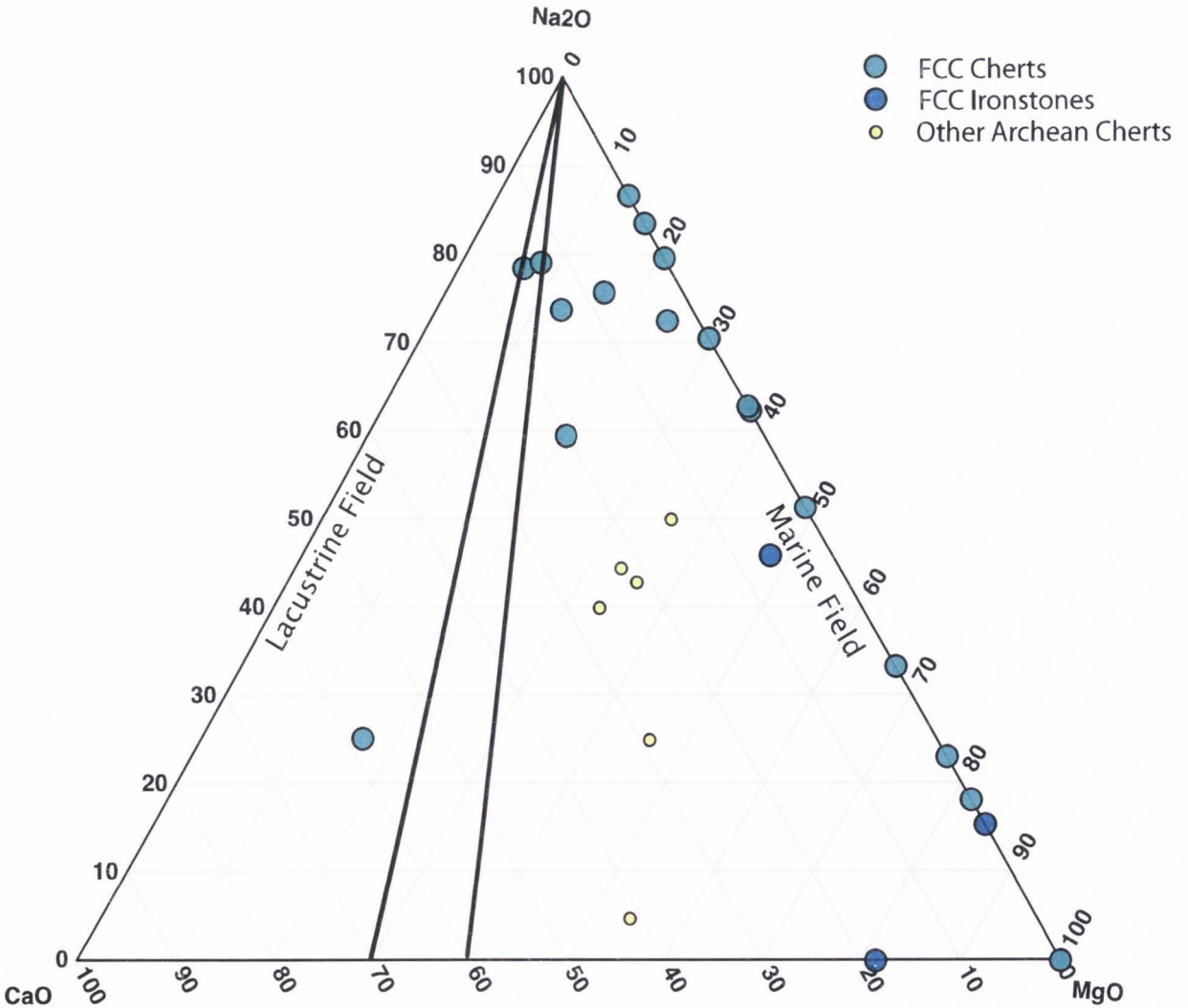

Figure 3-27. Na_2O vs CaO vs MgO ternary plot of the FCC cherts.

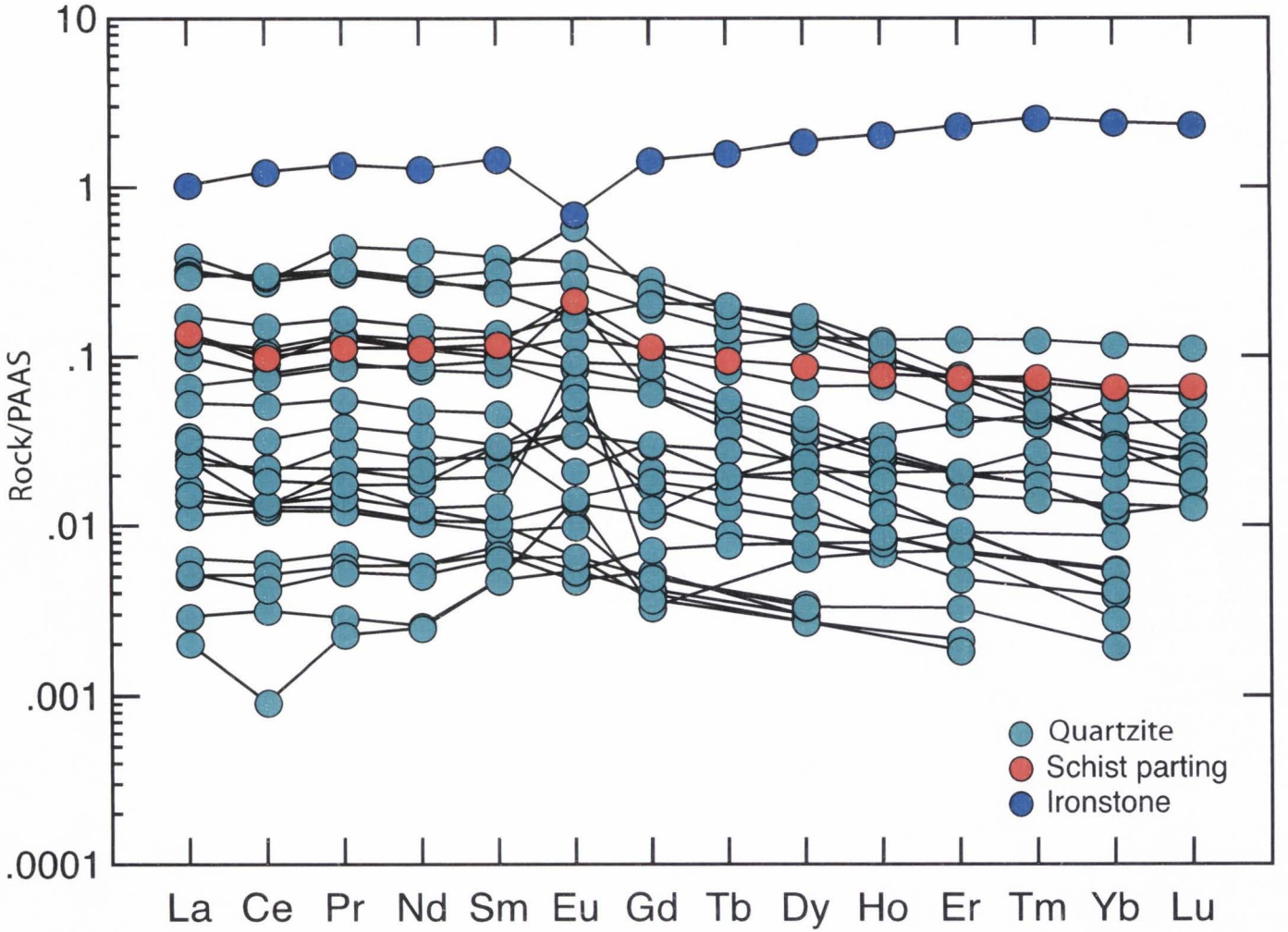

Figure 3-28. PAAS-normalized REE diagram for the FCC Quartzites.

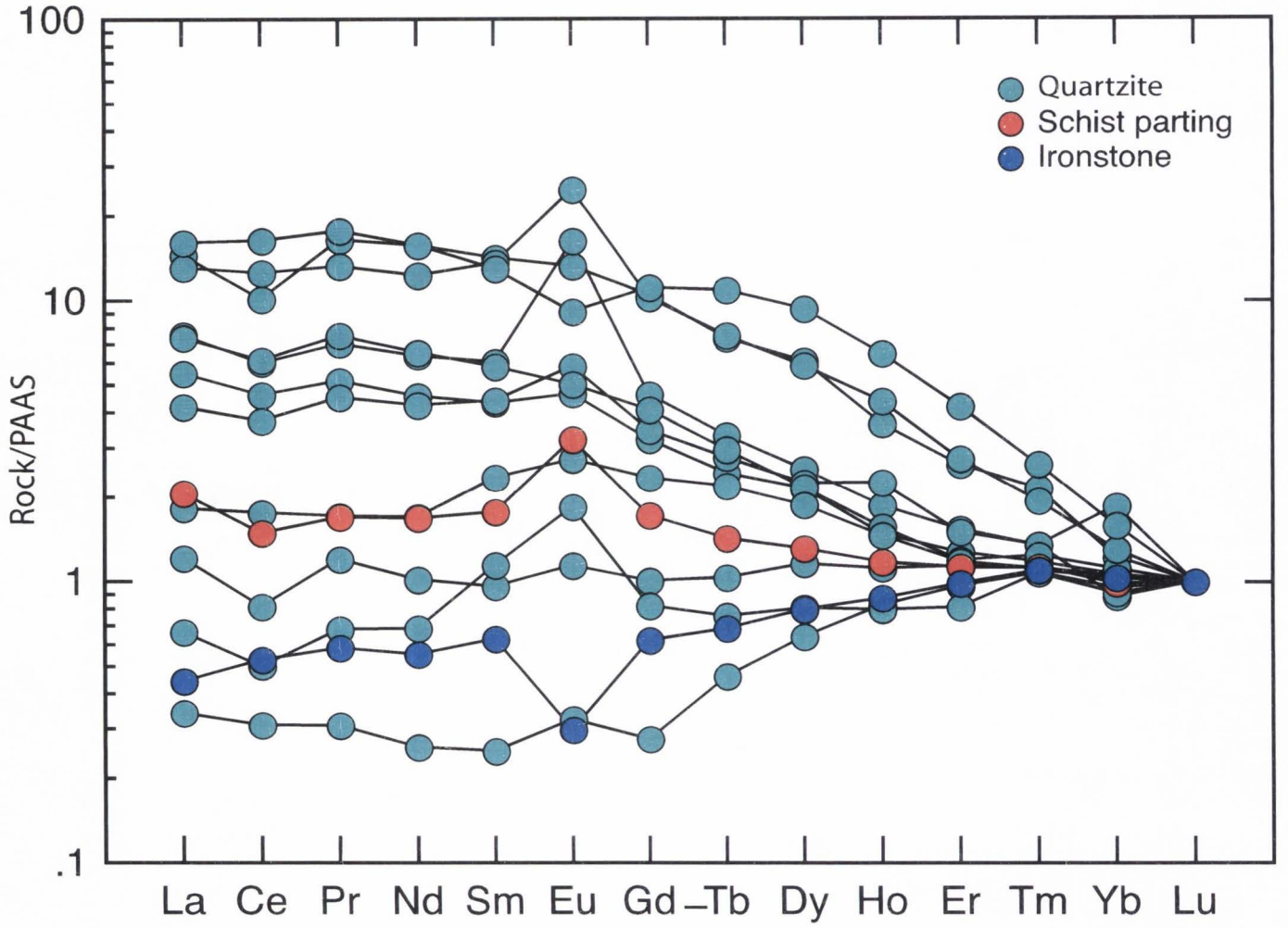

Figure 3-29. PAAS-normalized REE diagram for the FCC quartzites. Normalized to Lu=1.

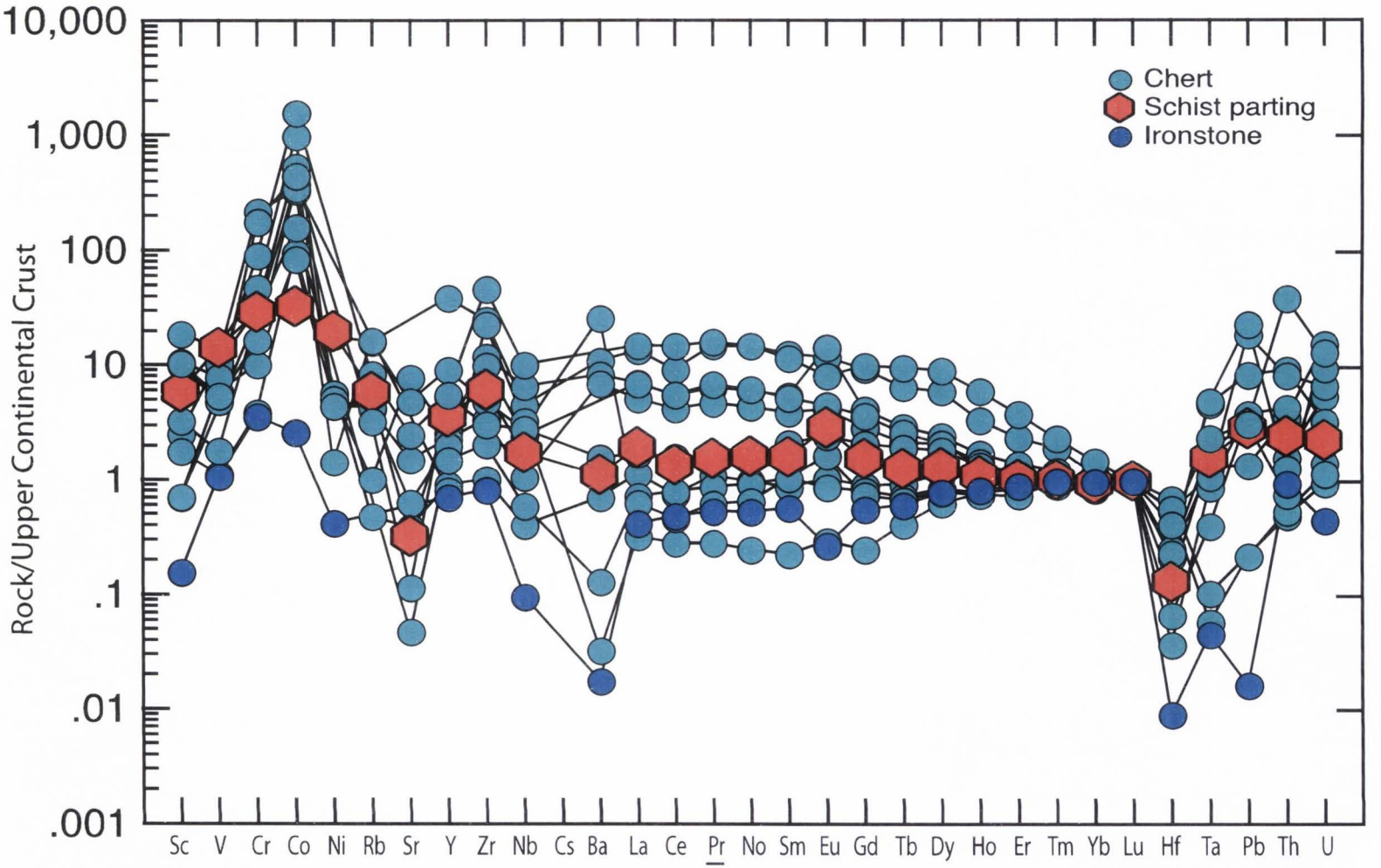

Figure 3-29. Upper-continental crust normalized multi-element variation diagram for the FCC quartzites. Normalized to Lu=1.

and olivine (Ni, Co) are associated with each other. This occurrence indicates a source of Cr-rich Komatiitic volcanic ash.

Twenty-one quartzite samples (including one sample of Cambrian Tintic formation) were analyzed for oxygen isotopes. The FCC quartzites had $\delta^{18}O$ values between 4.6 and 9.6 SMOW, while the Cambrian quartzite had a $\delta^{18}O$ value of 12.6 SMOW (Table 3-6).

Granites and Pegmatites

Six granite and pegmatite samples were analyzed for major and trace elements (compositions shown in Table 3-5). Granite/pegmatite samples have a variation of SiO_2 ranging from 68-89%, FeO* 0.01-2%, and MgO 0.01-0.1%. Amounts of Al_2O_3 and TiO_2 vary and range from 7-20% and 0.0-0.07%, respectively (Figs 3-31 and 3-32). The pegmatites are classified as granites in the IUGS classification, however, some fall well outside this field. More specifically, the sample containing 89% SiO_2 can be easily explained due to non-modal sampling of very coarse grained pegmatites. The pegmatites may be further classified as S-type granites based on their modal muscovite content and the ISMA classification scheme of Chappel and White (1974). Bryant (1988a) points out that some of the ratios, such as molar $Al_2O_3/(Na_2O+K_2O+CaO)$ and $Fe^3/(Fe^2+Fe^3)$, as well as the absence of normative corundum are inconsistent with S-type granites. He cites this as being inheritance of older continental crust that was derived from an older granulite facies metamorphism.

The results of the trace-element chemical analyses of the granite and pegmatite are also shown in Table 3-5. Chondrite-normalized REE diagrams show a slight LREE-

Table 3-5. Major and Trace element analyses of Pegmatites and Granites, Farmington Canyon Complex.

Sample#	FCC-5-3	FCC-6-2	FCC-29-2	FCC-33-1	FCC-37-1	FCC-114-2
Lithology	Pegmatite Granite	Pegmatite Granite	Pegmatite Granite	Pegmatite Granite	Pegmatite Granite	Pegmatite Granite
SiO2%	76.97	68.13	67.97	75.62	88.84	71.55
TiO2%		0.01	0.01			0.07
Al2O3%	13.00	18.47	19.91	13.96	7.43	14.30
FeO*%	0.14	0.39	0.13	0.07	0.01	2.10
MnO%	0.01	0.01	0.02	0.01	0.01	0.01
MgO%	0.01	0.12	0.04	0.02	0.12	0.01
CaO%	0.15	0.76	4.10	0.45	0.52	0.11
Na2O%	1.80	4.24	6.76	1.95	1.32	2.48
K2O%	7.89	7.83	0.99	7.91	1.64	9.33
P2O5%	0.02	0.01	0.08	0.01	0.01	0.01
MG#	15.50	36.13	34.39	31.73	86.06	0.55
Ti (ppm)	15	89	59	30		435
Nb_xrf (ppm)		4.6	1.9		3.1	1.8
Nb (ppm)	0.7	6.8	1.1	0.5	0.4	3.6
Zr (ppm)	13	47	28	33	370	13
Y_xfr (ppm)		66	53	1	9	1
Y (ppm)	1	62	5	1	1	1
Sr (ppm)	54	95	182	153	59	44
Rb (ppm)	208	221	20	209	28	246
Rb_I (ppm)	177.9	208.0	18.9	157.5	26.7	172.4
Sc_xrf (ppm)	2.4	2.6	6.8	0.8	3.2	3.5
Sc (ppm)	3.4	4.3	6.2	2.1	4.0	0.6
V_xrf (ppm)	12	8	3	4	8	10
V (ppm)	1	1	1	1	2	0
Cr (ppm)		2	79			6
Cr_I (ppm)	0	0	1	0	1	
Ni (ppm)		4	1	1	1	
Co (ppm)	67.3	34.0	72.9	49.6	91.4	57.2
Cu (ppm)						
Zn (ppm)	6	7	11	1	5	4
Ba_xrf (ppm)	664	564	75	1329	260	376
Ba (ppm)	611	660	75	2001	206	255
La (ppm)	0.71	7.83	4.62	2.31	0.39	0.33
Ce (ppm)	1.19	15.84	8.44	4.08	0.58	0.55
Pr (ppm)	0.15	1.89	1.04	0.48	0.10	0.07
Nd (ppm)	0.56	7.12	3.81	1.71	0.40	0.29
Eu (ppm)	1.65	0.98	0.58	1.51	0.16	0.47
Sm (ppm)	0.26	2.18	1.05	0.60	0.22	0.19
Gd (ppm)	0.13	2.96	1.24	0.33	0.25	0.14
Tb (ppm)	0.02	0.63	0.23	0.05	0.06	0.03
Dy (ppm)	0.13	4.70	1.34	0.19	0.40	0.18
Ho (ppm)	0.03	1.10	0.23	0.03	0.08	0.03
Er (ppm)	0.08	3.58	0.51	0.06	0.19	0.10
Tm (ppm)	0.01	0.55	0.06	0.01	0.03	0.02
Yb (ppm)	0.06	3.34	0.32	0.04	0.15	0.11
Lu (ppm)	0.01	0.50	0.04	0.01	0.03	0.02
Hf (ppm)	0.01	0.05	0.07	0.23	2.39	0.04
Ta (ppm)	0.06	0.70	0.31	0.53	0.09	0.88
Pb (ppm)	21.00	61.71	45.49	56.27	20.01	37.34
Th (ppm)	0.67	14.00	3.65	1.68	8.40	0.41
U (ppm)	0.32	3.06	1.42	0.42	5.45	0.71
K (ppm)	65528	65006	8177	65685	13644	77419
Na (ppm)	13366	31465	50112	14493	9799	18416

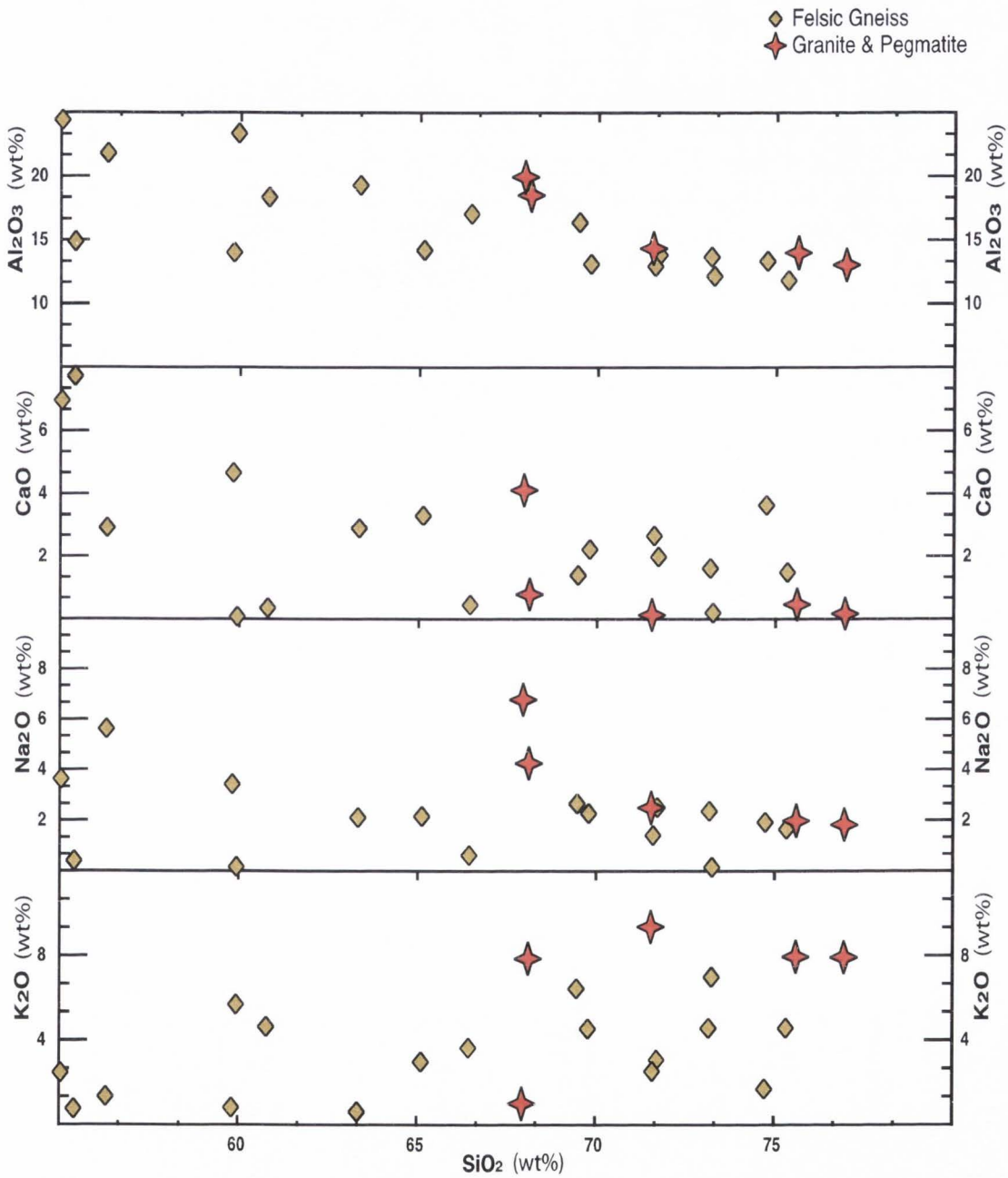

Figure 3-31. Harker diagrams for the FCC granites and pegmatites.

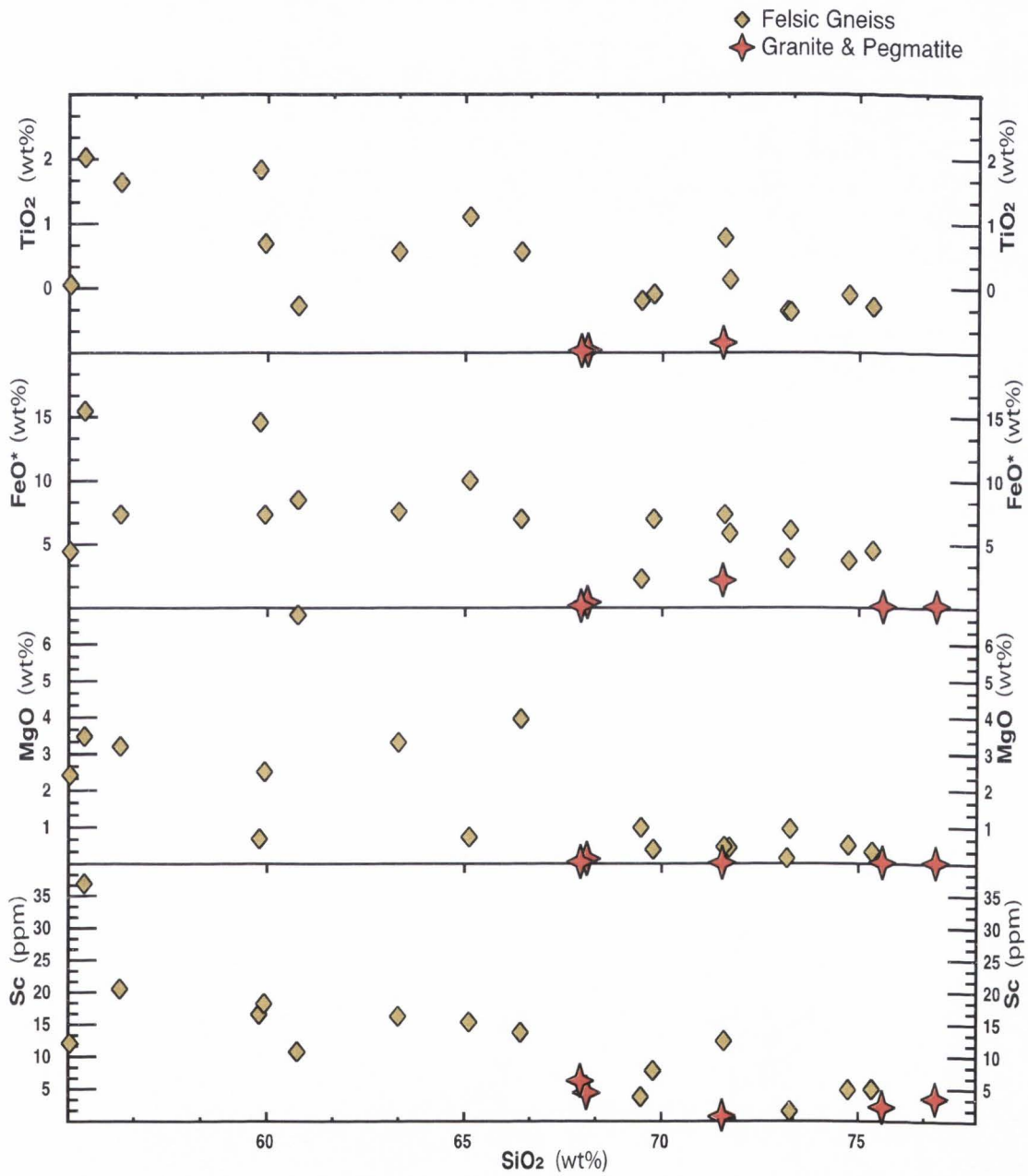

Figure 3-32. Harker diagrams for the FCC granites and pegmatites.

enrichment trend and positive europium anomalies that grow larger as the overall concentration of REE decreases. This is consistent with the accumulation of plagioclase elements (Fig 3-33). Primitive mantle-normalized multi-element diagrams are generally enriched in the more incompatible elements, with negative anomalies at Ti and the transition metals, and positive anomalies at Eu and Sr, consistent with plagioclase accumulation (Fig 3-34).

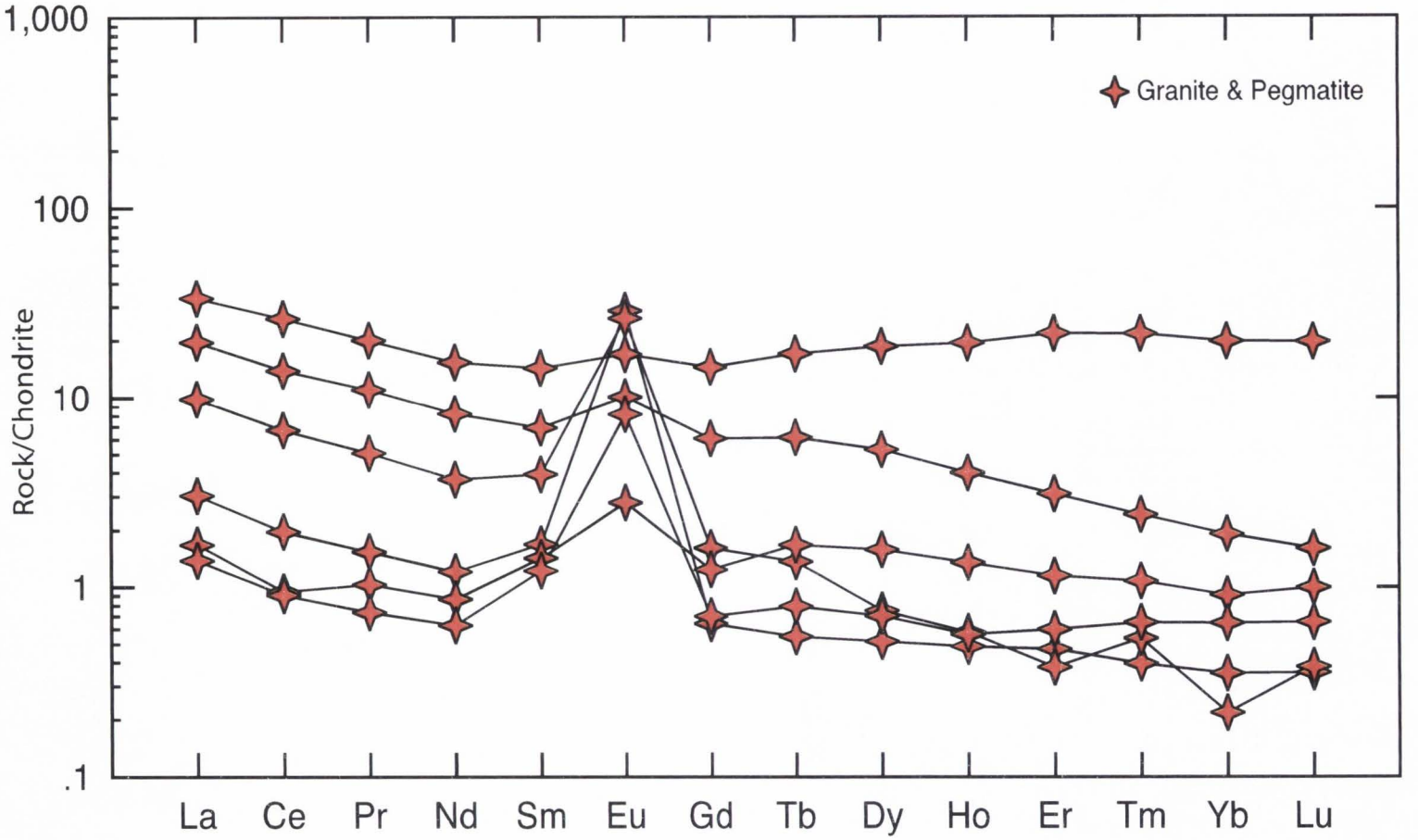

Figure 3-33. Chondrite normalized REE plot of the FCC granites and pegmatites.

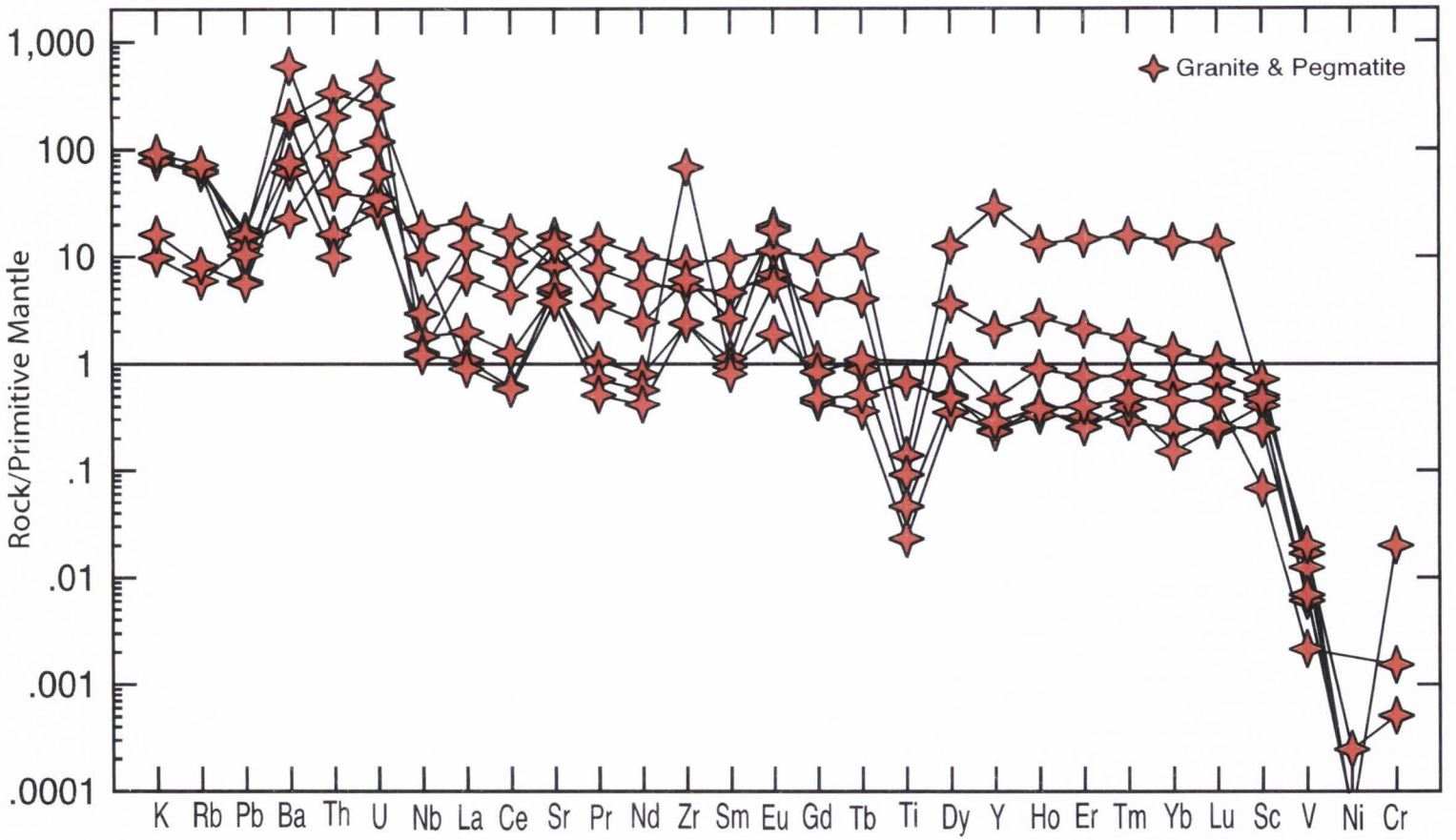

Figure 3-34. Primitive mantle-normalized multi-element plot of the FCC granites and pegmatites.

Table 3-6. Results of Oxygen isotopes for selected FCC rocks

Sample #	δ18O (SMOW)	Repeat δ18O	δD (deuterium)	Mineral sampled	Rock Type
53-1	3.4			whole rock	amphibolite
14-2	4.1			whole rock	amphibolite
33-2	4.4			whole rock	amphibolite
42-1	4.7	5.0		whole rock	amphibolite
35-1	5.3	5.6		whole rock	amphibolite
41-2	5.4			whole rock	amphibolite
1-3B	5.5			whole rock	amphibolite
7-1	5.5			whole rock	amphibolite
56-1	5.5			whole rock	amphibolite
40-2	5.8			whole rock	amphibolite
38-2	5.9			whole rock	amphibolite
175-3A	5.9	6.2		whole rock	amphibolite
7-2	6.4			whole rock	amphibolite
124-4	4.6	4.5		quartz	chert
35-2	5.1			quartz	chert
42-3B	6.4	6.5	-43.0	Fuchsite	chert
1-1B	6.5	6.8		quartz	chert
33-3	7.1			quartz	chert
14-1	7.4			quartz	chert
97-3	7.4			quartz	chert
38-3	8.0	7.9		quartz	chert
13-1	8.2			quartz	chert
36-1	8.2			quartz	chert
175-3B	8.6			quartz	chert
56-2	8.9			quartz	chert
7-4	9.1			quartz	chert
42-3A	9.1			quartz	chert
35-2	9.3			quartz	chert
41-1	9.3			quartz	chert
125-1B	9.3	9.2		quartz	chert
7-3	9.5			quartz	chert
40-1	9.6			quartz	chert
54-1	9.6	9.4		quartz	chert
5-1	4.0	4.0		whole rock	Felsic Gneisss
46-3	5.5			whole rock	Felsic Gneisss
11-1	6.0	6.2		whole rock	Felsic Gneisss
52-2	6.0			whole rock	Felsic Gneisss
12-1	6.7			whole rock	Felsic Gneisss
172-1	7.0			whole rock	Felsic Gneisss
148-2	7.1			whole rock	Felsic Gneisss
39-3	8.2	8.4		whole rock	Felsic Gneisss
91-1	8.5			whole rock	Felsic Gneisss
50-1	9.5	9.3		whole rock	Felsic Gneisss
97-1	7.2			whole rock	Felsic Gneisss
1-4	5.3			whole rock	schist parting
44-1	12.6			quartz	tintic quartzite

CHAPTER 4

DISCUSSION

PETROGENESIS

The petrogenesis of each rock suite must be understood in terms of processes operating both today and in the distant past. It is assumed that igneous processes during the Archean were similar to today, but the conditions of higher heat flow and rapid recycling of crust during the Archean influenced the rate and intensity of these processes. In addition, the low oxygen content of Archean seawater, and lack of marine life commonly associated with the formation of marine sedimentary rocks resulted in significant differences in their formation. In the following section, the petrogenesis of each suite is presented with these caveats in mind.

Quartzo-feldspathic Gneiss/Schist

The major element data of the gneisses support two possible origins: (1) wackes (paragneiss) or (2) felsic volcanic rock-ash. In most of the quartzo-feldspathic layers hornblende, garnet, and biotite are the most significant mafic components, and more than half of the felsic minerals are quartz. Bryant (1988a) hypothesizes that these quartz-rich layers could be derived from tuffaceous sediments, greywacke and arkose. High Na_2O content indicates the high amount of plagioclase in these rocks. Gneisses of the FCC show a generally negative europium anomaly as well as a strong negative strontium anomaly, which are indicative of plagioclase fractionation or removal. This indication of plagioclase fractionation supports the possibility of high volcanic input. Alternatively,

this could reflect the mechanical removal of a weathered feldspar component (clay) during transport, leaving a residue that was enriched in quartz. It is important to understand that the removal of feldspar would predate metamorphism and is not the product of current feldspar removal.

Amphibolites

Major element chemistry of the amphibolites is generally consistent with their origin as mafic igneous rocks, i.e., basalts and gabbros. One question that needs to be answered, and that has direct implications for this study, is understanding the origin(s) of these Archean mafic rocks: did mid-ocean ridges and island arcs exist during this time? Understanding these origins enables the comparison of Precambrian igneous rocks to their tectonic setting.

Amphibolite blocks: Amphibolite blocks are generally observed in the field as large blocks, and are commonly associated with quartzite. Whole rock geochemistry shows that most of the amphibolites are low in titanium and iron. Ti-V plots are a measure of oxygen activity in magma, and are also a measure of crystal fractionation. Titanium and vanadium are immobile elements and are thus not highly affected by hydrothermal alteration and metamorphic events (Shervais, 1982). A Ti *vs.* V plot shows that the amphibolites have a ratio of 15-50, and thus are not arc-related "wet" melts (Fig 4-1). Low oxygen fugacity in the mantle also supports that these melts were not hydrated. The trends from the Ti-V plots seem to point towards a MORB or OIB trend, and suggest fractionation along an olivine-and plagioclase-rich liquid. It should be noted, however, that Ti-V plots were not tested for komatiitic rocks (Shervais, pers.

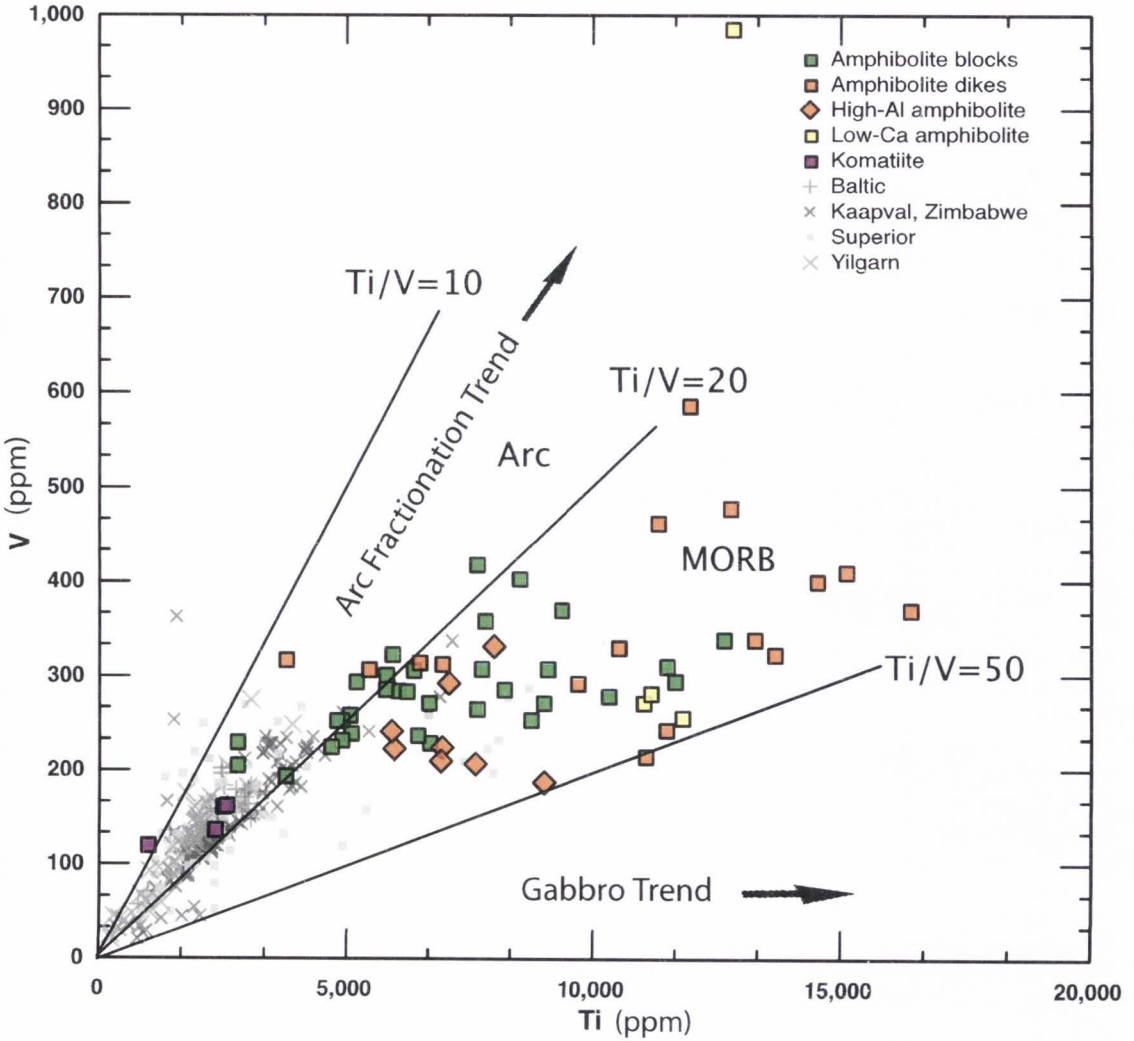

Figure 4-1. Ti vs V plot of the FCC komatiites and amphibolites with Archean komatiites for comparison.

comm., 2005), but they do seem to fit other discrimination diagrams and have therefore been considered as applicable in this study. These trends also may indicate radical amounts of melting. Chondrite-normalized REE plots show that the amphibolite blocks are relatively flat, and are only slightly enriched in LREEs (Fig 3-14). Multi-element (spider) diagrams normalized to primitive mantle show that the amphibolite blocks are low in high field strength elements and show a negative thorium anomaly relative to primitive mantle, indicating a non-arc source (Fig 3-17). Most of the amphibolite blocks lie along a fractionation trend of komatiites. If these form due to fractionation of komatiites, which require a high percentage of partial melting, then trace element patterns should be the same as the source.

Amphibolite dikes: Amphibolite dikes in gneiss and chert are high in titanium, iron, and HFSEs. A chondrite-normalized REE plot shows a very slight slope, which is similar to the amphibolite blocks; however, there is a slightly greater abundance of initial concentrations (Fig 3-15). A spider diagram normalized to primitive mantle shows that these dikes are higher in HFSE relative to primitive mantle than the amphibolite blocks (Fig 3-18). These dikes also have a negative thorium anomaly, but have a very large negative strontium anomaly indicating a non-arc source. This negative strontium anomaly can be attributed to residual plagioclase in the source, most likely due to shallow melting of the oceanic crust. The amphibolite dikes do not lie along the fractionation trend of the komatiites. Higher concentrations of HFSEs and other incompatible elements mean that they were either derived from a more enriched source

such as a mantle plume like Hawaii, or smaller percentages of melting from a possibly older amphibolite with residual plagioclase.

High-Al amphibolites: The high-Al amphibolites are mostly dikes that have Al_2O_3 amounts that are similar to cumulate gabbros (20-30% Al_2O_3) and most also have low CaO compared to normal amphibolites (Fig 3-8 and 3-9). Chondrite-normalized REE's in the high-Al amphibolites are relatively the same as the other amphibolites (Fig 3-16). Spider diagrams of the high-Al amphibolites, however, show that there is no positive europium or strontium anomalies such as are expected in plagioclase cumulates (Fig 3-19). Also of note is the large spike in uranium as well as compatible elements. These amphibolites appear to be representative of hydrothermally altered lithologies, as shown by the low CaO and positive spikes in water-mobile elements. This alteration could be a result of sea-floor hydrothermal alteration, or a later metasomatic event.

Low-calcium amphibolites: Low-calcium amphibolites also show geochemical signatures of sea-floor alteration, which commonly lowers Ca, and increases Na and K (Fig 3-9 through 3-11). The hydrothermal alterations, as found in the aluminum-rich amphibolites, are problematic, in that the original lithology is obscured. The generally high Ti and Fe, and the REE patterns, are consistent with their origin as amphibolite dikes.

Komatiites: The ultramafic lenses of the FCC have compositions that closely resemble komatiites and are distinct from harzburgites: they are too high in Al and Ca, and too low in Mg to represent refractory mantle material or even fertile lherzolites. Ultramafic rocks of the FCC clearly lie along the trend of known Archean komatiites

from around the world, and are associated with amphibolites (metabasalts) and quartzites (metacherts) in single tectonic blocks – an association not found in mantle harzburgite blocks in modern accretionary complexes or on the modern seafloor.

Petrogenesis: The amphibolites, with the exception of the high-aluminum and low-calcium amphibolites, have TiO_2-(CaO/TiO_2) and TiO_2-(Al_2O_3/TiO_2) systematics similar to oceanic basalts, including MORB and ocean island basalts (Fig 3-20 through 3-22); that is, they are not more depleted than MORB with respect to titanium. This means that they are not related to boninites, the ultra-depleted high-Mg andesites commonly associated with island arc terranes. TiO_2-(CaO/TiO_2) and TiO_2-(Al_2O_3/TiO_2) relations for the high-aluminum and low-calcium amphibolites show that there has most likely been pre-metamorphic alteration of these amphibolites (Fig 3-20 through 3-22).

Trace element discrimination plots such as Ti-V, Zr-Zr/Y, Cr-Y, and Ti-Zr discrimination diagrams (after Pearce and Cann, 1973; Shervais, 1982) can aid in distinguishing the amphibolites of MORB, island arc tholeiite, and calc-alkaline affinities. Ti-V (Fig 4-1) and Ti-Zr (Fig 4-2) discrimination diagrams show that the tholeiitic amphibolite knockers and dikes are dominantly in the MORB field, while some remain in the arc field. The majority of the FCC komatiites fall in the lower part of the arc field along with other Archean komatiites. The amphibolites also show what appears to be a melting curve on the Ti-V discrimination diagram. Fig 4-3 shows a Th-Hf-Ta discrimination diagram (Wood, 1980) and indicates that most of the amphibolites appear to fall outside the outlined fields, except for a few that are in the alkaline within-plate

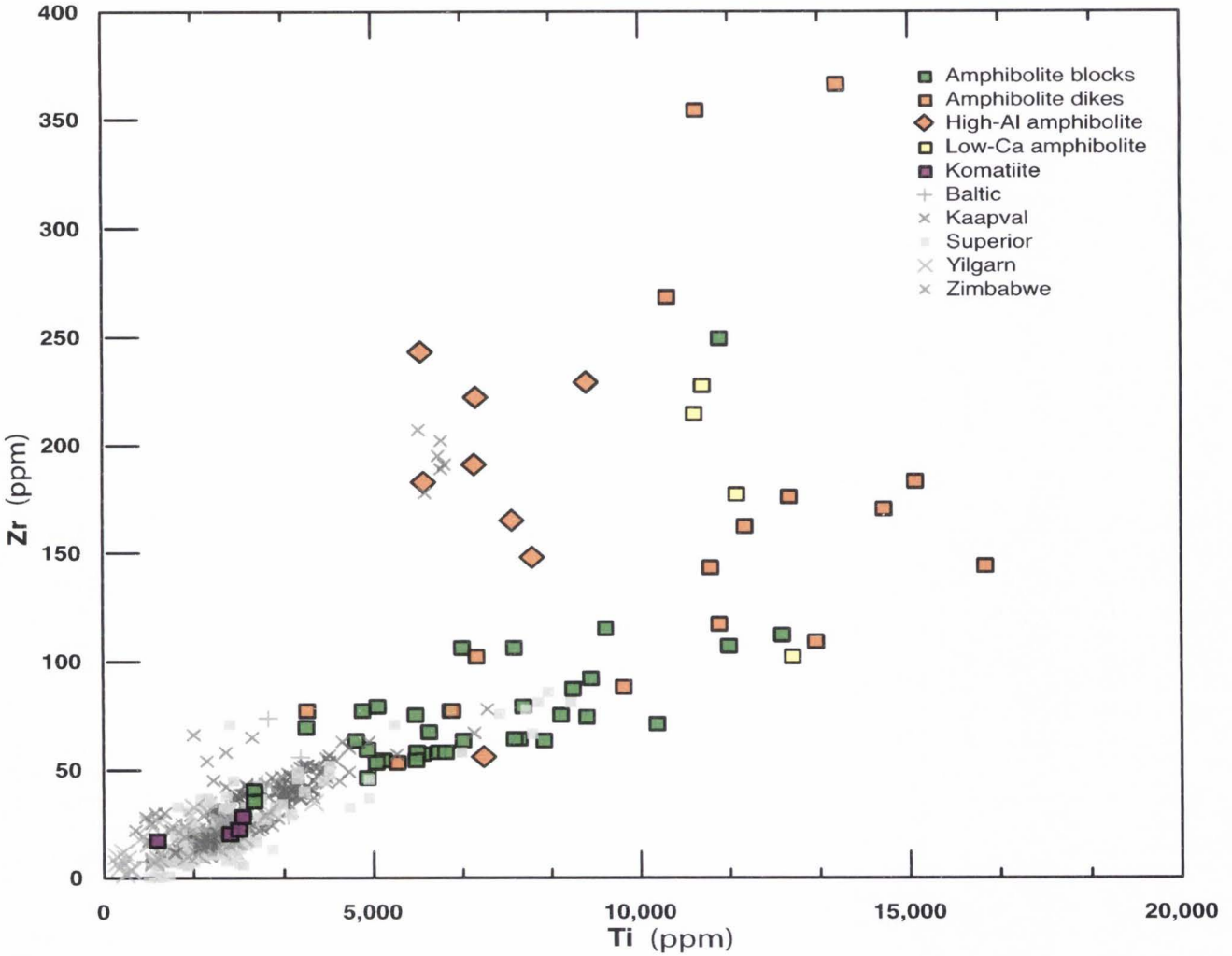

Figure 4-2. Ti vs Zr plot of the FCC komatiites and amphibolites with Archean komatiites for comparison.

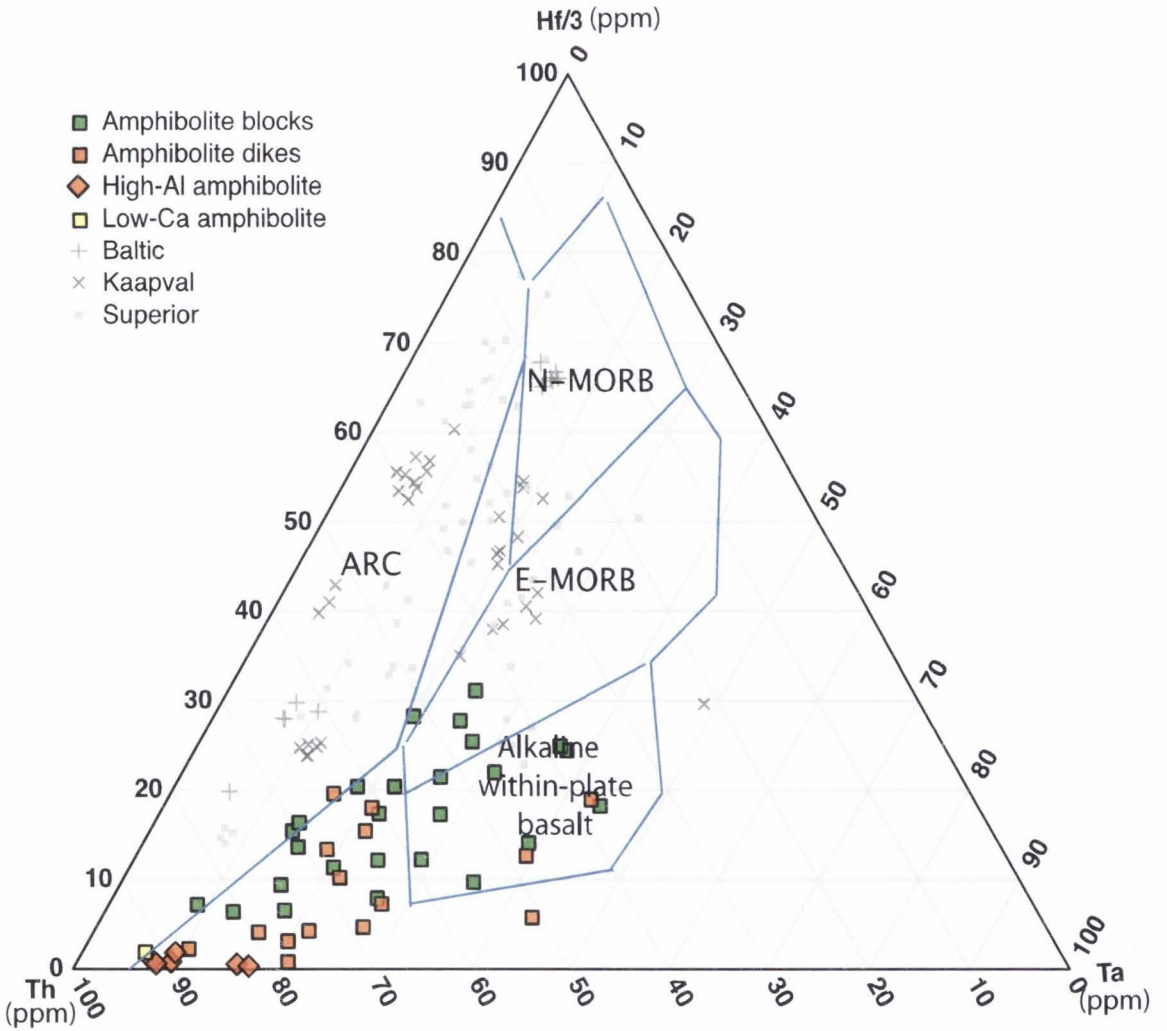

Figure 4-3. Th vs Hf/3 vs Ta plot for the FCC amphibolites, with Archean komatiites for comparison (after Wood, 1980).

basalt field. This may be due to limited data used in Wood (1980) or may reflect distinct mantle composition during the Archean.

All of the amphibolites are LREE-enriched and have REE concentrations that are greater than that of MORB which suggests a more evolved source. The amphibolite blocks have La concentrations that are 8x to 30x MORB, while the amphibolite dikes have La concentrations that are 9x to 90x MORB. The REE chemistry does not point toward a MORB source, but is characteristic of ocean island basalt (OIB). Fig 4-4 shows a spider diagram of a melting model based on an EMORB composition source with a spinel-lherzolite mode (indicating melting at pressures below ≈9 Kb). This diagram shows similar results for both the amphibolite blocks and the amphibolite dikes, and indicates that these amphibolites were probably derived from an enriched source similar to the E-MORB source composition by moderate to high degrees of partial melting (10% to 40%). An important point to note is that the slight LREE-enriched slopes of the amphibolite blocks must reflect a similar enrichment in their mantle source region (Fig 3-14). This means that, by the late Archean when their parent magmas formed, the Earth's mantle was already differentiated and parts of it were significantly more enriched in incompatible elements than primitive mantle.

Quartzites (Metachert)

There are four main hypotheses for the interpretation of the FCC quartzites/metacherts: (1) they are quartz-rich sands thatwere deposited on a passive continental margin, (2) they are hydrothermal cherts precipitated from submarine hot springs on or near an ocean spreading center, (3) they derived from microbial mats

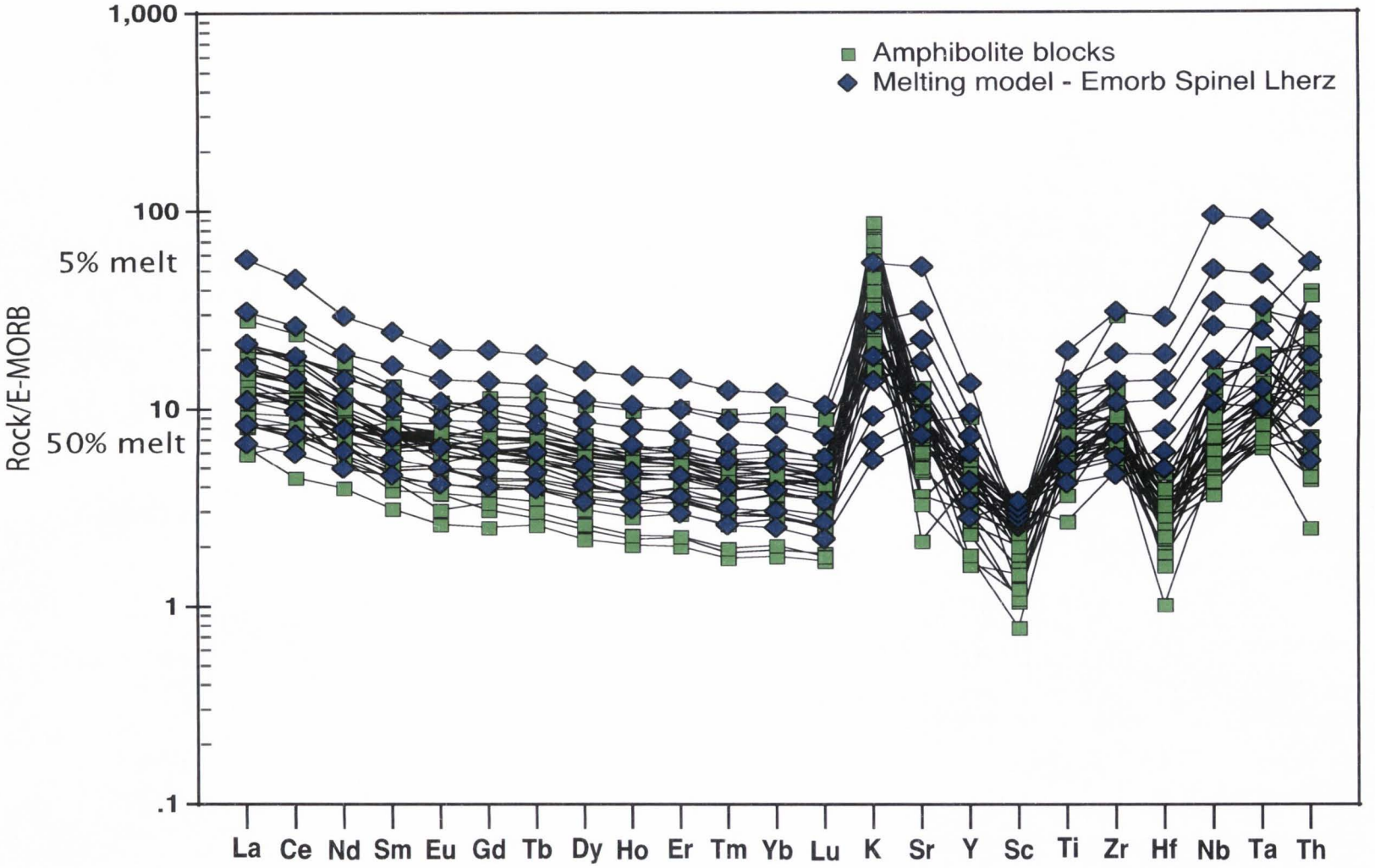

Figure 4-4. E-MORB normalized Spider diagram melting model using a Spinel Llehrzolite mode with 5-50% melting, compared with the FCC amphibolite blocks.

deposited on the seafloor (possibly near hot springs), or (4) they are silicified tuffs formed diagentically by the circulation of low fO_2 seawater that was saturated with silica in solution.

Based on geochemistry, the cherts can be divided into two groups: cherts that are slightly LREE-enriched relative to North American shale, and cherts that are slightly LREE-depleted relative to North American shale. None of the cherts show relict textures that reflect clastic sedimentation. In contrast, the faint color changes that reflect original bedding are commonly seen in Archean cherts of known provenance such as those found in the Sudros. The common association of "quartzite" with amphibolite, and the occurrence of later amphibolite dikes that cross-cut the quartzites, also argue against a passive margin depositional setting.

Fig 3-23 (SiO_2 vs Al_2O_3) and (SiO_2 vs K_2O) show that most FCC cherts fall along a mixing trend between pure silica and clay (illite or illite plus kaolinite seem to be the clay components along this mixing line). An interesting observation is that the schist partings between thinly bedded quartzites fall along a mixing line towards the clay end members. This suggests that these "quartzites" could possibly be actually cherts that formed as silicified ash beds such as those found in the Barberton greenstone belt (Lowe and Byerly, 1999) and the Swaziland Supergroup (Lowe, 1999; Knauth and Lowe, 2003). This trend does not rule out the possibility that these are quartzites derived from a sandstone source. The chemistry of the quartzites seem to support a range between a felsic to a more mafic ash character. Fig 3-25 (MgO vs FeO* vs Al_2O_3) shows a trend from clay to hydrothermal components. Some of the clays, which are rich in potassium

and aluminum, are now present as fuchsite (Cr-rich mica). The quartzites which are rich in chromium, nickel and cobalt can best be explained as chrome-rich ash layers from a mafic amphibolite or komatiite source, as opposed to a silica rich tuff.

In contrast, the ironstone appears to be influenced by a hydrothermal component rich in Fe that is unrelated to the clay mixing trend. SiO_2 vs FeO* (Fig 3-24) also emulates these same properties, showing the FCC quartzites along a clay mixing line. This figure shows that the ironstone has hydrothermal attributes.

There is no currently accepted way to infer whether microbial activity was important in the formation of these metacherts due to their high-grade of metamorphism. Based on analogies with unmetamorphosed Archean cherts, it seems likely that microbial activity may have been important, even in cases where the primary control was hydrothermal discharge or silicified ash.

The most likely interpretation is that the FCC quartzites were originally microbial chert beds that were inundated with ash, which was derived from komatiite basalt or ash and possibly other ash-rich eruptions. These were silicified shortly after deposition as seawater circulated through the sediment pile, much like the Barberton cherts (Lowe, 1999). It has been shown that Archean seawater had much higher dissolved silica content than modern seawater due to its low oxygen content, which inhibited the abiogenic precipitation of silica at or just below the sea-bed (Maliva et al., 2005). This would suggest that silica was primarily deposited by replacement.

Granite/Pegmatite

The granite pegmatites are clearly intrusive igneous rocks that formed after the main phase of metamorphism and deformation, but were intruded before deformation ceased. Chondrite-normalized REE patterns (Fig 3-33) for the granite pegmatites show positive europium anomalies that increase in size with decreasing total REE content, which indicates plagioclase accumulation. Pearce et al. (1984) derived several empirical discrimination diagrams to tell in which tectonic setting granites may have formed. Figs 4-5 (Nb-Y), 4-6 (Ta-Y), 4-7 (Rb-Y+Nb), and 4-8 (Rb-Yb+Ta) show that the FCC pegmatites and granites have volcanic arc and syn-collisional properties and attributes. One thing to note in these diagrams is the use of rubidium. Rubidium is a very mobile element in hydrothermal fluids, but is used based on the assumption that granites are not very easily altered and have lower elemental mobilities (Pearce et al., 1984; Harris et al., 1986). It is also evident that the granites are not altered or even metamorphosed. These plots are not effective in distinguishing post-orogenic granites as well as supra-subduction, fore-arc basin granites, which are an ocean-ridge type granite. To be able to distinguish these types of granites, Harris et al. (1986) showed that it is necessary to use Hf-Rb/30-Ta x 3 diagrams, which indicate that the FCC granites are syn-collisional, and volcanic arc granites (Fig 4-9). This evidence is also fortified by Fig 4-10 (Hf-Rb/10-Ta x 3) after Harris et al. (1986) that shows the FCC granites lie along a volcanic arc trend of a collisional tectonic setting.

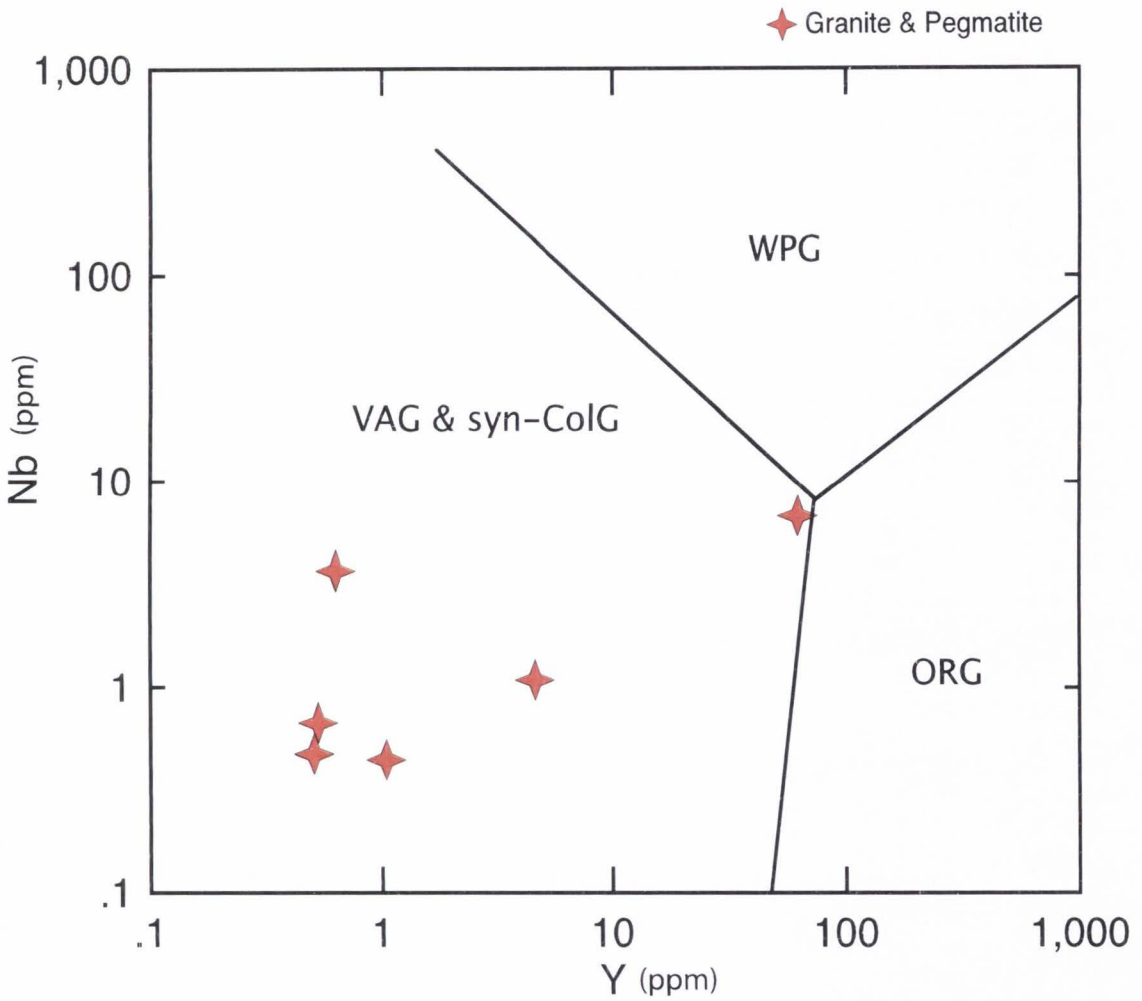

Figure 4-5. Nb vs Y plot for the FCC granites (after Pearce et al., 1984).

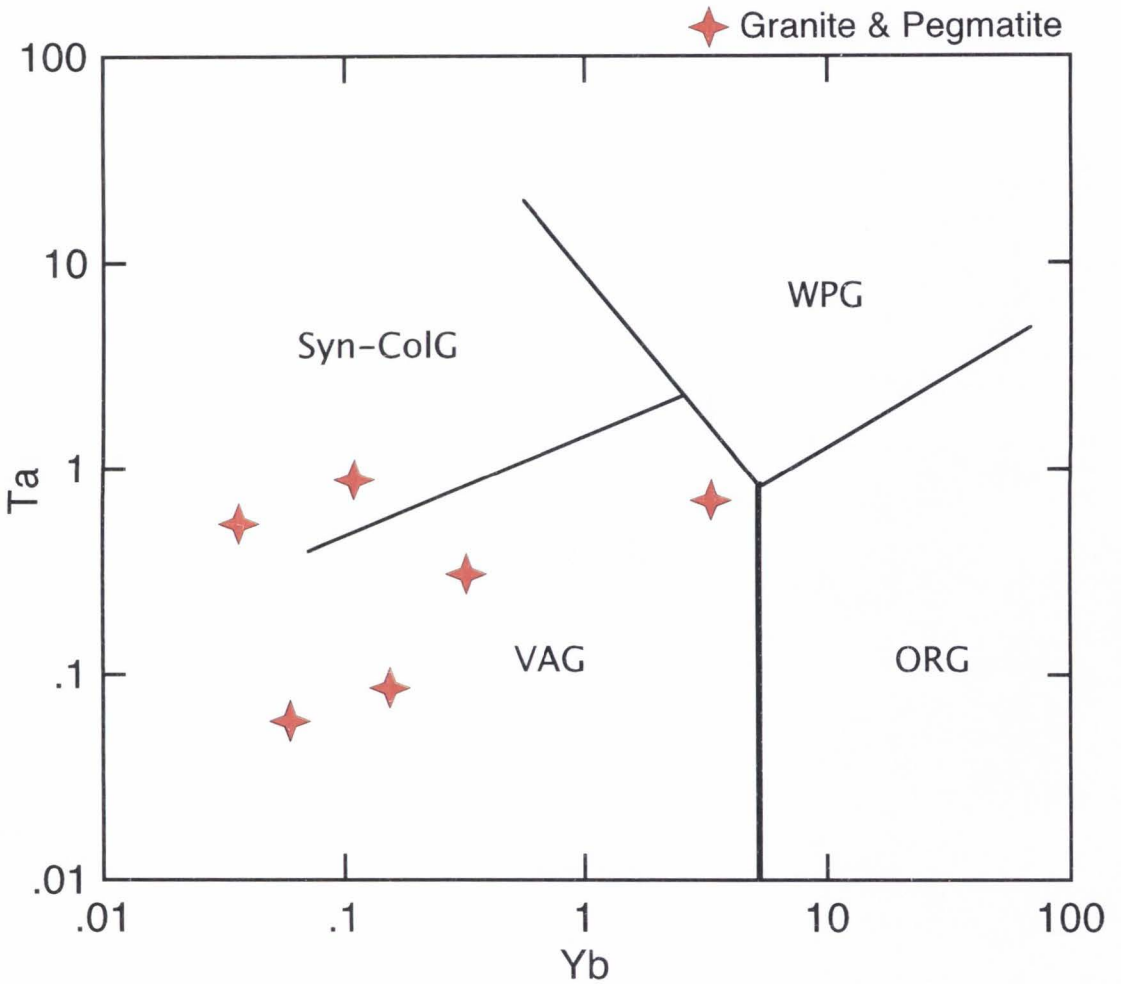

Figure 4-6. Ta vs Yb plot for the FCC granites (after Pearce et al., 1984).

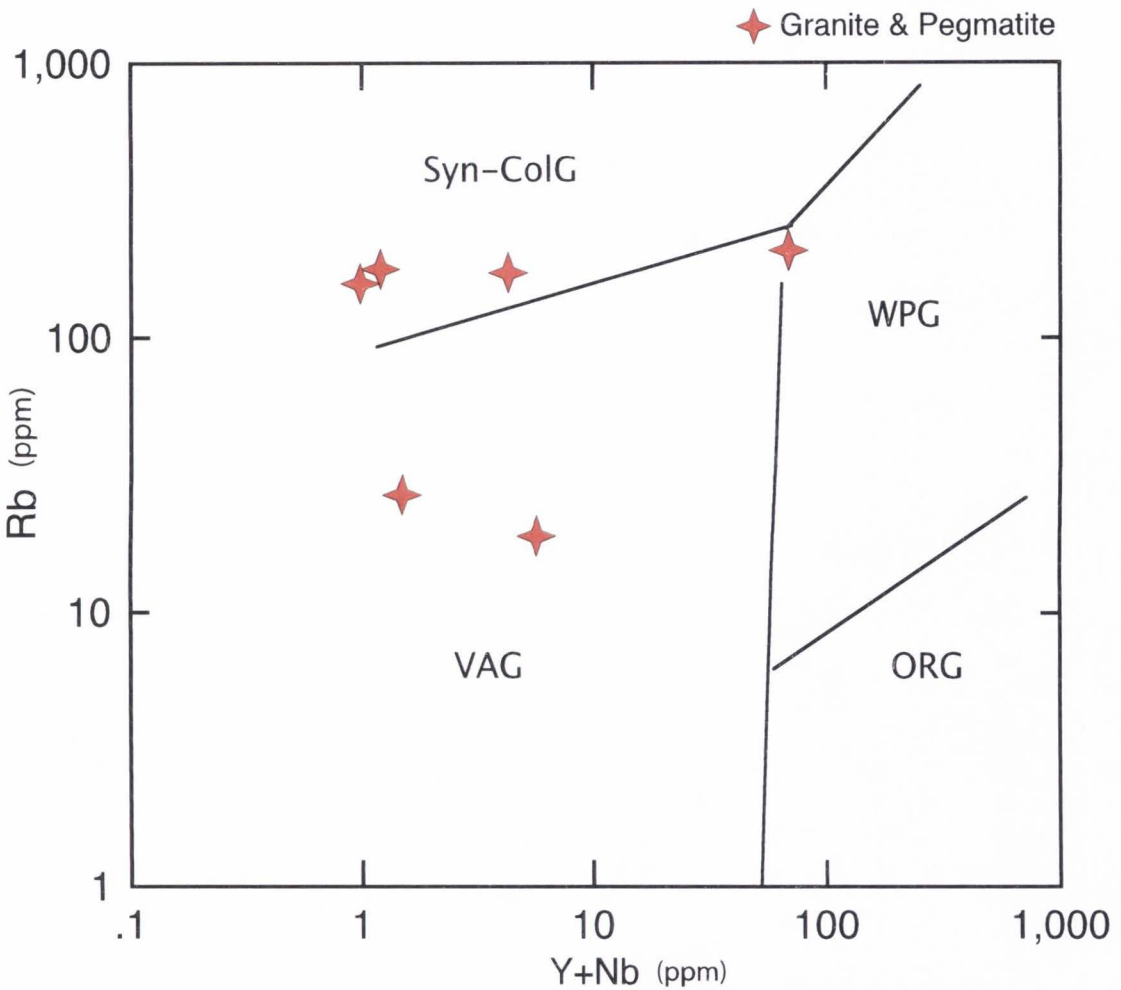

Figure 4-7. Rb vs Y+Nb plot for the FCC granites (after Pearce et al., 1984).

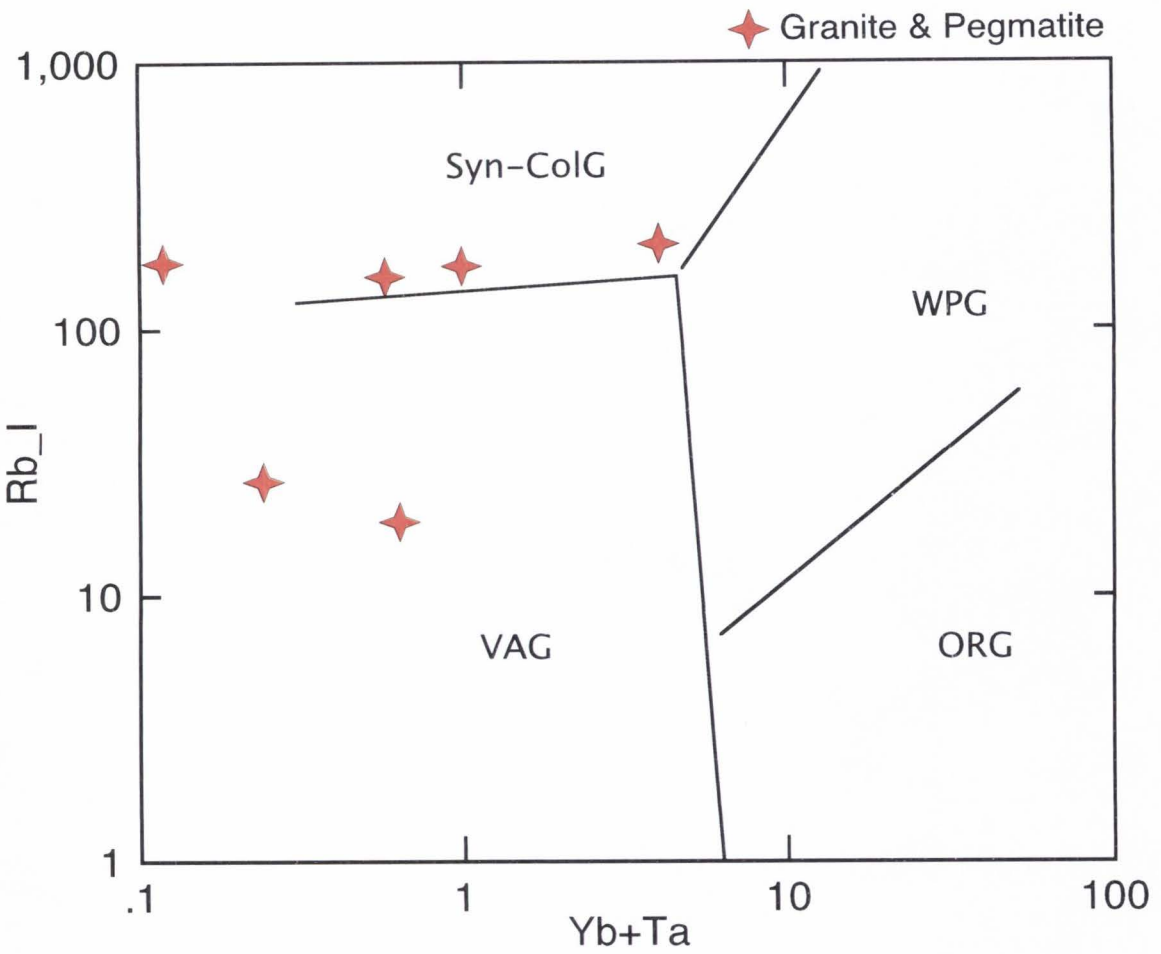

Figure 4-8. Rb vs Yb+Ta plot of the FCC granites (after Pearce et al., 1984).

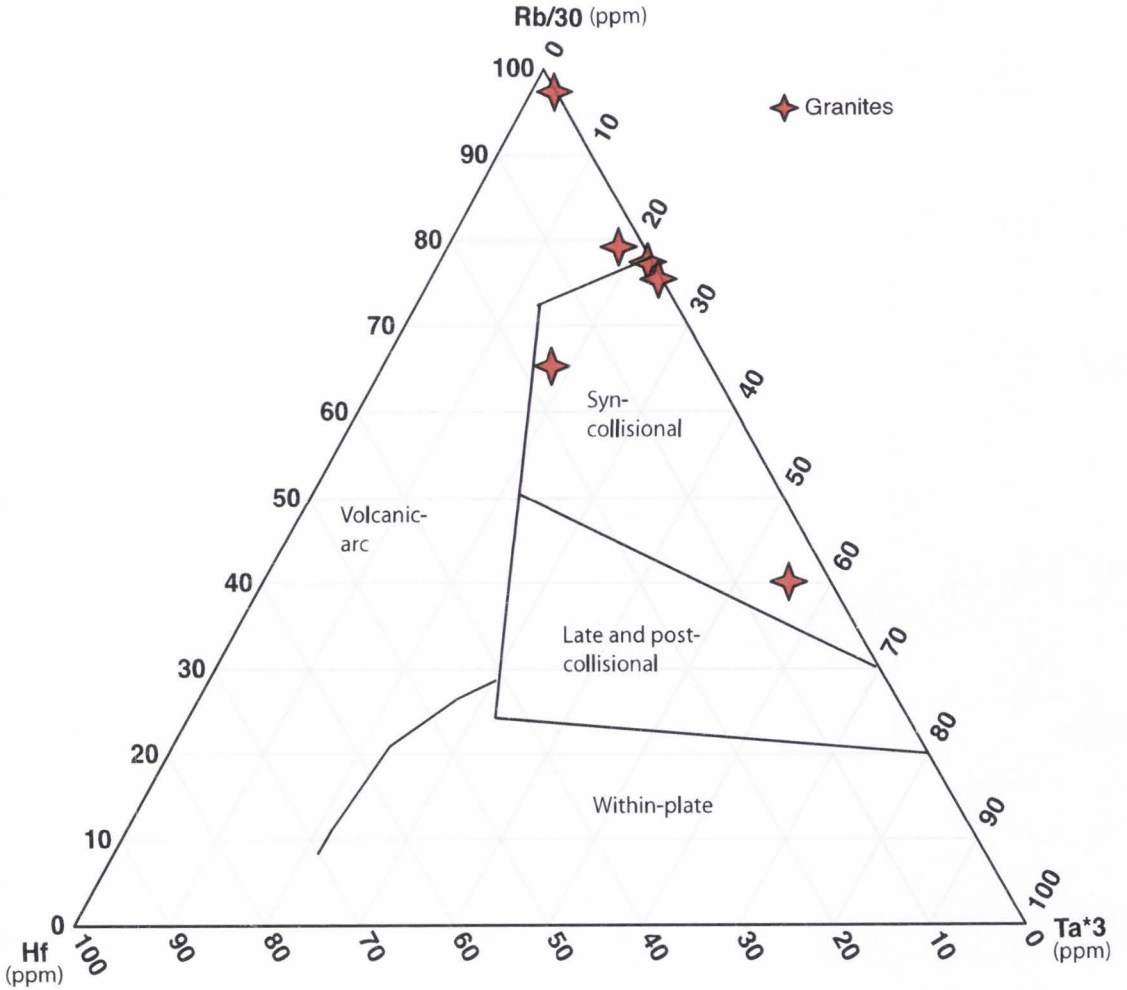

Figure 4-9. Hf vs Rb/30 vs Ta*3 ternary diagram of the FCC granites (after Harris, 1986).

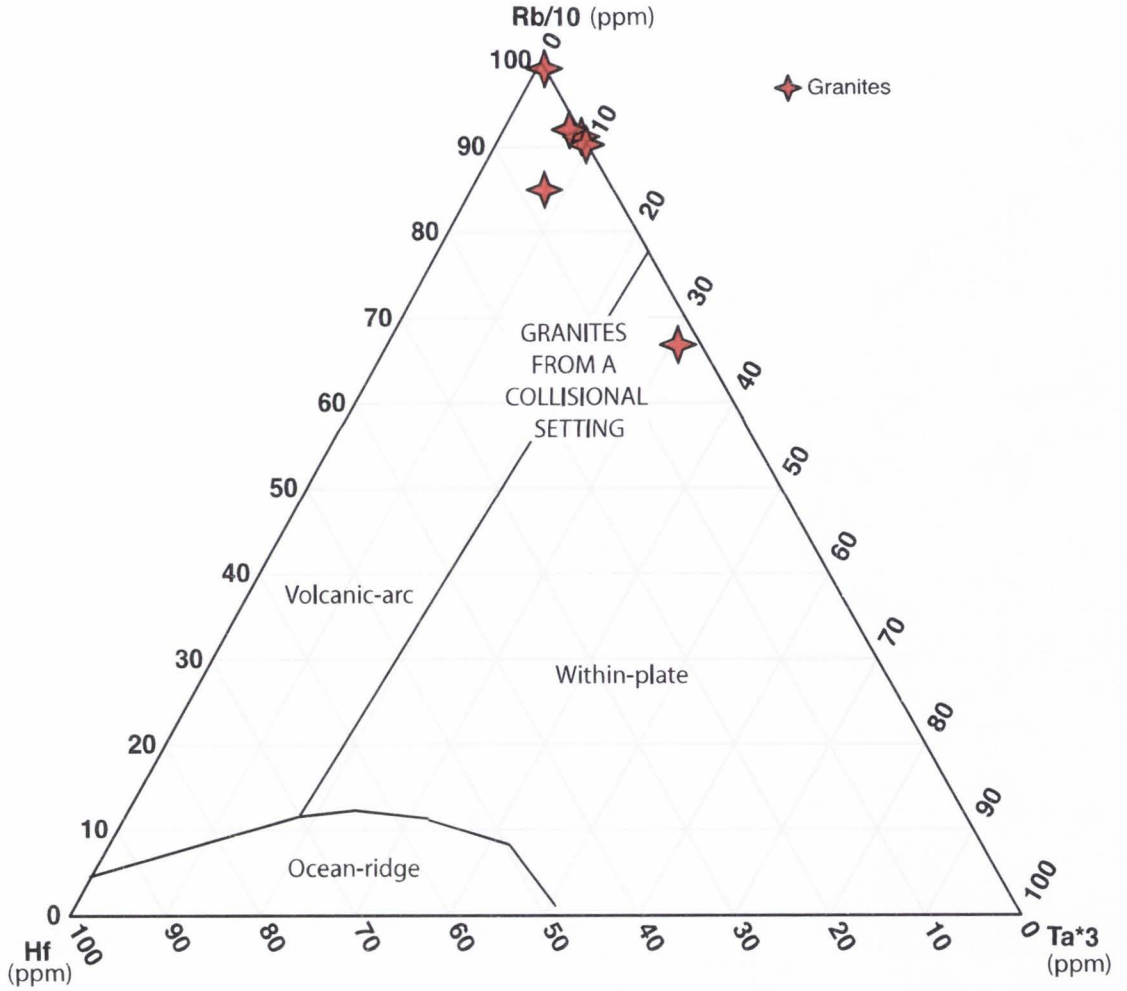

Figure 4-10. Hf vs Rb/10 vs Ta*3 ternary of the FCC granites (after Harris et al., 1986).

CHAPTER 5

CONCLUSIONS

Origin of the Farmington Canyon Complex

There are four main hypothesis for the origin of the Farmington Canyon Complex that we will consider here: (1) the FCC represents a passive continental margin succession, (2) the FCC represents an intra-continental rift basin succession, (3) the FCC represents a Precambrian accretionary complex associated with subduction along the margin of the Wyoming craton, and (4) the FCC represents a greenstone belt which has undergone extensive faulting. In all cases, the FCC must have undergone significant metamorphism and deformation under amphibolite grade conditions *circa* 1800 Ma.

The association of mafic volcanic rocks with passive margin sequences is a relict of its earlier stage of rifting to form an ocean basin; after rifting occurs there is little or no volcanic activity associated with passive margins. This makes the early rifting phase essentially the same as an intra-cratonic rift basin, so we will consider both together in our discussion. The higher amount of quartzo-feldspathic gneiss could be attributed to rifting, and the possibility that there is some rifting activity should not be entirely ruled out. Earlier studies have supported this theory (Bell, 1951,1952; Bruhn and Beck, 1981; Bryant, 1988a,b), but there are inconsistencies, such as the presence of ultramafic assemblages including komatiites and other chemical characteristics, that cannot be explained for the previously interpreted tectonic setting. This does not explain the granites with volcanic arc/syn collisional properties. Foster et al. (2006) proposed that the FCC could be an intracratonic rift of the Wyoming province, that did not progress

significantly. Another theory is, that the Grouse Creek block was accreted to Wyoming in the Paleoproterozoic, however, it is unclear at depth as to how the Wyoming province is related to the Grouse creek block (Foster et al. 2006).

The possibility that the FCC represents a Precambrian accretionary complex associated with subduction along the margin of the Wyoming craton has been discussed by Shervais (2006). He notes the following characteristics that support this interpretation: (1) rock assemblages consisting of oceanic crust or ophiolites, (2) island arc volcanic or plutonic rock suites, or (3) accretionary complexes formed in asymmetric subduction zones. These assemblages are based on Phanerozoic examples, and it is important to keep in mind that high heat flow in the Archean coupled with Hadean-style convection, could produce rock assemblages which are similar to oceanic crust.

Studies have shown that subduction centers have a tendency to initiate along preexisting oceanic fracture zones (e.g. Casey and Dewey, 1984). These convergent suture zones tend to parallel ancient convergent zones, and ancient backarc oceanic crust would be trapped within the overriding oceanic plate. The entrapped oceanic crust would then become the base on which magmatism and subsequent sedimentation would occur (Saleeby, 1979; Scholl et al., 1986; Kusky, 1998 ;de Wit, 1998, 2004; Polat and Kerrich, 2001, 2002; Wyman and Kerrich, 2002). This has been documented locally by the discovery of oceanic crust fragments in the northern Colorado Front Range. These fragments were formed prior to 1.7 Ga and were emplaced in an arc magmatic event between 1.8 -1.7 Ga. This event along with the accompanying sedimentation was important for the growth and formation of continental crust for the Colorado province

(Cavoise and Selverstone, 2003). The timing of this event, of the Santaquin arc, and the emplacement of the FCC pegmatites and granites suggests that they are connected to each other in a regional tectonic event. Garnet porphyroblasts (high pressure/high temperature) in amphibolite, such as shown in Fig 2-7 photo F, are commonly rimmed by plagioclase, hornblende (±pyroxene) symplectites (low pressure/high temperature) implying a clockwise pressure-temperature-time (PTt) path. This and other evidence previously discussed, gives reasonable evidence that there was a convergent margin along the margin of the Wyoming province as continental crust was incrementally added. The isolated blocks or slabs of mafic and ultramafic metavolcanics give credence to the possibility that they are oceanic and island-arc-derived material.

The FCC quartzites in the southern part of the complex may represent metachert, and not epiclastic quartzite (Shervais, 2004). High Cr and Ni content in many of these layers gives evidence of volcanic input and has been discussed previously as komatiitic ash. Comparison of Cr and Ni content in quartz sandstones would be helpful to ascertain whether or not this occurrence is an exclusive component. The Cr-rich fuchsite mica mimics bedding in many of the quartzites. Some outcrops have 5-20 cm thick beds of quartzite intercalated with 1-2 cm thick schist layers, which suggests a compositionally banded chert protolith. The FCC quartzites are also commonly found in blocks with ultramafic and mafic assemblages. There could be minor influences from later deformation, but the blocks have very wide ranges in foliations compared to the surrounding schist and gneiss. This relation fortifies the notion of being mélange related.

This suggests a sedimentary basin with oceanic crust or sills that were intruded off-axis (e.g.. Shervais and Kimbrough, 1987).

The FCC migmatitic gneisses have chemical compositions similar to greywacke (Bryant, 1988a,b), which is consistent with Franciscan-style mélange matrix with minor differences in appearance only (Shervais, 2006). These gneisses are associated with amphibolites and have been strongly deformed in the northern part of the complex, and are crosscut by younger amphibolitic dikes and undeformed granite pegmatites. These pegmatites are much younger and represent anatectic melting from emplacement at 1790-1800 Ma (Bryant, 1988a). The association of these granites, which have island arc/syn-collisional properties, supports the theory of an arc, or active margin sequence nearby. The formation of the FCC as an accretionary complex is still permitted within the time constraints given by previous investigations. Collision and metamorphism at ~1800 Ma would obscure the basinal record and therefore make interpretation problematic.

There is another possibility we have not considered yet: whether the FCC represents a greenstone belt that has undergone extensive deformation and metamorphism. In this case, the layered gneisses would represent the ancient "grey gneisses" that are commonly associated with greenstone belts and form the substrate that they were either deposited on (e.g., Hamilton, 1998) or thrust onto (de Wit, 1998). All of the rocks found in the FCC are also similarly associated in typical Archean greenstone belts, although the proportion of chert to amphibolite is much higher in the FCC. In addition, many of the FCC quartzo-feldspathic gneisses have compositions broadly

similar to the tonalitic ancient grey gneisses that underlie most greenstone belts. However, the banding common in the FCC quartzo-feldspathic gneisses is more characteristic of paragneiss derived from metasediments than the grey gneisses, which tend to be massive and lack compositional banding. In some parts of the FCC, orthogneisses with abundant plagioclase can be found with distinct compositional banding. These gneisses could possibly derive from passive-margin or arc related sediments that could pre-date the collision of an arc-terrane with other terranes and/or the margin of the Wyoming province. Foster et al. (2006) also suggest that the sediments from the protogneiss may have derived from intracratonic rifting in the Paleoproterozoic. This short-lived rifting event may explain the high proportions of gneiss and schist in the FCC. Archean tonalite-trondhjemite-granodiorite (TTG) gneiss complexes have been correlated with plutonic series formed in island-arc settings due to slab melting (Drummond and Defant, 1990; Rapp et al., 2003). With nearby arcs, there would be an influx of volcanic ash and material that would account for their presence in the sediments as well as the chert/quartzites. Some authors have argued that Archean greenstone belts represent coeval island arc volcanic rocks (e.g., Parman et al., 2001,2004; Polat and Kerrich 2001, 2002, 2004; Grove and Parman, 2004; Parman and Grove, 2004). Komatiitic ashes also appear to have been incorporated in many of the quartzites as evidenced by the high chromium and nickel content. Many of the quartzo-feldspathic gneisses contain mafic and felsic ashes, as reported by Bryant (1988a) in his discussion of protolith. Studies in the western Pacific have shown a progression of ultramafic to felsic volcanism within greenstone belts (e.g., Hawkins et al., 1984).

The pegmatitic granites are younger than the gneisses and tonalitic granites and were emplaced between 1790-1800 Ma during the last significant metamorphic event of the FCC. This event is coincident with the accretion of the Santaquin arc as well as the northern Colorado Front range as previously discussed. It seems that this was a period of terrane accretion and that it possibly could be the accretion of a greenstone belt with an island arc. This evidence is also consistent with the 1800 Ma collision zone of the Cheyenne belt of the Wyoming province (Chamberlain et al., 1993). The proto-gneissic sediments could have then been added to by sediment influx from surrounding highlands or have been mixed in a mélange style accretionary wedge.

Based on the data currently available, model #3 or model #4 is favored, or possibly a mixture of the two. It has been proposed that Archean greenstone belts represent primitive island arc terranes (Grove et al., 1999; Parman et al., 2001; Parman and Grove 2004). Based on the findings of this investigation, the FCC would also fit well with the constraints of this hypothesis. Fig 5-1 shows a final culmination cartoon representing the most likely sequence of events for the FCC.

Further Work

In order to fully understand the origin of the Farmington Canyon complex, further work will be required. Additional work needed includes the following:

Refined age constraints of the different rock suites are needed to better define their temporal relationships. Isotopic compositions of amphibolites and gneisses, and mineral compositions and P-T-time calculations based on relict mineral assemblages need to be performed. More detailed studies of cherts of the FCC need to be carried out

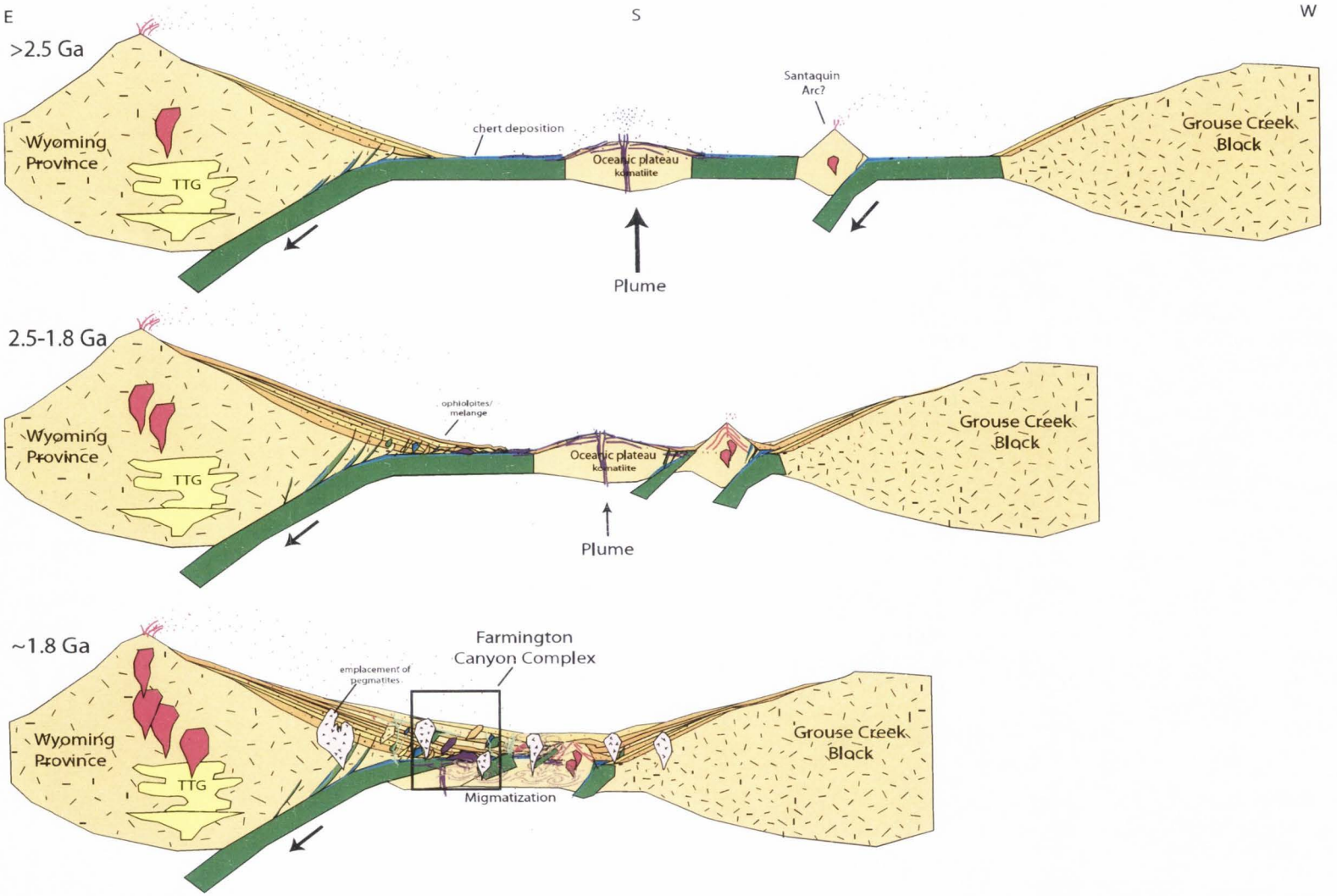

Figure 5-1. Final culmination cartoon representing the most likely sequenc of events for the FCC during the precambrian.

in order to better understand their petrogenesis. Additionally, more major and trace element data of known Archean cherts are needed for better comparison with the FCC cherts.

Understanding the enigmatic Archean processes, as well as deciphering the evolution of Archean rocks is quite a challenge. Much work has been done to further research in this area. There is much speculation and little agreement on tectonic processes and timing in the Archean; however, great advancements have been made, and many more will undoubtedly be made in the future.

REFERENCES

Barnett, D., Bowman, J.R., and Smith, H.A., 1993, Petrologic and geochronologic studies in the Farmington Canyon Complex, Wasatch Mountains and Antelope Island, Utah: Utah Geological and Mineral Survey, Contract Report CR-93-5, p. 34.

Bell, G.L., 1951, Farmington Complex of the north-central Wasatch: Ph.D. thesis Salt Lake City, University of Utah, , 101 p.

Bell, G.L., 1952, Geology of the northern Farmington Mountains, *in* Marsell, R.E., ed., Geology of the central Wasatch Mountains: Utah Geological Society Guidebook to the Geology of Utah, no. 8, p. 38-51.

Bercovici, D., 2003, The generation of plate tectonics from mantle convection: Earth and Planetary Science Letters, v. 205, p. 107-121.

Bruhn,R.L., and Beck, S.L., 1981, Mechanics of thrust faulting in crystalline basement, Sevier orogenic belt, Utah: Geology, v. 9, no. 5, p. 200-204.

Bryant, B., 1988a, Geology of the Farmington Canyon Complex, Wasatch Mountains, Utah: U.S. Geological Survey Professional Paper 1476, 54 p.

Bryant, B., 1988b, Evolution and early Proterozoic history of the margin of the Archean continent in Utah, in Ernst, W. G., ed., Metamorphism and crustal evolution of the Western United States. Rubey Volume vii; Englewood Cliffs, New Jersey, Prentice Hall, p. 431-445.

Calvert, A.J., and Ludden, J.N., 1999, Archean continental assembly in the southeastern Superior province of Canada: Tectonics, v. 18, no. 3, p. 412-429.

Casey, J.F., and Dewey, J.F., 1984, Initiation of subduction zones along transform and accreting plate boundaries, triple-junctions evolution, and forearc spreading centers-Implications for ophiolitic geology and obduction, *in* Glass, I.G., et al., eds., Ophiolites and Oceanic Lithosphere: Geological Society Special Publication, 13, p. 269-290.

Cavoise, A., and Selverstone, J., 2003, Early Proterozoic ocean crust in the northern Colorado Front Range: Implications for crustal growth and initiation of basement faults: Tectonics, v. 22, no. 2, p. 1015-1035.

Chamberlain, K.R., Patel, S.C., Frost, B.R., and Snyder, G.L., 1993, Thick-skinned deformation of the Archean Wyoming province during Proterozoic arc-continent collision: Geology, v. 21, p. 995-998.

Chappel, B.W., and White, A.I.R., 1974, Two contrasting granite types: Pacific Geology, p. 173-174.

Christie-Blick, N., 1997, Neoproterozoic sedimentation and tectonics in west-central Utah, *in* Link, P.K., Kowallis, B.J., (editors), *Proterozoic to Recent stratigraphy, tectonics, and volcanology, Utah, Nevada, southern Idaho, and central Mexico*: Brigham Young University Geology Studies, v. 42, part I, p. 1-30.

Compton, R.R., 1972, Geologic map of the Yost quadrangle, Box Elder County, Utah and Cassia County, Idaho: US Geological Survey Miscellaneous Geologic Investigations Map I-672, 1:31,680.

Compton, R.R., 1975, Geologic map of the Park Valley quadrangle, Box Elder County, Utah and Cassia County, Idaho: US Geological Survey Miscellaneous Geologic Investigations Map I-873, 1:31,680.

Compton, R.R., 1980, Fabrics and strains in quartzites of a metamorphic core complex, Raft River Mountains, Utah: Geological Society of America Memoir 153, p. 385–398.

Compton, R.R., Todd, V. R., Zartman, R. E., and Naeser, C. W., 1977, Oligocene and Miocene metamorphism, folding, and low-angle faulting in northwestern Utah: Geological Society of America Bulletin, v. 88, p. 1237–1250.

Condie, K.C., Lee, D., and Farmer, G.L., 2001, Tectonic setting and provenance of the Neoproterozoic Uinta Mountain and Big Cottonwood groups, northern Utah: constraints from geochemistry, Nd Isotopes, and detrital modes: Sedimentary Geology, v. 141-142, p. 443-464.

Connelly, J.N., Ryan, B., 1996, Late Archean evolution of the Nain province, Nain, Labrador: imprint of a collision: Canadian Journal of Earth Sciences, v. 33, no. 9, p. 1325-1342.

Cox, K.G., Bell, J.D., and Pankhurst, R.J., 1979, The interpretation of igneous rocks, London, George, Allen, and Unwin, 450 p.

Dasgupta, H.C., Sambasiva Rao, V.V., and Krishna, C., 1998, Chemical environments of deposition of ancient iron- and manganese-rich sediments and cherts: Sedimentary Geology, v. 125, p. 83-98.

Dehler, C.M., Porter, S.M., De Grey, L.D., Sprinkel, D.A., and Brehm, A., 2007, The Neoproterozoic Uinta Mountain Group revisited: A synthesis of recent work on the Red Pine Shale and related undivided clastic strata, northeastern Utah, U.S.A.: SEPM Special Publication 86, p. 151-166.

de Wit, M.J., 1998, On Archean granites, greenstones, cratons and tectonics: Does the evidence demand a verdict?: Precambrian Research, v. 91, no. 1-2, p. 181-226.

de Wit, M.J., 2004, Archean greenstone belts do contain fragments of ophiolites, *in* Kusky, T.M., ed., Precambrian ophiolites and related rocks, Developments in Precambrian Geology, v.13: Amsterdam, Elsevier, p. 599-614.

de Wit, M.J., Roering, C., Hart, R.J., Armstrong, R.A., de Ronde, C.E.J., Green, R.W.E., Tredoux , M., Peberdy, E., and Hart, R.A., 1992, Formation of an Archean continent: Nature, v. 357, p. 553-562.

Dirks, P.H.G.M., and Jelsma, H.A., 1998, Horizontal accretion and stabilization of the Archean Zimbabwe Craton: Geology, v. 26, p. 11-14.

Doelling, H.H., Willis, G.C., Jensen, M.E., Hecker, S., Case, W.F., and Hand, J.S., 1990, Geologic map of Antelope Island, Davis County, Utah: Utah Geological and Mineral Survey Map M -127, 27 pp., 2 pl., scale 1:24,000.

Drummond, M., and Defant, M., 1990, Amodel for trondhjemite-tonalite-dacite genesis and crustal growth via slab melting: Archean to modern comparison: Journal of Geophysical Research, v. 95, no. B13, p. 21,503-21,521.

Ehlers, T.A., Chan, M.A., and Link, P.K., 1997, Proterozoic tidal, glacial, and fluvial sedimentation in Big Cottonwood canyon, Utah, *in* Link, P.K., Kowallis, B.J.,

(editors), Proterozoic to Recent stratigraphy, tectonics, and volcanology, Utah, Nevada, southern Idaho, and central Mexico: Brigham Young University Geology Studies, v. 42, part I, p. 1-30.

Foster, D.A., Mueller, P.A., Mogk, D.W., Wooden, J.L., and Vogl, J.J., 2006, Proterozoic evolution of the western margin of the Wyoming craton: Implications for the tectonic and magmatic evolution of the northern Rocky Mountains: Canadian Journal of Earth Science, v. 43, p. 1601-1619.

Giletti, B.J., and Gast, P.W., 1961, Absoluteage of Precambrian rocks in Wyoming and Montana: New York Academy of Science, Ann. 91, p. 454-470.

Grove, T.L., and Parman, S.W., 2004, Thermal evolution of the Earth as recorded by komatiites: Earth and Planetary Science Letters, v. 219, p. 173-178.

Grove, T.L., Parman, S.W., and Dann, J.C., 1999, Conditions of magma generation for Archean komatiites from the Barberton Mountainland, South Africa, *in* Fei, Y., Bertka, C.M., Mysen, B.O., eds., Mantle petrology: Field observations and high-pressure experimentation; A tribute to Francis R. (Joe) Boyd: Geochemical Society Special Publication 6, p. 155-167.

Hamilton, W.B., 1998, Archean magmatism and deformation were not products of plate tectonics: Precambrian Research, v. 91, no. 1-2, p. 143-179.

Harris, N.B.W., Pearce, J.A., and Tindle, A.G., 1986, Geochemical characteristics of collision-zone magmatism, *in* Coward, M.P., and Reis, A.C., eds., Collision tectonics, Special Publications Geological Society of America, v. 19, p. 67-81.

Hawkins, J.W., Bloomer, S.H., Evans, C.A., and Melchoir, J.T., 1984, Evolution of intra-oceanic arc-trench systems, in Carlson, R.L., and Kobayashi, K., eds., Geodynamics of back-arc regions: Tectonophysics, p. 175-205.

Hedge, C.E., and Sacey, J.S., 1980, Precambrian geochronology of northern Utah: Geological Society of America Abstracts with Programs v.12, p. 275.

Hedge, C.E., Sacey, J.S., and Bryant, B., 1983, Geochronology of the Farmington Canyon Complex, Wasatch Mountains, Utah, *in* Miller, D.M., ed.,) Tectonic and stratigraphic studies of the eastern Great Basin: Geologic Society of America Memoire 157, p. 37-44.

Hintze, L.F.,1993, Geologic history of Utah: Brigham Young University Geology Studies Special Publication 7, p. 202.

Hsu, K.J., 1968, Principles of mélanges and their bearing on the Franciscan-Knoxville Paradox: Geologic Society of America Bulletin, v. 79, p. 1063-1074.

Knauth, L.P., and Lowe, D.R., 2003, High Archean climatic temperature inferred from oxygen isotope geochemistry of cherts in the 3.5 Ga Swaziland Supergroup, South Africa: Geological Society of America Bulletin, v. 115, p. 566-580.

Kröner, A., 1985, Evolution of the Archean Continental Crust, Ann. Rev. Earth Planet Sci. v. 13, p. 49-75.

Kusky, T.M., 1998, Tectonic setting and terrane accretion of the Archean Zimbabwe craton: Geology, v. 26, p. 163-166.

Kusky, T.M., Li, J.-H., and Tucker, R.D., 2001, The Archean Dongwanzi ophiolite complex, North China craton: Geology, v. 26, p. 163-166.

Kusky, T.M., and Polat, A., 1999, Growth of granite-greenstone terranes at convergent margins, and stabilization of Archean cratons: Tectonophysics, v. 305, p. 43-73.

Le Maitre, R.W., 2002, Igneous rocks, a classification and glossary of terms: Cambridge, Cambridge University Press, 236 p.

Li, J.-H., Kusky, T.M., and Huang, X., 2002, Archean podiform chromitites and mantle tectonites in ophiolitic mélange, North China craton; a record of early oceanic mantle processes; GSA Today, v. 12, p. 4-11.

Lowe, D.R., 1999, Petrology and sedimentology of cherts and related silicified sedimentary rocks in the Swaziland Supergroup: Geologic Society of America Special Paper 329, p. 83-114.

Lowe, D.R., and Byerly, G.R., 1999, Stratigraphy of the west-central part of the Barberton Greenstone Belt, South Africa: Geologic Society of America Special Paper 329, p. 1-36.

Maliva, R.G., Knoll, A.H., and Simonson, B.M., 2005,Secular change in the Precambrian silica cycle: Insights from chert petrology: GSA Bulletin, v. 117, no. 7/8, p. 835-845.

Miller, E.L., Egger, A., Forrest, S., and Wright, J.E., 2002, Syn-extensional magmatism in the Grouse Creek and Albion Mountains metamorphic core complexes, Utah and Idaho—Implications for gneiss dome genesis: Geological Society of America Abstracts with Programs, v. 34, p. 108.

Nelson, S.T., Harris, R.A., Dorais, M.J., Heizler, M., Constenius, K., and Barnett, D.A., 2002, Basement complexes in the Wasatch Fault, Utah, provide new limits on crustal accretion: Geology, v. 30, p. 831-834.

Parman, S.W., and Grove, T.L., 2004, Petrology and geochemistry of Barberton komatiites and basaltic komatiites: Evidence of Archean fore-arc magmatism, *in* Kusky, T.M., ed., Precambrian Ophiolites and Related Rocks, Developments in Precambrian Geology: v.13, Amsterdam, Elsevier, p. 539-565.

Parman, S.W., Grove, T.L., and Dann, J.C., 2001, The production of Barberton komatiites in an Archean subduction zone: Geophysical Research Letters, v. 28, no. 13, p. 2513-2516.

Pearce, J.A., and Cann, J.R., 1973, Tectonic setting of basic volcanic rocks determined using trace element analyses: Earth and Planetary Science Letters, v. 19, p. 290-300.

Pearce, J.A., Harris N.B.W., and Tindle, A.G., 1984, Trace element discrimination diagrams for the tectonic interpretation of granitic rocks: Journal of petrology, v. 25, p. 956-983.

Polat, A., and Kerrich, R., 1999, Formation of an Archean tectonic mélange in the Shreiber-Hemlo greenstone belt, Superior province, Canada; Implications for Archean subduction-accretion processes: Tectonics, v. 18, p. 733-755.

Polat, A., and Kerrich, R., 2001, Magnesian andesites, Nb-enriched basalt-andesities, and adakites from late-Archean 2.7 Ga Wawa greenstone belts, Superior Province, Canada: Implications for late Archean subduction zone petrologenetic processes: Contributions to Mineralogy and Petrology, v. 141, no. 1, p. 36-52.

Polat, A., and Kerrich, R., 2002, Nd-isotope systematics of ~2.7 Ga adakites, magnesian andesites, and arc basalts, Superior Province: Evidence for shallow crustal

recycling at Archean subduction zones: Earth and Planetary Science Letters, v. 202, no. 2, p. 345-360.

Polat, A., and Kerrich, R., 2004, Precambrian arc associations: Boninites, adakites, magnesium andesites, and Nb-enriched basalts *in* Kusky, T.M., ed., Precambrian Ophiolites and Related Rocks, Developments in Precambrian Geology: v.13, Amsterdam, Elsevier, p. 567-598.

Polat, A., Kerrich, R., and Wyman, D.A., 1998, The late Archean Shreiber-Hemlo and White River-Dayohessarah greenstone belts, Superior province; collages of oceanic plateaus, oceanic arcs, and subduction-accretion complexes: Tectonophysics, v. 289, p. 295-326.

Polat, A., Kusky, T., Li, J., Fryer, B., Kerrich, R., and Patrick, K., 2005, Geochemistry of Neoarchean (ca. 2.55–2.50 Ga) volcanic and ophiolitic rocks in the Wutaishan greenstone belt, central orogenic belt, North China craton: Implications for geodynamic setting and continental growth: GSA Bulletin, v. 117, no. 11/12, p. 1387–1399.

Rapp, R.P., Shimizu, N., and Norman, M.D., 2003, Growth of early continental crust by partial melting of eclogite: Nature, v. 425, p. 605-609.

Reymer, A., and Schubert, G., 1984, Phanerozoic addition rates to the continental crust and crustal growth, Tectonics, v. 3, p. 63-78.

Saleeby, J., 1979, Kaweah serpentinite mélange, southwest Sierra Nevada foothills, California, Geological Society of America Bulletin: v. 90, p. 29-46.

Scholl, D.W., Vallier, T.L., and Stevenson, A.J., 1986, Terrane accretion, production, and continental growth: A perspective based on the origin and tectonic fate of the Aleutian-Bering Sea region: Geology, v. 14, p. 43-47.

Shervais, J.W., 1982, Ti-V plots and the petrogenesis of modern and ophioloitic lavas: Earth and Planetary Science Letters, v. 59, p. 101-118.

Shervais, J.W., 2004, Is the southern Farmington Canyon complex a late Archean/early Proterozoic accretionary complex? *In* Reimold, W.U., Hofman, A., eds., Abstract volume, Field Forum on Processes on the Early Earth, Kaapvaal Craton, Geological Society of South Africa, Johannesburg, SA, 4-9 July 2004, p. 88-89.

Shervais, J.W., 2006, The significance of subduction-related accretionary complexes in early Earth processes, *in* Reimold, W.U., and Gibson, R.U., eds., Processes on the Early Earth: Geological Society of America Special Paper 405, p. 173-192.

Shervais, J.W., and Kimbrough, D.L., 1987, Alkaline and transitional subalkaline metabasalts in the Franciscan complex mélange, *in* Morris, E.M., and Pasteris J.D., eds., Mantle metasomatism and alkaline magmatism: Geological Society of America Special Paper 215, p. 167-182.

Shervais, J.W., Vetter, S.K., and Lindstrom, M.M., 1990, Chemical differences between small sub-samples of Apollo 15 Olivine Normative Basalt, in Sharpton, B., and Ryder, G., eds., Proceedings 20th Lunar and Planetary Science Conference, Lunar and Planetary Institute, Houston, p. 109-126.

Todd, V.R., 1980, Structure and petrology of a Tertiary gneiss complex in northwestern Utah: Geological Society of America Memoir 153, p. 349–383.

Willis, G.C., Yonkee, A., Doelling, H.H., and Jensen, M.E., 2000, Geology of Antelope Island State Park, Utah. *in* Sprinkel, D., Chidsey, T.C., and Anderson, P.B., eds., Geology of Utah's Parks and Monuments: Utah Geological Association Publication 28, p. 337-364.

Wood, D.A., 1980, The application of a Th-Hf-Ta diagram to problems of tectonomagmatic classification and to establishing the nature of crustal contamination of basaltic lavas of the British Tertiary volcanic province: Earth and Planetary Science Letters, v. 50, no. 1, p. 11-30.

Wyman, D.A., and Kerrich, R., 2002, Formation of Archean continental lithospheric roots: The role of mantle plumes: Geology, v. 30, p. 543-546.

Yonkee, W.A., Willis, G.C., and Doelling, H.H., 2000, Petrology of Precambrian rocks of the Farmington Canyon complex, Antelope Island, Utah. *in* King, J.K., and Willis, G.C., eds., The geology of Antelope Island, Davis County, Utah; Utah Geological and Mineral Survey, Miscellaneous Publications MP-00-1, 163 p.

Zegers, T.E., and van Keken, P.E., 2001, Middle Archean continent formation by crustal delamination: Geology, v. 29, p. 1083-1086.

APPENDIX

Standards for XRF analysis:

Standard	Source
VG2	National Museum of Natural History
Kakanui Hornblende	National Museum of Natural History
Kakanui Augite	National Museum of Natural History
Plagioclase Lake County	National Museum of Natural History
San Carlos Olivine	National Museum of Natural History
Plagioclase	National Museum of Natural History
Apatite	National Museum of Natural History
Amelia Albite	National Museum of Natural History
Amelia K-spar	National Museum of Natural History

Synthetic and Natural standards for EMP analysis are all from USGS, National Museum of Natural History, and Smithsonian Institute.

Minerals used: Ilmenite, Corundum, Hematite, Diopside, Chromite, Albite, and Sanidine. VG2 was also used for volcanic glass standard

Standards for ICP-MS:

BCR-2	USGS
BHVO-2	USGS
W-2	USGS

Blanks and in-house prepared standards were also used.

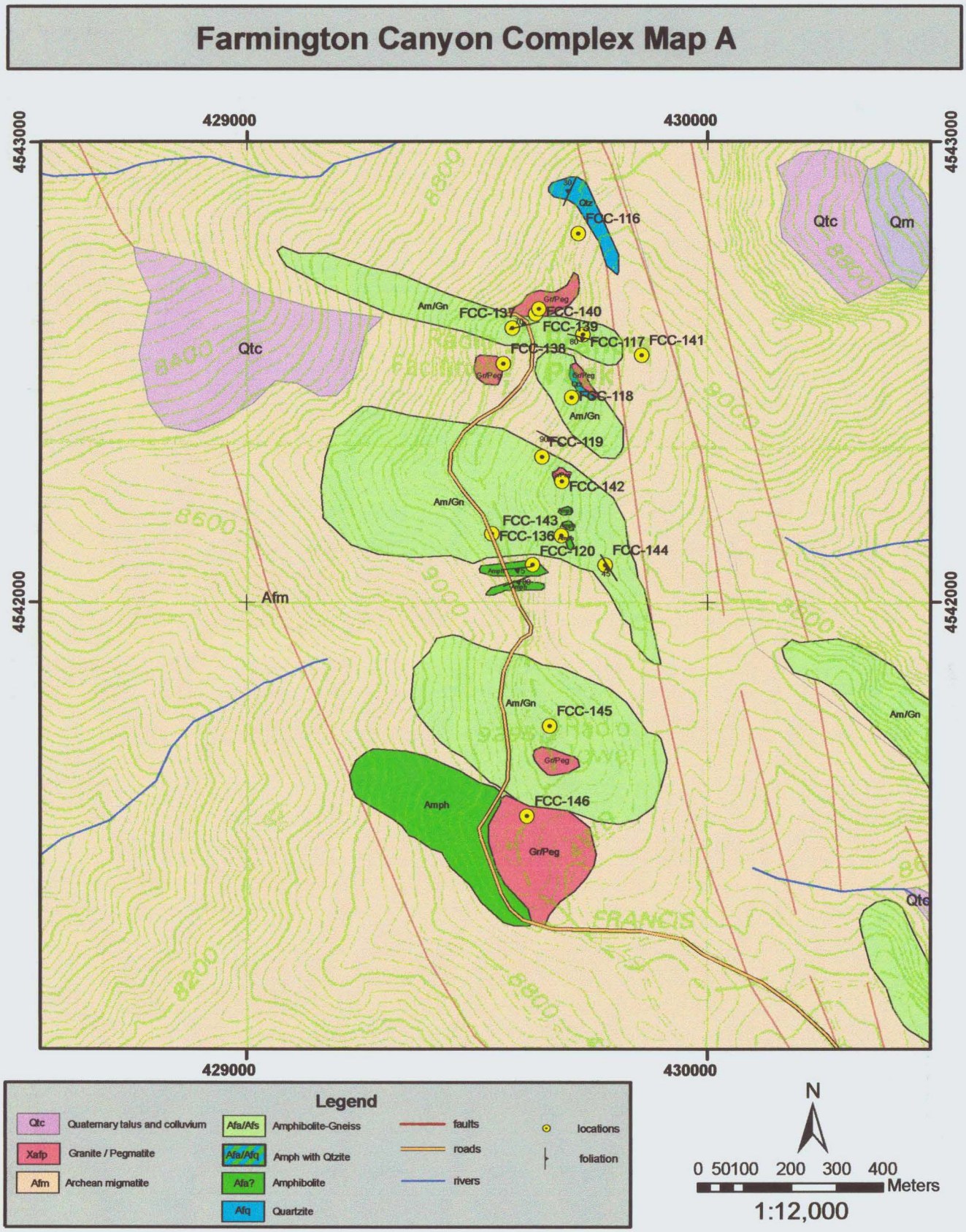

Plate I. Detailed map of Francis Peak area in the Farmington Canyon Complex.

Farmington Canyon Complex Map B

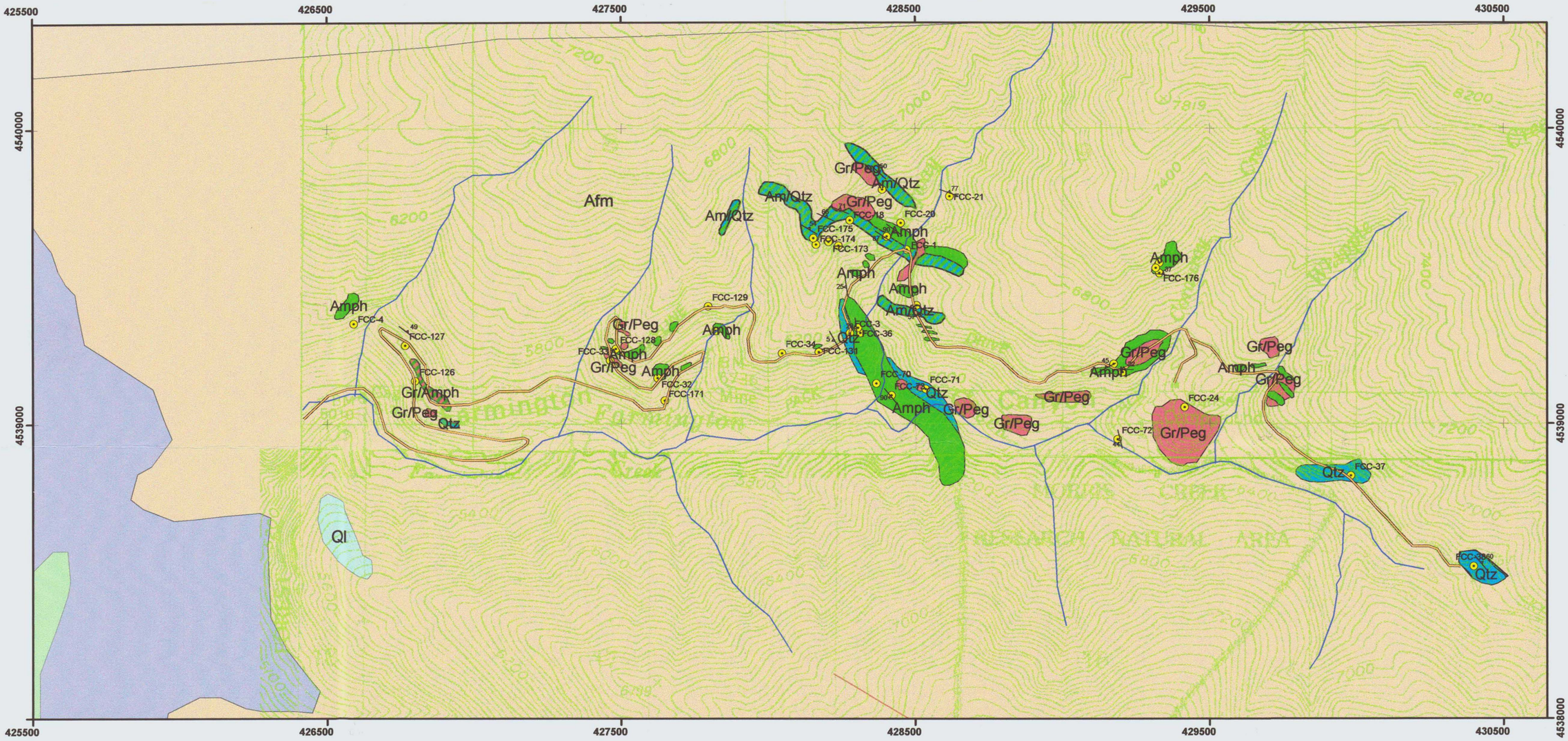

Legend

Ql	Quaternary landslide deposits	Afs	Archean schist and gneiss	Afa	Amphibolite
Qb	Quaternary Lake Bonneville group	XAfp/Afa	Granite with Amphibolite	Afq	Quartzite
XAfp	Granite	Afa/Afs	Amphibolite-Gneiss		locations
Afm	Archean migmatite	Afa/Afq	Amphibolite with Quartzite		foliation

faults
roads
rivers

N

0 150 300 600 900 1,200 Meters

1:12,000

Plate II. Detailed map of Farmington Canyon, in the Farmington Canyon Complex.

Farmington Canyon Complex Map C

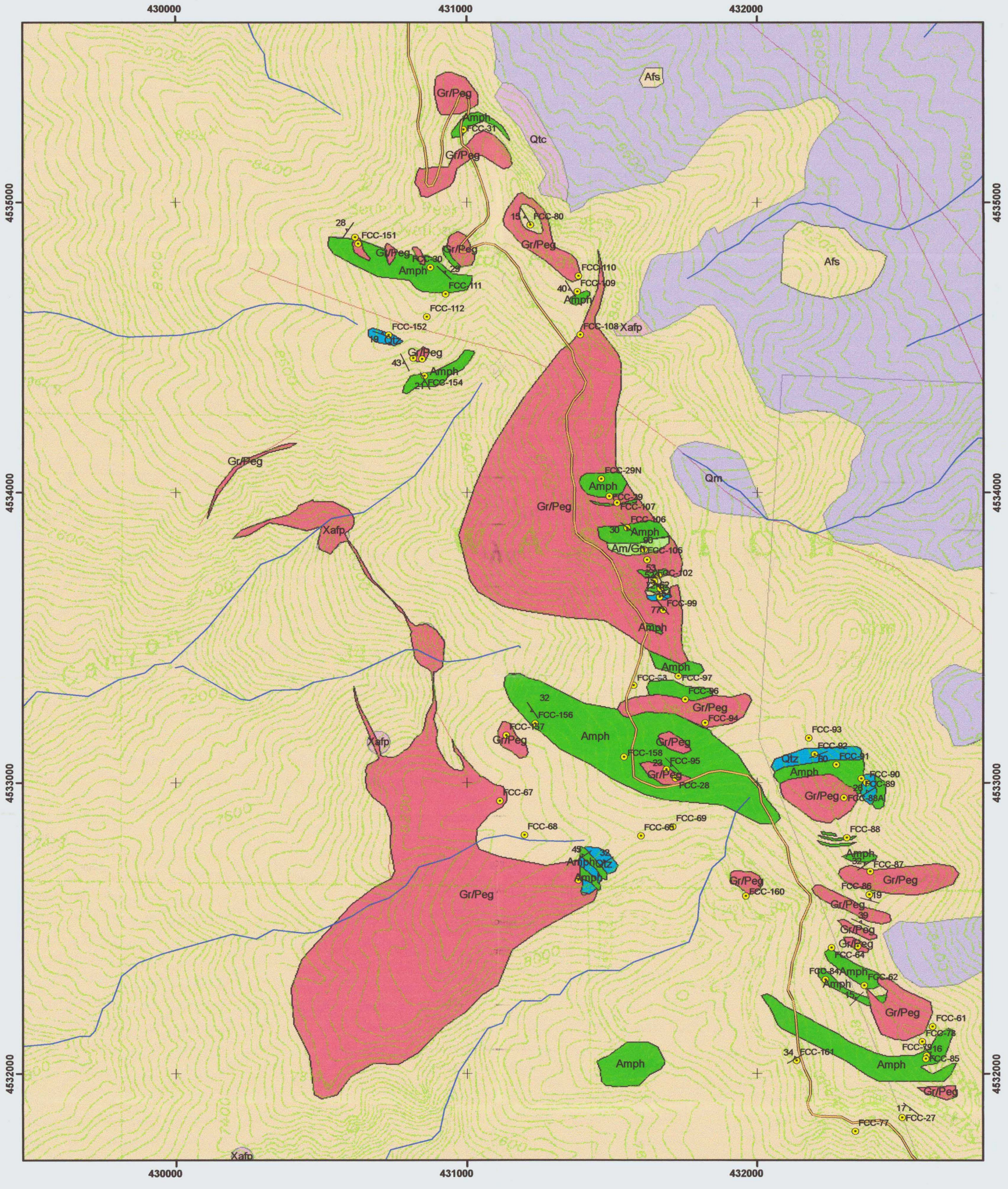

Legend

Qtc	Quaternary talus and colluvium	Afs	Archean schist and gneiss		faults
Qm	Quaternary till and outwash deposits	Afa	Amphibolite		roads
Tw	Tertiary Wasatch Formation	Afq	Quartzite		rivers
Xafp	Archean/Early Proterozoic Pegmatite		locations		foliation
Xafp	Granite				

N

0 100 200 400 600 800 Meters

1:12,000

Plate III. Detailed map of Bountiful Peak in the Farmington Canyon Complex.

Farmington Canyon Complex Map D

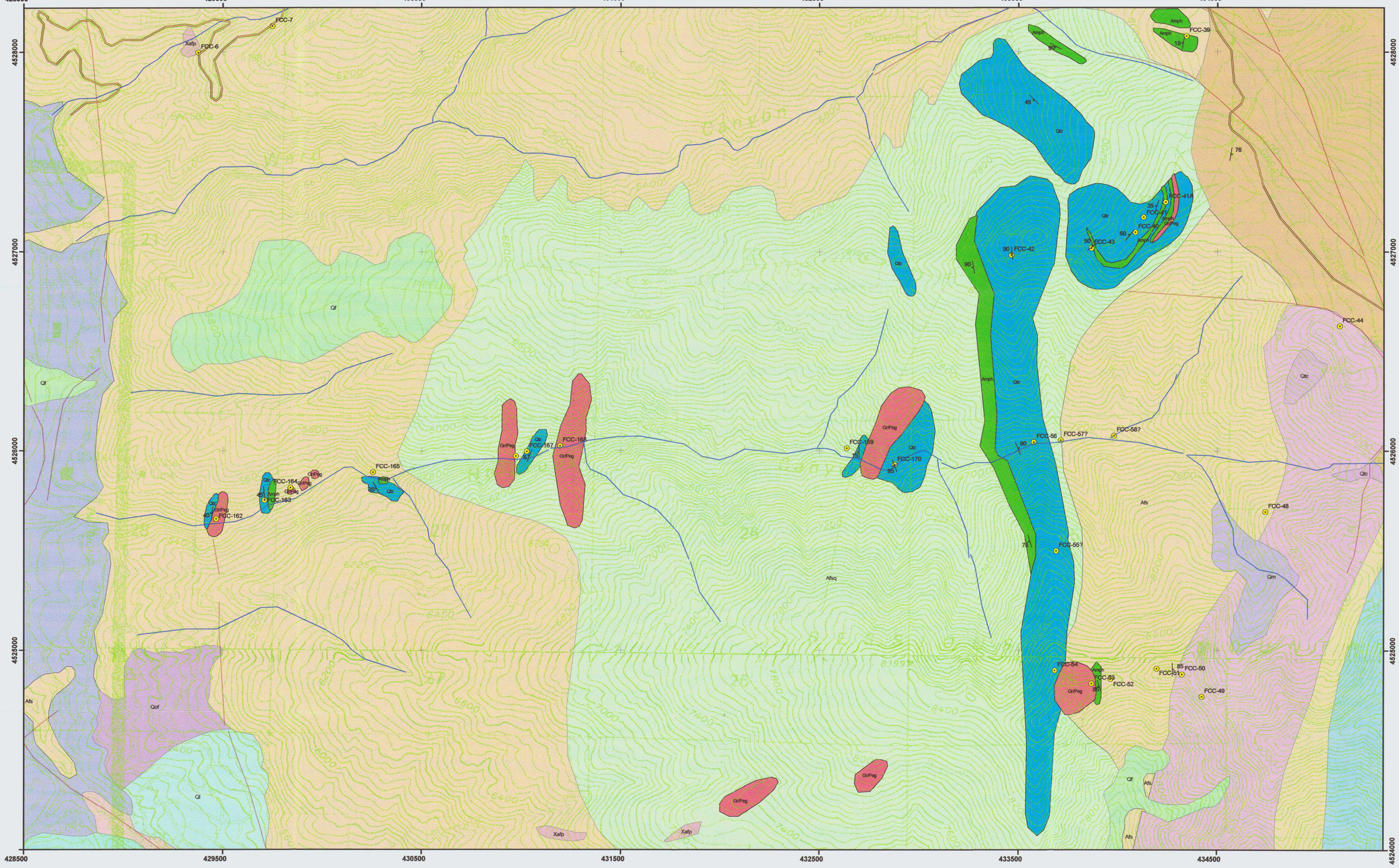

Legend

Qf	Quaternary debris fan deposits	Tw	Tertiary Wasatch Formation	Afs	Archean shist and gneiss
Ql	Quaternary landslide deposits	Ct	Cambrian Tintic quartzite	Afsq	Archean quartzite, gneiss and schist
Qm	Quaternary till and outwash deposits	Xafp	Archean/Early Proterozoic Pegmatite	Afa	Amphibolite
Qb	Quaternary Lake Bonneville Group	XAfp	Granite	Afq	Quartzite
Qof	Quaternary old debris fan deposits				

roads
rivers
faults
foliation
locations

N

0 300 600 1,200 Meters

1:12,000

Plate IV. Detailed map of the Session Mountains in the Farmington Canyon Complex.